

Dipartimento di / Department of

Fisica "G. Occhialini"

Dottorato di Ricerca in / PhD program Fisica ed Astronomia Ciclo / Cycle XXXIV.

Curriculum in (se presente / if it is) Fisica Subnucleare

**First observation of the electroweak production of
a W^+W^- pair in association with two jets in the
fully leptonic channel with the CMS detector at
the LHC**

Cognome / Surname Cetorelli Nome / Name Flavia

Matricola / Registration number 841313

Tutore / Tutor: Prof. Alessio Ghezzi

Cotutore / Co-tutor:
(se presente / if there is one)

Supervisor:
(se presente / if there is one)

Coordinatore / Coordinator: Prof.ssa Marta Calvi

ANNO ACCADEMICO / ACADEMIC YEAR 2020/2021

Summary

This thesis reports the first observation of the electroweak production of a W^+W^- bosons pair in association with two jets in the fully leptonic final state. The analysis has been performed using the data sample collected by the CMS detector during the 2016-2018 proton-proton collisions at center-of-mass energy $\sqrt{s} = 13$ TeV, provided by the Large Hadron Collider (LHC).

The electroweak W^+W^- production belongs to the very rare class of vector boson scattering (VBS) processes, which are purely electroweak at tree level. Their cross sections span in the range of fb. The investigation of VBS processes is a central objective of the LHC since they are essential tools to test the consistency of the electroweak sector of the standard model. Indeed, they are connected directly to the Higgs boson and the spontaneous symmetry breaking mechanism of the electroweak interaction. Moreover, VBS processes are sensitive to possible anomalies arising in triple and quartic gauge couplings; they offer a way to study the possibility of a new physics beyond the standard model (BSM). VBS processes have a characteristic signature consisting of two high-energy jets placed in the backward-forward parts of the detector.

The final state chosen for the electroweak W^+W^- analysis is the fully leptonic one; the two W bosons decay in a lepton (an electron or a muon) and its corresponding neutrino. The leptonic final state was preferred due to its higher signal purity with respect to the other ones. The events were selected requiring the presence of two charged leptons with opposite sign charges, two jets with large invariant mass and large pseudorapidity separation, and a certain amount of missing transverse momentum. Events are then separated into different categories considering the flavor of the charged leptons: ee , $\mu\mu$, and $e\mu$. The $t\bar{t}$ - tW productions constitute the main background of the analysis; this large background may be reduced with a veto against the jets containing b quark, produced by the decay of the top quark. Another important source of background is due to diagrams containing two QCD vertices, which produce the same final state as the signal (QCD-induced W^+W^- production). Events from this irreducible background may be discarded only by applying stringent cuts on the kinematics of the jets. The Drell-Yan (DY) production contaminates the ee and $\mu\mu$ final states, while this background is highly suppressed in the $e\mu$ one. Even though ee and $\mu\mu$ categories have a lower signal-to-background ratio with respect to the different flavor final state, their inclusion in the final fit gives a non-negligible contribution. The final result has been achieved also thanks to the use of a deep neural network (DNN). The DNN was trained to separate the

signal from the $t\bar{t}$ and the QCD-induced W^+W^- production in the $e\mu$ final state. The use of the DNN output as a discriminator in this category has boosted the performance of the analysis.

Finally, the analysis reaches the observation of the electroweak W^+W^- signal with a statistical significance of 5.6 standard deviations, whereas 5.2 standard deviations were expected. Moreover, two cross sections are measured into two different fiducial phase spaces. The first one is an inclusive phase space, defined with cuts at parton level on the two outgoing partons: they are required to have a $p_T > 10$ GeV and an invariant mass $m_{qg'} > 100$ GeV. The measured cross section in the inclusive phase space is 99 ± 20 fb to be compared with the theoretical expectation at the lowest order of 89 ± 5 fb. The uncertainty in the expected cross section is due to theoretical uncertainties related to the QCD factorization scale of the signal. The second one is an exclusive volume, defined with requirements on observables at generator level that mimic the ones of the analysis signal region. In this fiducial volume, the cross section observed is 10.2 ± 2.0 fb, while the expected one is 9.1 ± 0.6 fb. These are the first measurements of the purely electroweak W^+W^- cross section; the results show good agreement with standard model expectations. The data sample that will be collected during Run III, starting in 2022, will surely improve the current knowledge of the electroweak W^+W^- process. Indeed, a significant improvement is expected since the main impact on the final precision of the reported results is due to statistical uncertainty.

The thesis also reports the work for the electromagnetic calorimeter (ECAL) calibration. Indeed, a good calibration is essential to achieve an optimal analysis performance. A new calibration method (EFlow) for the ECAL was developed and tested during this work. The method can provide per-crystal intercalibration with a time granularity of about 1-2 days to correct the time drift in light response that is still visible after laser corrections. The method relies on the use of minimum bias events from low energy events, as the ϕ -symmetry method, which are expected to have a uniform distribution in ϕ . The EFlow extends the idea of the ϕ -symmetry method, normalizing the energy of each crystal to the mean of the barrel. In this way, the response in time of each crystal is adjusted to the average drift of the barrel. Then, events with electrons from W and Z decays are used to correct the residual global drift, providing an overall correction averaged on all the barrel crystals. The corrections derived in this way are competitive with ones obtained by the method employed during Run II, which used the E/p distribution of electrons from W and Z decays. Thanks to the fine space-time granularity of these corrections and the rapidity of deriving them, the method may be implemented in Run III to provide the so-called “prompt” calibrations for the ECAL.

The thesis is divided into four chapters. In Chapter 1, a brief introduction to the standard model of particle physics is given. Moreover, VBS processes are described in detail. Their main features are described and their role in the standard model and beyond the standard model physics is discussed. Finally, the status of the art on VBS analyses in CMS is given to provide to the reader a framework where the result reported in this thesis may be placed. After this introduction, an overview of the

LHC complex and the CMS detector, which collected the data used in the thesis, is given in Chapter 2. Chapter 3 is dedicated to the calibration of the electromagnetic calorimeter of the CMS detector, focusing on the work carried on during this thesis. Finally, Chapter 4 reports the observation of the vector boson scattering process with W^+W^- plus two jets in the leptonic final state; the analysis strategy adopted to obtain the results is reported in detail.

Contents

1	Introduction	6
1.1	The standard model of particle physics	6
1.1.1	Fermions and bosons	7
1.1.2	The local gauge invariance principle	7
The quantum chromodynamics	7	
The electroweak sector	9	
1.1.3	Spontaneous symmetry breaking mechanism	11
1.1.4	The Lagrangian of the standard model	12
1.1.5	Beyond the standard model	12
1.2	Vector boson scattering at the LHC	14
1.2.1	The signal topology	14
1.2.2	The Higgs boson and the unitarity of the VBS cross sections .	19
1.2.3	VBS measurements in CMS	20
2	The Compact Muon Solenoid detector at the Large Hadron Collider	25
2.1	The Large Hadron Collider	25
2.2	The Compact Muon Solenoid	28
2.2.1	Tracker	30
2.2.2	ECAL	32
2.2.3	HCAL	34
2.2.4	Muon Chambers	35
2.2.5	Trigger	37
2.3	Event reconstruction	38
2.3.1	Muons	39
2.3.2	Electrons	40
2.3.3	Jets and missing transverse momentum	41
3	Calibration of the electromagnetic calorimeter	42
3.1	Energy reconstruction	42
3.2	Response monitoring and calibration methods	44
3.2.1	The ϕ -symmetry method	47
3.3	The EFlow method for the regional energy drift corrections	50

3.3.1	The Run II regional energy drift corrections	50
3.3.2	Regional energy drift corrections with EFlow + global scale	50
3.3.3	Performance of regional drift corrections for Run III	54
3.3.4	Summary and perspective for Run III	56
4	Electroweak production of a pair of W^+W^- bosons in association with two jets	57
4.1	Signal topology and main backgrounds	57
4.2	Data set, triggers and simulated samples	60
4.2.1	Triggers	60
4.2.2	Simulated samples	61
4.2.3	Signal modeling	62
4.3	Physical objects identification	63
4.3.1	Electrons	63
4.3.2	Muons	65
4.3.3	Jets	65
4.3.4	B tagged jets	66
4.3.5	Missing transverse momentum	66
4.4	Selections	66
4.5	Deep neural network for the $e\mu$ category	71
4.5.1	Deep neural networks	71
4.5.2	Preparation of samples	72
4.5.3	Phase space selection	73
4.5.4	Building a network	73
4.5.5	Final architecture and input variables	75
4.5.6	Training monitoring and performance	78
4.6	Control regions	82
4.7	Background estimation	88
4.8	Systematic uncertainties	89
4.9	Signal extraction	92
4.9.1	Statistical procedure	92
4.9.2	Results	93
4.10	Summary and outlook	97
5	Conclusions	100

1 Introduction

The Large Hadron Collider (LHC) is a circular accelerator that can provide proton-proton collisions at a nominal center-of-mass energy of 14 TeV. The collisions happen in four different points located along its ring. Two general purpose detectors, ATLAS and CMS, are disposed around two of these interaction points to measure the properties of the particles produced during the collisions. The first data-taking period of the LHC, called Run I (2010-2012), provided proton-proton collisions at a center-of-mass energy of 7-8 TeV corresponding to an integrated luminosity of about 30 fb^{-1} . The Run I data collected by the ATLAS and the CMS detectors brought to the observation of the Higgs boson in 2012. After a long shutdown, in 2015 proton collisions restarted at a center-of-mass energy of 13 TeV, and another three-years-long data-taking period (Run II) began at the LHC. The integrated luminosity of Run II is about 138 fb^{-1} . The LHC complex and the CMS detector are described in detail in Chapter 2.

In this work of thesis, the data sample collected by the CMS detector during the 2016-2018 data-taking of proton-proton collisions at a center-of-mass energy of 13 TeV is analyzed to search for the electroweak vector boson scattering production of an opposite sign pair of W bosons plus two jets in the fully leptonic channel. The sample corresponds to an integrated luminosity of about 138 fb^{-1} . In this chapter, the standard model of particle physics is introduced, very briefly, with a focus on the electroweak sector (Sec. 1.1). The vector boson scattering processes are powerful tools to investigate this sector and the mechanism of spontaneous symmetry breaking since they are directly connected to the Higgs boson. These processes are introduced (Sec. 1.2) to show their distinctive kinematic topology and the characteristic signature of the possible final states. Finally, the recent CMS results in this field are reported in Section 1.2.3 to make clear what is the current status of art.

1.1 The standard model of particle physics

Understanding the fundamental structure of the universe is the objective of particle physics. It aims to grasp the ultimate constituents of matter (elementary particles) and the laws followed by them (the forces).

The standard model of particle physics (SM) is based on a relativistic quantum field theory; it embodies the description of three (out of four) fundamental interactions, the strong, the weak, and electromagnetic force. The gravitational force is

left out of this model; its effect on the sub-atomic particles is orders of magnitude weaker than the others, and thus, negligible. In this section, the fundamental features of the SM are presented, underlying its great successes as well as its intrinsic limits. For a more detailed discussion on the SM, see Refs.[1, 2].

1.1.1 Fermions and bosons

According to the standard model, the elementary constituents of matter are point-like particles with spin $\frac{1}{2}$ (fermions), while the mediators of the three fundamental forces are point-like particles with an integer spin (bosons). The twelve fermions, reported in Table 1.1, are classified into three generations (or families). The particles of the first generation constitute the ordinary matter. The ones belonging to the second and the third family could be seen as copies of the firsts (with the same quantum numbers) but with different masses. In the same table, masses and quantum numbers of the fermions are listed, according to Ref. [3]. Antiparticles have the same mass and spin but opposite quantum numbers.

The fundamental constituents of matter are categorized also concerning their participation in the fundamental interactions. The quarks are the only fermions with color charge, and hence they participate in all three interactions. The leptons are color-less particles, and thus they do not feel the strong force, but only the electroweak one, and neutral leptons (neutrinos) interact only weakly since they have no electric charge. The vector bosons, which carry the fundamental forces, are summarized in Table 1.2. One additional scalar boson, the Higgs boson, arising from the mechanism of spontaneous symmetry breaking of the electroweak interaction, completes the framework (cf. Sec. 1.1.3).

1.1.2 The local gauge invariance principle

The SM relies on the $SU(3) \times SU(2)_L \times U(1)_Y$ unitary symmetry group. The first part, the $SU(3)$ symmetry, describes the quantum chromodynamics (QCD), which is the quantum field theory underlying the strong interaction in the SM, whereas the other two, $SU(2)_L \times U(1)_Y$, represent the unification of the electromagnetic and the weak interactions. The local gauge invariance principle guarantees that the theory remains renormalizable, hence predictive and consistent.

The quantum chromodynamics

The QCD can be derived by imposing the invariance of the Lagrangian under the $SU(3)$ local phase transformations in the color space. This new degree of freedom, the color (red, green, blue), is the charge of the QCD interaction. Following Noether's theorem from the invariance under $SU(3)$ transformation arises the conservation of the color charge. Eight force-carrying massless gauge bosons (the gluons) are introduced in the Lagrangian (one for each generator of the $SU(3)$ group) to restore this invariance. Only colored particles (quarks and gluons) can couple to

Table 1.1: The twelve 1/2 spin fermions of the standard model (six leptons and six quarks). Their masses, electric charges (Q), and colors are reported. Weak isospin and hypercharge quantum numbers are reported in Table 1.3. Antiparticles have the same mass of particles and opposite quantum numbers. Neutrinos are considered massless in the SM.

		Particle	Mass [GeV]	Q	Color
Leptons	1st generation	electron e	0.5×10^{-3}	-1	-
		neutrino ν_e	0	0	-
		muon μ	106×10^{-3}	-1	-
	2nd generation	neutrino ν_μ	0	0	-
		tau τ	1.8	-1	-
		neutrino ν_τ	0	0	-
	3rd generation	up u	$2. \times 10^{-3}$	2/3	RGB
		down d	4.7×10^{-3}	-1/3	RGB
		charm c	1.3	2/3	RGB
		strange s	93×10^{-3}	-1/3	RGB
		top t	172.8	2/3	RGB
		bottom b	4.2	-1/3	RGB

Table 1.2: The bosons of the standard model: five vector bosons and one scalar boson. Their spins, masses, electric charges (Q), and colors are reported.

Particle	Spin	Mass [GeV]	Q	Color
gluon g	1	0	0	RGB
photon γ	1	0	0	-
W^\pm	1	80.4	+1/-1	-
Z	1	91.2	0	-
H	0	125.3	0	-

gluons and thus participate in the strong interaction. The Lagrangian of the QCD is

$$\mathcal{L}_{QCD} = \sum_q \bar{\psi}_{q,a} (i\gamma^\mu \partial_\mu \delta_{ab} - g_s \gamma^\mu t_{ab}^C \mathcal{A}_\mu^C - m_q \delta_{ab}) \psi_{q,b} - \frac{1}{4} F_{\mu\nu}^A F^{A\mu\nu} \quad (1.1)$$

with $F_{\mu\nu}^A = \partial_\mu \mathcal{A}_\nu^A - \partial_\nu \mathcal{A}_\mu^A - g_s f_{ABC} \mathcal{A}_\mu^B \mathcal{A}_\nu^C$, $[t^A, t^B] = i f_{ABC} t^C$

where repeated indices are summed over. In the equations above: γ^μ are the Dirac γ -matrices; the $\psi_{q,a}$ are spinors for a quark of flavor q , mass m_q , and color a that runs over the three possible colors; \mathcal{A}_μ^C are the eight gluons field ($C=1,..,8$); t_{ab}^C are the eight 3×3 matrices generators of the SU(3) group; g_s (or $\alpha_s = g_s^2/4\pi$) is the QCD coupling constant; $F_{\mu\nu}^A$ is the field tensor; finally, f_{ABC} are the structure constants of the SU(3) group.

Experimentally, colored particles, such as gluons and quarks, have never been

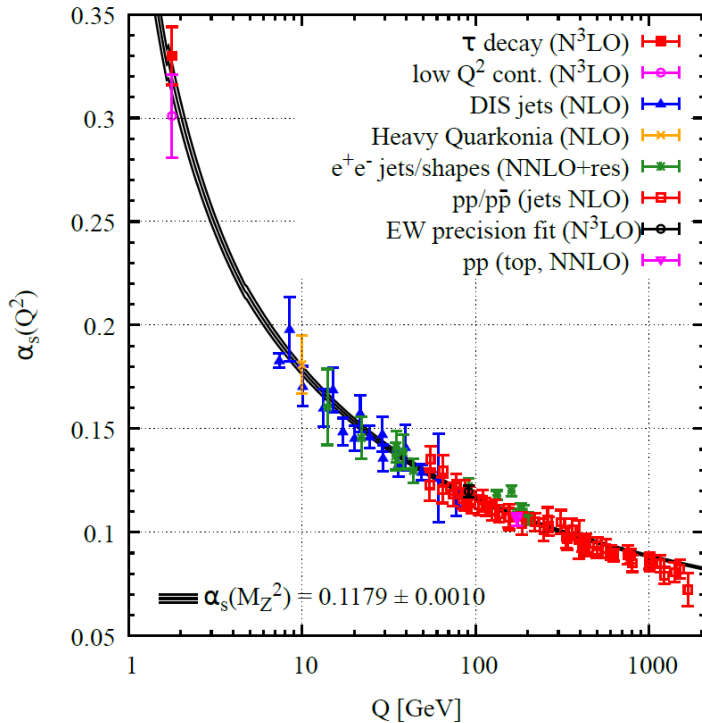


Figure 1.1: The QCD coupling constant (α_s) as a function of the transferred momentum (Q). From Ref. [3].

observed as free particles. Only color-less objects (hadrons), which result from an aggregation of colored quarks and gluons, are observed. The evidence of this color confinement is a direct consequence of the running of the QCD coupling parameter (α_s). Indeed, α_s decreases at high energy (short-distance interaction), while increases at low energy (large-distance interaction), as reported in Figure 1.1. According to Ref. [3], the current value of α_s at the Z boson mass scale is

$$\alpha_s(M_Z^2) = 0.1179 \pm 0.0009. \quad (1.2)$$

When quarks are produced in a collision, they never remain unbounded. Indeed, after their production, as the energy decreases and the distance becomes relatively large (time scale order of fs), the QCD coupling increases leading to the formation of bound states, such as mesons ($q\bar{q}$) and baryons (qqq). This process is the so-called hadronization; its final products are the jets, which are groups of hadrons (mesons or baryons).

The electroweak sector

The electromagnetic interaction and the weak interaction are unified in one single electroweak theory by Glashow, Salam e Weinberg [4, 5, 6]. The electroweak theory can be derived by requiring the invariance of the Lagrangian under the $SU(2)_L \times U(1)_Y$ local gauge transformations. Three vector bosons W_1, W_2, W_3 arise from the

requirement to respect the $SU(2)_L$ symmetry. Their coupling constant is defined to be g . Left handed fermions are $SU(2)_L$ weak isospin (T) doublets, while right-handed ones are isospin singlets (as shown in Table 1.3). An exception is made for neutrinos, which in the theory are considered massless and therefore have no right-handed component.

Table 1.3: Weak isospin and hypercharge quantum numbers for leptons and quarks. In the SM neutrino are massless, hence they do not have a right-handed component.

Lepton	T	T^3	Y	Quark	T	T^3	Y
ν_e	1/2	1/2	-1	u_L	1/2	1/2	1/3
e_L	1/2	-1/2	-1	d_L	1/2	-1/2	1/3
-	-	-	-	u_R	0	0	4/3
e_R	0	0	-2	d_R	0	0	-2/3

The mediators of the weak charged current interactions, the physical W^\pm bosons, could be identified as a linear combination of the first two gauge bosons described above:

$$W_\mu^\pm = \frac{1}{\sqrt{2}}(W_\mu^1 \mp iW_\mu^2),$$

The $SU(2)_L$ symmetry is not enough to describe completely the weak interaction, as the W^3 can not be interpreted as the physical Z boson. For a complete description, another $U(1)_Y$ local gauge invariance is needed, which introduces a fourth gauge boson B with a coupling constant g' . The weak hypercharge Y (reported in Table 1.3) is directly related to the electromagnetic charge (conserved in the electromagnetic interaction) and the third component of the weak isospin (conserved in the weak interaction)

$$Q = T^3 + \frac{Y}{2}$$

The values of the weak hypercharge are reported in Table 1.3 for each fermion. It was shown, at first by Glashow [4, 6] and then by Weinberg and Salam [5], that the weak interaction and electromagnetic interaction can be unified in this way. Indeed, the gauge bosons, which describes the weak and electromagnetic neutral current interactions, can be expressed as the combination of the W^3 and B field

$$\begin{aligned} A_\mu &= \cos \theta_W B_\mu + \sin \theta_W W_\mu^3, \\ Z_\mu &= -\sin \theta_W B_\mu + \cos \theta_W W_\mu^3; \end{aligned} \tag{1.3}$$

where θ_W is a mixing angle sometimes called the Weinberg angle. This angle is directly related to the g, g' coupling constants as

$$\tan \theta_W = \frac{g'}{g}. \tag{1.4}$$

1.1.3 Spontaneous symmetry breaking mechanism

In the last section, it has been shown that both QCD and EW interactions descend from the local gauge invariance principle. But to satisfy the symmetries, the gauge bosons introduced must be massless. This statement is true for the photon and the gluons, but it does not hold for the Z and W^\pm bosons, as proven experimentally. Moreover, this model does not accommodate the mass of the fermions. Inserting the needed mass terms ($m\bar{\psi}\psi$) by hand is not a viable solution since these terms violate the gauge invariance leading to an unrenormalizable and unpredictable theory. The Brout-Englert-Higgs [7, 8] mechanism shows how mass terms for both bosons and fermions could be generated through a scalar field, making hidden, but still intact, the underlying symmetry. To realize this mechanism, the most simple choice is to introduce an isospin doublet of two complex scalar fields with weak hypercharge $Y = 1$

$$\phi = \begin{pmatrix} \phi^+ \\ \phi^0 \end{pmatrix} = \frac{1}{\sqrt{2}} \begin{pmatrix} \phi_1 + i\phi_2 \\ \phi_3 + i\phi_4 \end{pmatrix} \quad (1.5)$$

that is added in the Lagrangian with a potential term

$$V(\phi) = \mu^2 \phi^\dagger \phi + \lambda (\phi^\dagger \phi)^2. \quad (1.6)$$

This potential have an infinite degenerate number of minima for $\mu^2 < 0$ and $\lambda > 0$. If a suitable choice for the vacuum expectation value is made, like

$$\phi_0 = \sqrt{\frac{1}{2}} \begin{pmatrix} 0 \\ v \end{pmatrix}, \text{ where } v = 246.22 \text{ GeV}, \quad (1.7)$$

the $SU(2)_L \times U(1)_Y$ symmetry is broken, leading to the generation of masses for the associated gauge bosons. However, with this choice, the $U(1)_{em}$ symmetry is left untouched. Indeed, ϕ_0 is neutral and thus preserves the invariance under $U(1)_{em}$, leaving the photon massless. Thus, boson masses are then found to be

$$m_H = \sqrt{2v^2 \lambda}, \quad (1.8)$$

$$m_W = \frac{1}{2}vg, \quad (1.9)$$

$$m_Z = \frac{1}{2}v\sqrt{g^2 + g'^2}, \quad (1.10)$$

$$m_A = 0 \quad (1.11)$$

The values of these masses are not predicted by the standard model but have to be experimentally measured. The process explained above is referred to as the spontaneous breaking of the electroweak symmetry. Thanks to this process, the masses of the weak bosons are naturally incorporated into the theory. Eventually, the introduction of terms related to the Yukawa interaction generate the masses of the fermions with the same Higgs field doublet.

1.1.4 The Lagrangian of the standard model

Finally, the Lagrangian of the SM may be written as the sum of a kinematic term (\mathcal{L}_{kin}) plus two terms ($\mathcal{L}_{QCD}, \mathcal{L}_{EW}$), which describe the strong interaction and the electroweak one

$$\mathcal{L} = \mathcal{L}_{Kin} + \mathcal{L}_{QCD} + \mathcal{L}_{EW}$$

In particular, the total electroweak (Weinberg-Salam) Lagrangian for one generation of fermions is

$$\mathcal{L} = -\frac{1}{4}\mathbf{W}_{\mu\nu}\mathbf{W}^{\mu\nu} - \frac{1}{4}B_{\mu\nu}B^{\mu\nu} \quad (1.12)$$

$$+ \bar{\psi}_L \gamma^\mu (i\partial_\mu - g \frac{1}{2} \tau \cdot \mathbf{W}_\mu - g' \frac{Y}{2} B_\mu) \psi_L + \bar{\psi}_R \gamma^\mu (i\partial_\mu - g' \frac{Y}{2} B_\mu) \psi_R \quad (1.13)$$

$$+ |(i\partial_\mu - g \frac{1}{2} \tau \cdot \mathbf{W}_\mu - g' \frac{Y}{2} B_\mu)\phi|^2 - V(\phi) \quad (1.14)$$

$$- (G_u \bar{\psi}_L \phi \psi_R + G_d \bar{\psi}_L \phi_c \psi_R + \text{hermitian conjugate}), \quad (1.15)$$

where ψ_L stands for left-handed fermion (lepton or quark), ψ_R is a right-handed fermion singlet, and $G_u(d)$ are the couplings of the up (down) fermions with Higgs boson (Yukawa couplings).

The different terms above are:

- Equation 1.12, the W^\pm, Z, γ , kinetic energies and self-interactions;
- Equation 1.13, the leptons and quarks kinetic energies and their interactions with W^\pm, Z, γ , bosons;
- Equation 1.14, W^\pm, Z, γ, H bosons masses and couplings of the electroweak bosons with the Higgs boson after the EWSSB. Indeed, from the first term, substituting the vacuum expectation chosen as in Equation 1.7, remembering that $\frac{1}{\sqrt{2}}(W_\mu^1 \mp iW_\mu^2)$, and using Equation 1.3 boson masses as in Eqs.1.9-1.11 are obtained. The second term contains the mass of the Higgs boson (cf. Equation 1.8) and its self interaction terms once the vacuum expectation value is put in.
- Equation 1.15, the Higgs interactions with leptons and quarks and their masses after the EWSSB. Fermions' masses, as bosons' ones, are free parameters of the standard model that have to be determined. They are directly related to their Yukawa coupling (G_f) to the Higgs boson as $G_f = \frac{\sqrt{2}m_f}{v}$.

1.1.5 Beyond the standard model

The validity of the standard model of particle physics has been confirmed through the years by vast series of experimental measurements at energies up to the electroweak scale, and recently it has been also confirmed by a variety of measurements

at the LHC (cf. Figure 1.2). Its last success was the discovery of the Higgs boson in 2012 at the LHC, which was the last particle predicted by the model.

Despite the great success of the SM in describing the experimental observations in particle physics, there remain theoretical questions and experimental evidence not satisfactorily explained by the SM.

The energy scale connected with electroweak interaction is about 10^2 GeV, whereas the Planck scale (M_{Planck}), an energy scale related to gravitational interaction, is orders of magnitude higher $M_{\text{Planck}} \sim 10^{19}$ GeV. Going to the Planck scale (if the SM were valid at all energy scales), the loop corrections to the tree level mass of the Higgs boson ($m_H \sim 125$ GeV) become very large, up to 10^{17} GeV. This is the so-called Hierarchy problem. Fine-tuning of higher-order contributions to the Higgs boson mass is needed to produce cancellations, which leave the mass of the Higgs boson close to the electroweak scale. Moreover, huge differences in mass among the particles of the SM (cf. masses reported in Table 1.1-1.2) are observed experimentally. These differences are not explained by the SM since masses are among the ~ 20 free parameters of the model. Their values are not predicted by the theory but have to be determined experimentally. Some experimental evidence deserves an extension of the SM to overcome these shortcomings. The observed asymmetry between matter and anti-matter in the Universe is not explained up to now since the observed CP violation in the SM is not sufficient to justify it. The experimental evidence of neutrinos oscillation implies that these particles must be massive. However, in the SM, neutrinos remain massless even after the EWSSB. Evidence of dark matter from astrophysical and cosmological measurements requires the presence of a viable candidate. No one of the known SM particles is a suitable candidate to explain the amount of dark matter observed. Finally, the description of the gravitational interaction, given by general relativity, is not contained in the SM theory. A possible unification of all the known interactions is not considered.

Thus, many questions remain open in the SM framework, the answer to which should be searched in theories that go beyond it. In the past, various theories have been proposed, from supersymmetry to extra dimensions, but up to today, no experimental evidence to support them has been found. Indeed, the search for hints of physics beyond the SM remains one of the main goals of the LHC program.

In this context, the effective field theory (EFT) [9] approach is a model-independent way to search for deviations from the standard model prediction. The SM Lagrangian can be seen as the first-order low energy approximation of a more general theory valid at all energies. Operators of dimension greater than the SM ones ($d > 4$) appear when expanding at higher orders in energy

$$\mathcal{L}_{\text{EFT}} = \mathcal{L}_{\text{SM}} + \sum_{d>4} \sum_i \frac{f_i^{(d)}}{\Lambda^{d-4}} O_i^{(d)}, \quad (1.16)$$

where Λ is the energy scale where the new physics should appear clearly; $f_i^{(d)}$ are the dimensionless coupling for the $O_i^{(d)}$ operators introduced. Anomalies, which are hints of new physics, may be investigated through the analysis of these dimensionless coefficients, which parametrize the modification to SM vertices.

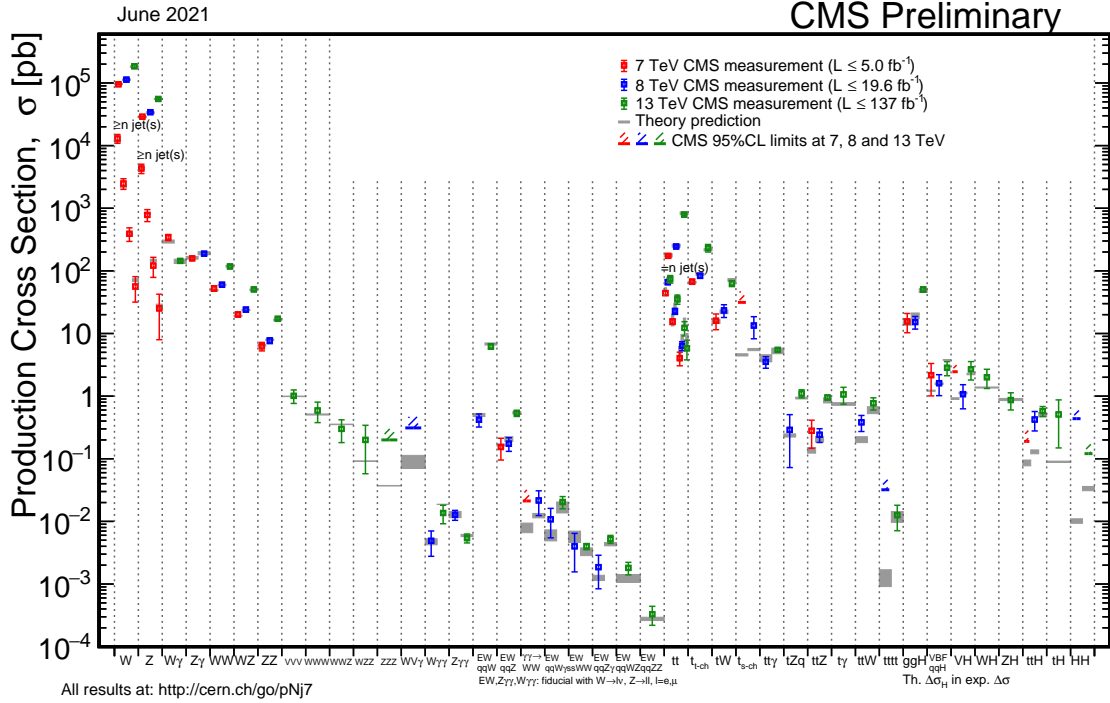


Figure 1.2: Summary of the cross section measurements of standard model processes.

1.2 Vector boson scattering at the LHC

The Higgs and the electroweak (EW) sector of the SM have not been investigated with high precision yet, as the discovery of the Higgs boson dates back to 2012 [10][11], less than ten years ago. Vector boson scattering (VBS) processes [12] are considered useful probes to investigate these sectors and to shed light on the mechanism underneath the spontaneous breaking of the EW symmetry. Moreover, these processes are sensitive to possible anomalies, which could reveal the nature of what lies beyond the SM. In these sections, the VBS kinematic topology is described (Sec. 1.2.1); the relation with the Higgs boson is analyzed in Section 1.2.2; finally, an overview of the current status of VBS analyses in CMS is given in Section 1.2.3.

1.2.1 The signal topology

VBS processes are purely mediated by EW interaction at leading order (LO); they are of order $O(\alpha_{EW}^6 \alpha_S^0)$, counting also the final state objects produced by the decay of massive vector bosons. The wide range of cross sections measured at LHC by the CMS Collaboration is reported in Figure 1.2; the VBS processes are among the rarest production modes measured. Indeed, their cross sections are in the range of a few fbs. Similar measurements are obtained by the ATLAS Collaboration, as reported in Ref. [13].

When two protons collide at the LHC, their partons may emit vector bosons, as depicted in the Feynman diagrams of Figure 1.3 for the W^+W^- production, which

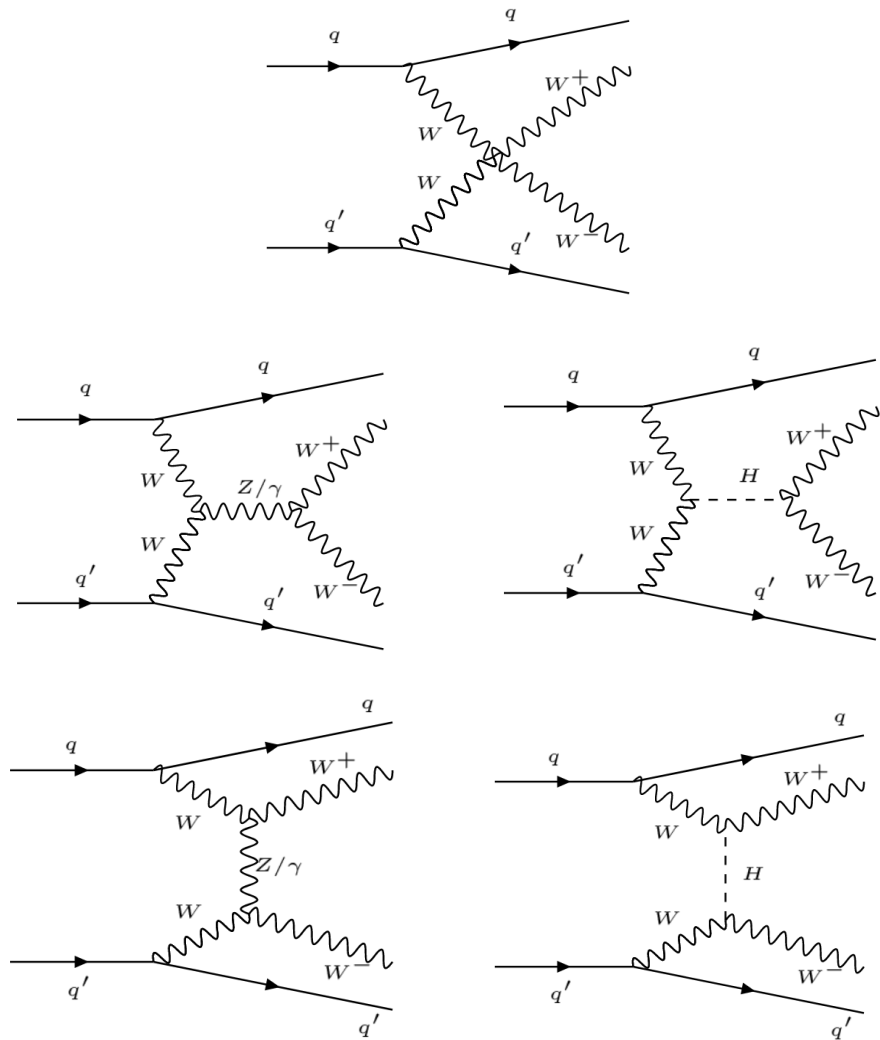


Figure 1.3: Interesting VBS Feynman diagrams at $\mathcal{O}(\alpha_{EW}^6)$ contributing to W^+W^- EW production.

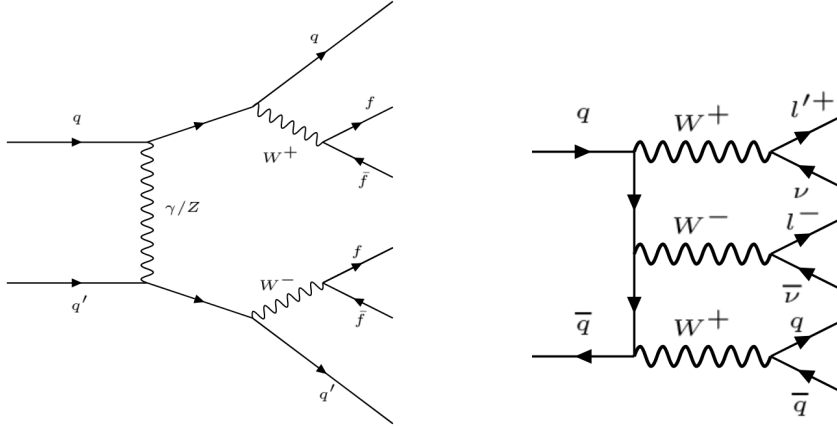


Figure 1.4: Additional diagrams at order $O(\alpha_{EW}^6)$. Even if they are not really interesting, they must be taken into account to preserve the gauge invariance.

interact producing two vector bosons. Eventually, these vector bosons may decay in a pair of leptons or quarks, providing six fermions in the final state.

Figure 1.3 shows the Feynman diagrams at LO contributing to the VBS W^+W^- final state, which is the subject of this thesis. In the first row, the interaction between the W bosons happens directly through a quartic gauge coupling. Graphs in the second (s-channel) and in the third row (t-channel) contain only triple gauge couplings, where the exchange is mediated through a vector (left) or a scalar (right) boson.

Diagrams reported in Figure 1.4 must be considered as well, even though these do not involve a real scatter between vector bosons. Still, they are of order $O(\alpha_{EW}^6)$, and thus, they must be taken into account to preserve gauge invariance.

If the vector bosons are massive, three different types of final state may be defined, depending on their decay mode:

- fully leptonic $VV' \rightarrow l_1\nu_1l_2\nu_2$;
- semileptonic $VV' \rightarrow l\nu qq'$;
- fully hadronic $VV' \rightarrow q_1q'_1q_2q'_2$.

Leptonic decay modes have the advantage of low contamination from QCD-induced processes. They have the highest purity among the other decay modes; however, they have a low branching ratio and thus suffer from large statistical uncertainties. The spread of the new machine learning techniques to suppress the large QCD-induced backgrounds make it feasible to study final states other than leptonic ones. In particular, the semileptonic ones are the most suitable since they have a good equilibrium between the statistics and the signal purity.

Processes like the ones in Figure 1.5 are of order $O(\alpha_{EW}^4\alpha_S^2)$. Here, the initial state quarks interact exchanging a gluon; the W bosons are then emitted by final state quarks and do not interact between them. These processes are called QCD-induced production of W^+W^- bosons since the Feynman diagrams at LO contain

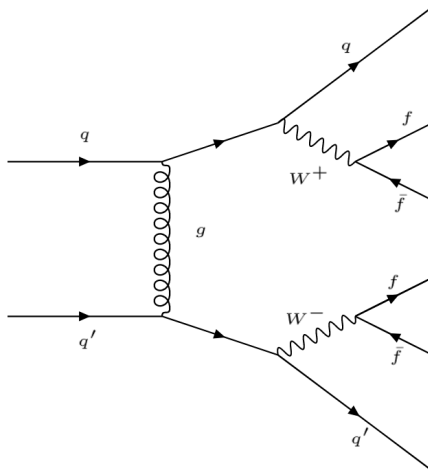


Figure 1.5: Example of a Feynman diagrams at LO of order $O(\alpha_{EW}^4 \alpha_S^2)$, the so-called QCD-induced production of W^+W^- bosons.

two QCD vertices. They are an irreducible background for our EW signal as they share the same final state. The interference between the EW and QCD components has order $O(\alpha_{EW}^5 \alpha_S)$; its contribution usually amounts to only a few percent with respect to the signal yield.

The hadronization process of the two initial state quarks after the interaction in VBS processes produces two jets in the final state, which are often called the tagging or VBS jets. They are characterized by a large invariant mass and a large gap in pseudorapidity. The presence of these two jets is the main peculiarity of a VBS process. Indeed, the two initial state quarks only interact weakly, exchanging a small part of their energy and being deviated only a bit from their initial path (hence the projection in the high rapidity region and the high invariant mass). The correlation between the invariant mass and the rapidity gap of the two tagging jets is reported in Figure 1.6 for the VBS same-sign WW production. Kinematic selections on these two variables are usually adopted to disentangle the VBS signal from other processes, which may mimic the VBS final state. In particular, these are the only effective selections to separate our signal from the irreducible QCD-induced background. Indeed, as reported in Figure 1.6, the tagging jets of the EW signal have high invariant mass and are well separated in pseudorapidity. Instead, the jets associated with W^+W^- QCD-induced background (or the interference) are usually less energetic and more central. In the strong interaction between quarks, more energy is exchanged, causing a severe deflection of the interacting particles. Thus, topological selections on m_{jj} and $\Delta\eta_{jj}$ are usually the best way to distinguish between EW and QCD production and define a VBS-like phase space at high- m_{jj} and high- $\Delta\eta_{jj}$.

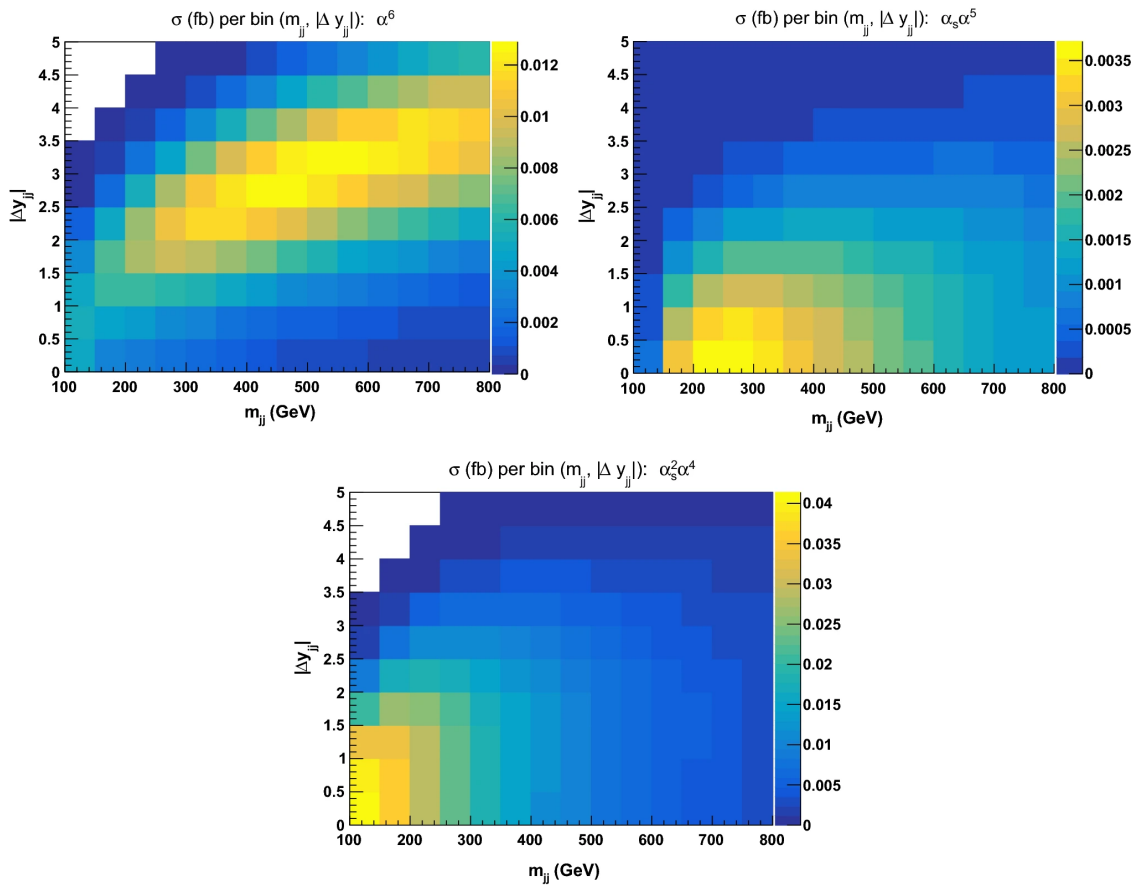


Figure 1.6: Correlation plot between invariant mass and rapidity difference of the two tagging jets for VBS same-sign WW signal (up-left), QCD-induced background (down-middle), and interference(up-right). From Ref. [14].

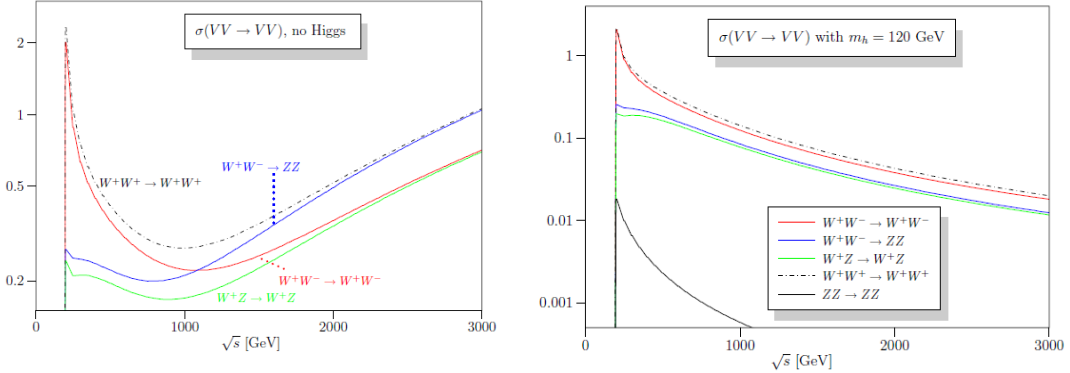


Figure 1.7: Cross sections (in nb) for the five different scattering processes of longitudinal weak gauge bosons. On the left, the scenario with no Higgs boson, on the right SM Higgs boson with a 120 GeV mass is considered. Figure from Ref. [16].

1.2.2 The Higgs boson and the unitarity of the VBS cross sections

The renormalizability of the VBS cross sections is ensured by the presence of the Higgs boson. Indeed, the computation of the amplitude for the $W^+W^- \rightarrow W^+W^-$ scattering produces a matrix element that diverges as $\frac{s^2}{M_W^4}$, when only the diagram with the quartic gauge coupling of Figure 1.3 is considered. Adding in the calculation the diagrams with vector boson exchange in the s- and t-channel (left column of Figure 1.3) do not solve the problem, since the cross section still diverges with the center of mass energy (s) [15]

$$-i\mathcal{M}(W^+W^- \rightarrow W^+W^-) \sim \frac{s}{M_W^2} \quad \text{as } s \rightarrow \infty. \quad (1.17)$$

Only the introduction of diagrams in which a scalar boson is exchanged, as shown in the right column of Figure 1.3, add terms that cancel the divergence. This scalar particle happens to be the Higgs boson with a mass 125 GeV.

Figure 1.7 shows the dependence of cross sections on \sqrt{s} for a variety of VBS processes in different scenarios. The divergence is fixed and the unitarity is restored only when a particle like the Higgs boson is considered. VBS processes are just another example of the necessity of this scalar boson in the SM. Only its presence can assure the unitarity of the theory. However, deviations from the SM expectation could alter this fragile equilibrium. Indeed, changes in the triple or quartic gauge couplings affect the interaction vertices, producing a rise of the cross section that deviates from the expected behavior. Hence, the study of VBS cross sections is a powerful tool to detect possible anomalies in these couplings, which are hints of new physics.

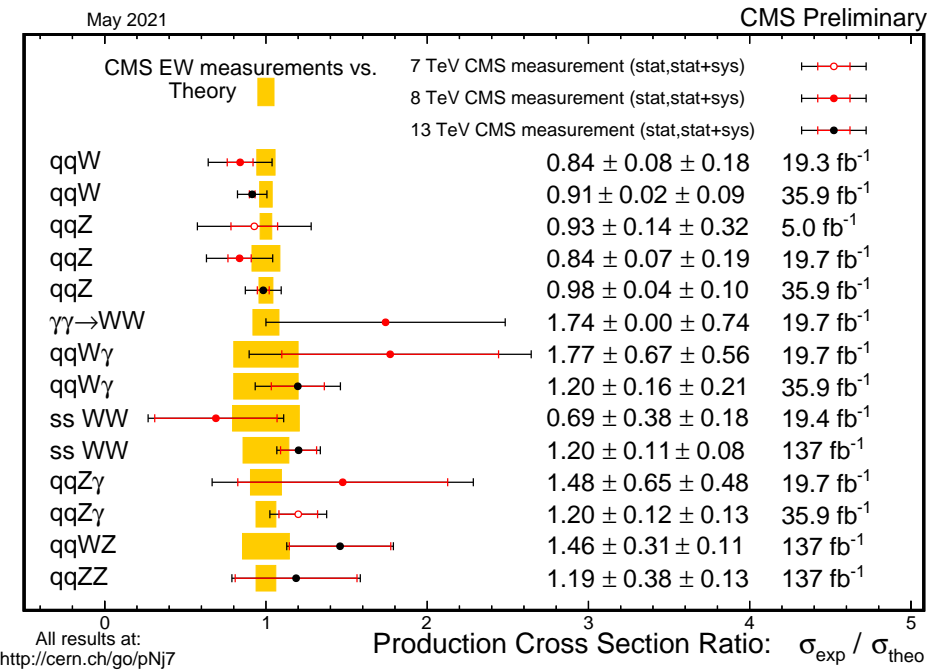


Figure 1.8: Summary of the ratio between measured and predicted cross sections of pure electroweak interactions among the gauge bosons. The plot is updated to May 2021.

1.2.3 VBS measurements in CMS

The electroweak production of two vector bosons in association with two jets has been studied at the LHC since the beginning with the data of the LHC-Run I period ($\sim 30 \text{ fb}^{-1}$). However, the small amount of data and the small cross section of these processes prevent a claim for their observation. Only with the Run II data set (138 fb^{-1}), the first observation of a VBS process was published. Indeed, the increase of center-of-mass energy up to $\sqrt{s} = 13 \text{ TeV}$ in Run II and the larger amount of data collected significantly increase the sensitivity of these searches, which are strongly limited by the statistical uncertainty because of their very low cross sections (see Figure 1.2).

A summary of the CMS results in this field is reported in Figure 1.8, including both Run I and Run II measurements (updated in May 2021). A similar picture, consistent with CMS results, can be drawn for ATLAS results [13]. Results are in good agreement with the standard model predictions; the dominant uncertainty is the statistical uncertainty for most of the measurements reported. In what follows, some of the latest results published by the CMS Collaboration are briefly discussed to give the present status of the art. Indeed, the work of this thesis can be better understood when related to the current status of the knowledge of VBS processes.

The first observation of a VBS process was made in the final state with massive W boson decaying leptonically. In particular, the CMS Collaboration reported the observation with the 2016 data set (35.9 fb^{-1}) of the VBS production of two same-sign W bosons [17]. Indeed, this is the so-called golden channel due to its favorable

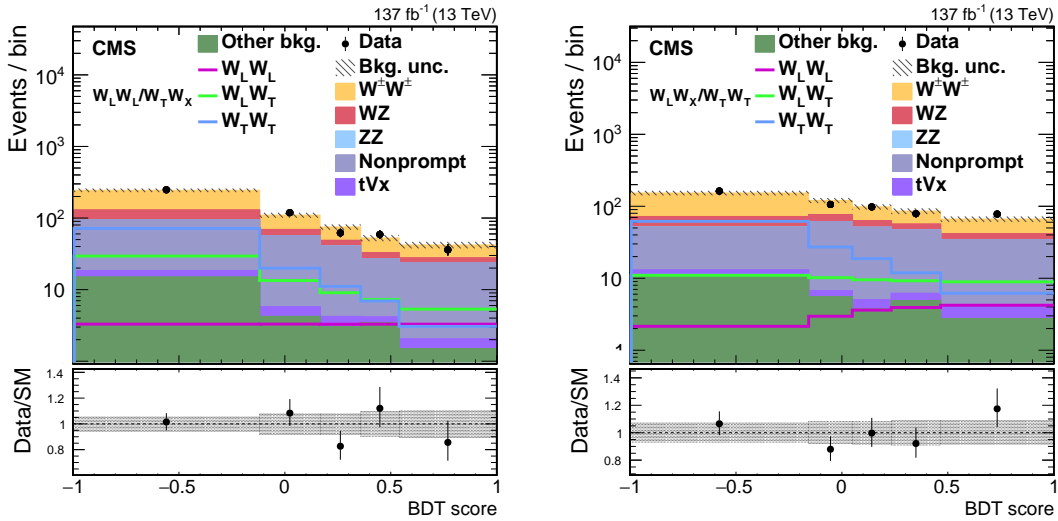


Figure 1.9: Post-fit distributions of the output score of the signal BDT used for the $W_L^\pm W_L^\pm / W_X^\pm W_T^\pm$ (left) and the $W_L^\pm W_X^\pm / W_T^\pm W_T^\pm$ (right) cross section measurements. Here, L and T denote the longitudinal and transverse state of polarization, while X may stand for L or T. In the low panel of each figure, the ratio between the number of events observed in data and the total SM prediction is reported. The gray bands represent the uncertainties in the predicted yields, while vertical bars report the data statistical uncertainties. From Ref. [19]

EW/QCD signal-to-background ratio. The full Run II analysis published by CMS [18] reports the simultaneous cross section measurements of the same-sign WW and WZ bosons pair production in association with two jets. The paper exploits the fully leptonic final state where either two charged leptons ($l^\pm l'^\pm$, with $l, l' = e, \mu$) from the decay of the W pair or three charged leptons ($l^\pm l'^\pm l^\mp$) from the WZ bosons' decays are found. The electroweak production of WZ bosons in association with two jets is observed with a statistical significance of 6.8 statistical deviations (s.d.), while 5.3 s.d. were expected. Studies of inclusive and differential cross sections are performed for both the same-sign WW and the WZ production. In particular, the differential cross sections are measured as functions of various observables such as the invariant masses of VBS jets and charged lepton pairs and the leading-lepton p_T . The comparison with the standard model predictions shows a good agreement with these observed results.

The golden channel has been exploited to obtain the first measurements on the polarized cross sections in a recent CMS analysis, using the 137 fb^{-1} of pp collisions at $\sqrt{s} = 13 \text{ TeV}$ [19]. This analysis is performed in the fully leptonic final state, which guarantees the best signal purity. Boosted decision trees are trained with discriminating kinematic and angular observables to separate the various polarized components (cf. Figure 1.9) as well as to disentangle the inclusive signal from the SM background. Results are derived for the helicity eigenstates defined into either the parton-parton or the WW center-of-mass (c.o.m.) reference frame. The

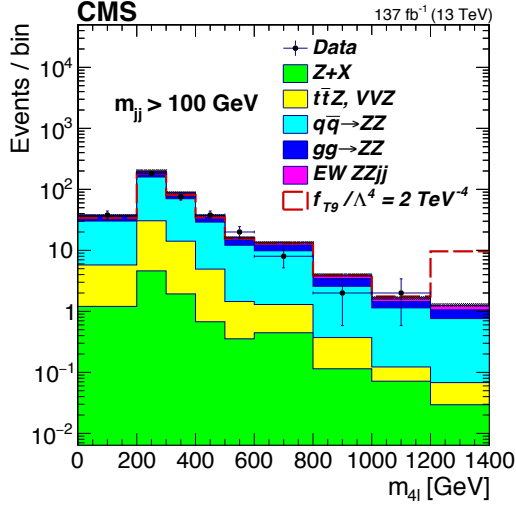


Figure 1.10: Post-fit distributions of the four-lepton invariant mass for f_{T9}/Λ^4 . Black dots with error bars represent the data; filled histograms show the fitted signal and background contributions. From Ref. [20].

paper sets a 95% confidence level upper limit of 1.17 (0.88 expected) fb on the cross section of longitudinally polarized same-sign WW bosons defined in the bosons c.o.m. reference frame. Eventually, the same-sign WW electroweak signal with at least one longitudinally polarized W boson (in the WW c.o.m. reference frame) is found to have an observed (expected) statistical significance of 2.3 (3.1) standard deviations. All the cross sections measured are consistent with the standard model’s expectations.

The VBS ZZ bosons production in the leptonic decay mode has the highest purity among the VBS processes but the lowest branching ratio. Thus, it has not been observed yet in CMS. A claim for evidence, with an observed (expected) statistical significance of 4.0 (3.5) standard deviations for the electroweak signal in the final state with four leptons, has been published by CMS with the full Run II data set [20]. The paper reports a measured fiducial cross section of $\sigma_{fid} = 0.33^{+0.11}_{-0.10}$ (stat) $^{+0.04}_{-0.03}$ (syst) fb, which is in agreement with the standard model expectation. Moreover, a measure involving both the electroweak and QCD components of the ZZjj production is performed. The channel is particularly suitable for searches of anomalies. Indeed, limits are set in an effective field theory approach on a set of anomalous quartic gauge coupling dimension-8 operators, using as discriminating variable the invariant mass of the four final state leptons Figure 1.10. The ZZ channel provides the current most stringent limit at 95% confidence level on the neutral current operator T8 of $-0.43 < f_{T8}/\Lambda^4 < 0.43$.

In a recent publication of the CMS Collaboration, the VBS production with a non-massive vector boson γ and a massive Z boson in the final state has been observed for the first time with a statistical significance much larger than five statistical deviations [21]. The analysis has been performed in the leptonic chan-

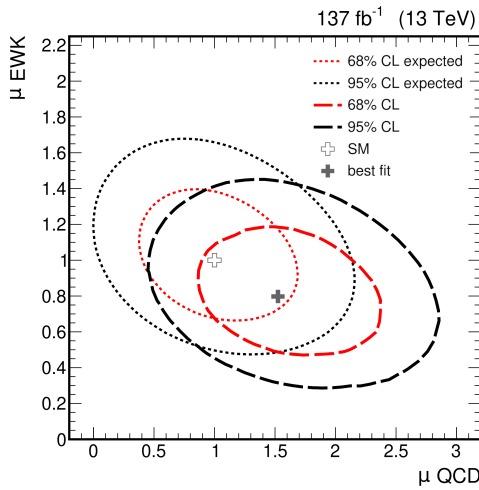


Figure 1.11: Simultaneous fit of EW and QCD components of WV production. The expected and observed 68% and 95% confidence level (CL) contours on the signal strengths are shown. From Ref. [22]

nel, looking for two leptons of opposite sign charge and same flavor, one photon, and two jets with large invariant mass and large pseudorapidity separation. The paper reports the inclusive cross sections for both the electroweak signal alone (5.21 ± 0.52 (stat) ± 0.56 (syst) fb) and the EW+QCD production together (14.7 ± 0.80 (stat) ± 1.26 (syst) fb). Differential cross sections as a function of several observables are calculated as well. All the measured cross sections are in agreement with the standard model leading order predictions. The $Z\gamma$ analysis also puts stringent constraints on a set of anomalous quartic gauge couplings defined in the effective field theory framework.

Final states different from pure leptonic ones have been recently studied by CMS [22]; an evidence for the electroweak production of a WV pair in the semileptonic channel has been reported for the first time with an observed (expected) significance of 4.4 (5.1) standard deviations. The appeal of the semileptonic final state is in the possibility of enhancing the number of signal events because of the higher branching ratio than the leptonic mode. However, the QCD background (in particular due to W+jets events) is also enhanced. Data-driven techniques are employed to cure the uncertainties in the MC modeling of this background. Sophisticated machine learning techniques help to disentangle the signal from the very large background. Events are split into two categories based on how the jets from the hadronically decaying W or Z boson are reconstructed. Indeed, these two jets may be resolved as two different entities by the detector or, in the case of the decay of a boosted boson, they can be reconstructed as a unique large radius jet. The measured fiducial cross section for the electroweak WV signal is $1.90^{+0.53}_{-0.46}$ pb, to be compared with the theoretical prediction of $2.23^{+0.08}_{-0.11}(\text{scale})^{+0.05}_{-0.05}(\text{pdf})$ pb. The fiducial region is defined

with parton level selection: the momentum of the outgoing partons has to be greater than 10 GeV and their invariant mass than 100 GeV. The measurement is also performed in the same fiducial phase space considering as signal the electroweak plus the QCD component of the WVjj production. The measured cross section in this case is $16.6^{+3.5}_{-2.8}$ pb, whereas the theoretical prediction is $16.9^{+2.9}_{-2.1}(\text{scale})^{+0.5}_{-0.5}(\text{pdf})$ pb. The simultaneous two-dimensional fit of the EW and the QCD component is reported in Figure 1.11; results are in agreement with standard model expectations.

Finally, one of the latest results of the CMS Collaboration is the one developed during the work of this thesis. Contrarily to EW same-sign WW, the purely electroweak production of a pair of opposite sign W bosons in association with two jets (W⁺W⁻ jj) has not been observed yet. Indeed, the very large tt} background made challenging the study of this channel. Moreover, this final state is contaminated by a higher irreducible QCD-induced background with respect to the same-sign WW channel. Contamination from Drell-Yan (DY) production is also important for the final state with charged leptons of the same flavor (such as ee and $\mu\mu$). The development of refined machine learning techniques has been employed to obtain optimal discrimination of the signal from the two main background processes (tt} and QCD-induced W⁺W⁻). The effort brings to a measurement of this process with a statistical significance of 5.6 standard deviations. Thus, the first observation for the purely electroweak W⁺W⁻ jj production has been claimed, and the first measurement of its cross section has been provided. This new result and the methods used to obtain it are described in detail in Chapter 4.

2 The Compact Muon Solenoid detector at the Large Hadron Collider

The Large Hadron Collider (LHC) [23] is a circular accelerator designed for investigating the physics up to the energy scale of a few TeV. In particular, it was designed mainly to investigate the electroweak sector to the search for the Higgs boson; this task was accomplished in 2012 [11, 10]. After its discovery, the Higgs boson’s properties have been studied to make the knowledge of the breaking symmetry mechanism clearer. Several channels of research are currently open at the LHC, including consistency tests of the SM and investigation of its possible extensions. Indeed, the LHC objectives are now a deeper understanding of the SM and searches of new physics.

In this chapter, an overview of the LHC machine (Sec. 2.1) and a brief description of the CMS detector (Sec. 2.2), which collected the data used in this work, are given. Finally, in Section 2.3 the algorithm used to reconstruct the final state particles, also called physics objects, is briefly described.

2.1 The Large Hadron Collider

The LHC is a circular accelerator that is placed in a region near the city of Ginevra, between France’s and Switzerland’s territories. It is hosted in an underground tunnel at about 100 m under the surface; the same tunnel previously hosted another great circular accelerator: the Large Electron Positron collider (LEP). The LHC circumference is about 27 km long; the accelerator may produce collisions with protons (or lead ions) up to a nominal center of mass energy of 14 (5.5) TeV with luminosities up to $10^{34} \text{ cm}^{-2}\text{s}^{-1}$ ($10^{27} \text{ cm}^{-2}\text{s}^{-1}$). Thus, the LHC is the largest and most energetic particle accelerator ever built.

Along the ring of the LHC, there are four points of interaction, each one surrounded by a different detector with a different purpose. The ATLAS and the CMS are general purpose detectors, which perform a vast range of SM and BSM physics’ searches. The LHCb studies processes involving the bottom quark to search for hints of CP violation. Finally, ALICE is a detector suited for the study of Pb ions collisions.

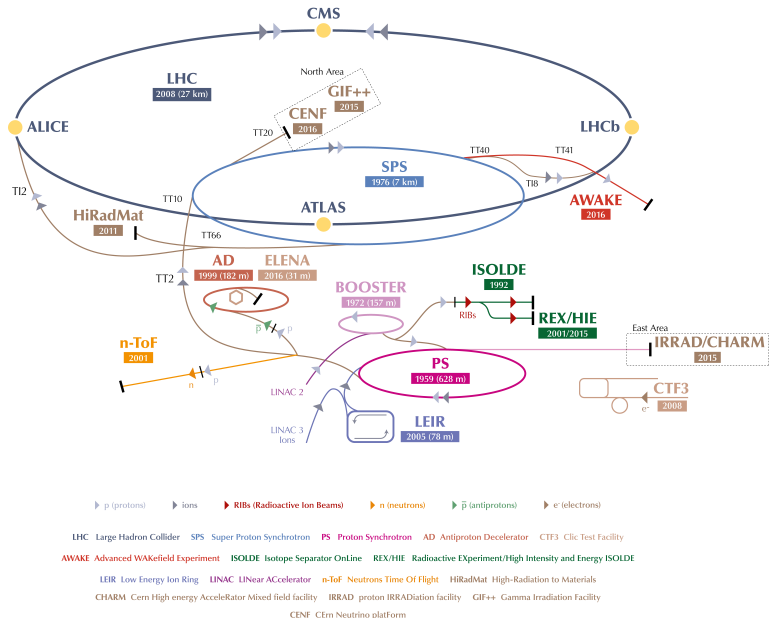


Figure 2.1: The LHC complex. From Ref. [24]

At the LHC, two opposite dipole magnetic fields are needed to bend the two counter-rotating beams of protons. Hence, two different pipes run along the ring, one for each of the two beams. The accelerator consists of eight straight sections (528 m each) plus eight long arc sections (2.9 km each). The collisions happen in four of these eight straight sections; each interaction point is surrounded by one of the four detectors described above. An 8 T magnetic dipole field is applied in the arc sections to bend the direction of protons. The magnets are constituted by Niobium-Titanium wires covered with Copper; they are maintained in the superconducting state at a temperature of 1.9 K by a cryogenic Helium-4 system. Magnetic quadrupoles are used to focus the beams in the center of the pipes along the LHC ring. Systems of three quadrupoles are located before any interaction points to adjust the beams' focalization. In this way, the rate of hard interactions is enhanced.

The protons in LHC are usually distributed in up to 2800 bunches of about 1.15×10^{11} protons. They travel along the ring with a nominal time distance of 25 ns from each other. Proton bunches are produced from ionized hydrogen atoms. They are accelerated up to 450 GeV by a system of machines (Linac2 - Proton Synchrotron Booster (PSB) - Proton Synchrotron (PS) - Super Proton Synchrotron (SPS)), as shown in Figure 2.1. Proton bunches are then injected into the LHC that increase their energy up to 7 TeV. The acceleration is performed using a 400 MHz superconducting cavity system, placed in one of the straight sections of the accelerator. When beams are stable, collisions happen at a rate time of 40 MHz.

The instantaneous luminosity L delivered by a colliding machine is a parameter

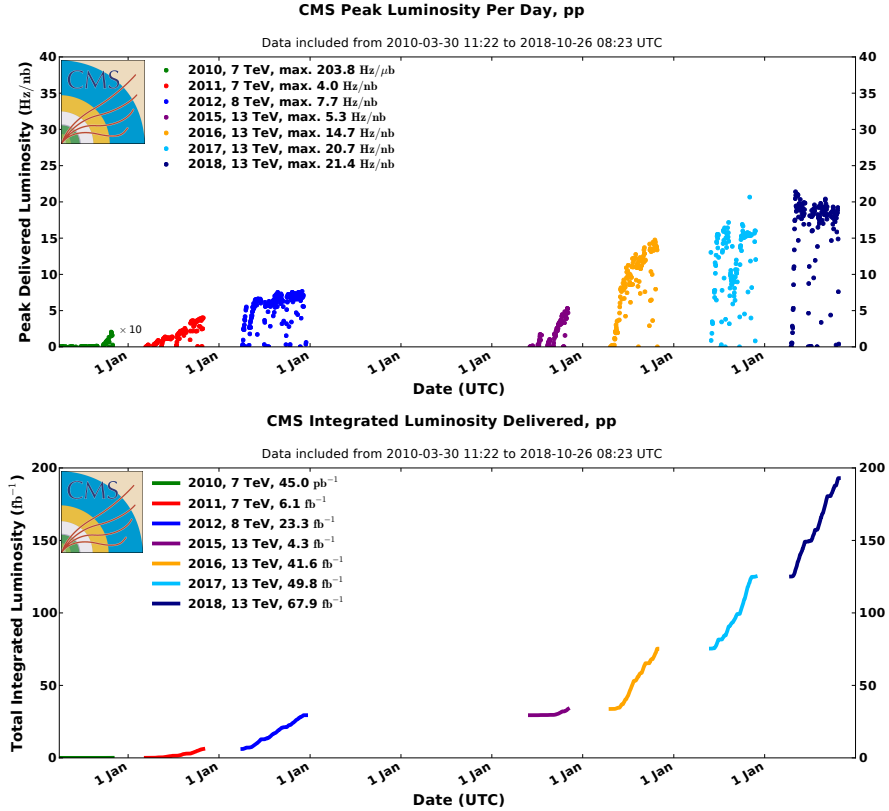


Figure 2.2: Top: Instantaneous luminosity versus day delivered by the LHC to CMS during pp collisions happening in the period from 2010 to 2018. Bottom: Integrated luminosity versus day delivered by the LHC to CMS during pp collisions happening in the period from 2010 to 2018. From Ref. [25].

defined as

$$\mathcal{L}\sigma = \frac{dN}{dt}, \quad (2.1)$$

where the σ and $\frac{dN}{dt}$ are the cross section and the observed rate of a certain scattering process, respectively. This parameter is related only to the characteristics of the circulating beams; it is one of the observables used to define the performance of a colliding machine since it expresses the rate of events of a process that the collider can produce. Integrating the instantaneous luminosity over time, one obtains the integrated luminosity L

$$L = \int_{t_0}^{t_1} \mathcal{L} dt = \frac{N}{\sigma}, \quad (2.2)$$

which is directly related to the number of events of a certain process collected in a period of LHC operation. The instantaneous and integrated luminosity delivered by the LHC machine in the 2010-2018 period are reported in Figure 2.2.

In each collision between two bunches of protons (bunch crossing), several interactions occur. The number of these interactions per crossing (pileup) is another important parameter that describes the LHC environment. Figure 2.3 shows the av-

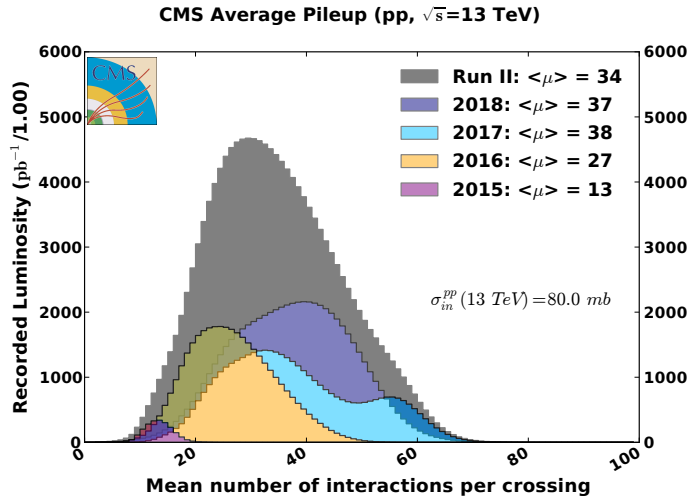


Figure 2.3: Distributions of the average number of interactions per crossing (pileup) for pp collisions for the 2011-2018 data sets. Distribution for all Run II is reported as well. The mean values of these distributions are reported and the minimum bias cross sections are shown. From Ref. [25].

verage number of interactions per bunch crossing measured by the CMS experiment during LHC data-taking. During Run II, about 20-40 simultaneous collisions occur in a bunch crossing on average.

The LHC plan for data-taking and maintenance is depicted in Figure 2.4. The data-taking periods (Run) are alternated by shutdown periods (LS), in which upgrades or maintenance of the detectors are made. The work of this thesis is based on the data sample accumulated during the period from 2016 to 2018. This period, called Run II, corresponds to an integrated luminosity of about 138 fb^{-1} . During the development of this thesis, the LS2 phase is ending; the processes to restart the LHC are ongoing. The beginning of Run III has been postponed to February 2022 because of the current issue related to the pandemics. After the conclusion of Run III, the third LS will take place. During this period, significant upgrades of the ATLAS and CMS detector will make the two detectors ready for the high luminosity (HL-LHC) phase. The HL-LHC will start taking data in 2026, accumulating an integrated luminosity about ten times higher than LHC one.

2.2 The Compact Muon Solenoid

The Compact Muon Solenoid (CMS) [27] is a multi-purpose detector surrounding one of the four interaction points of the LHC. The detector has a cylindrical shape, with a length of 21.6 m, a diameter of 14.6 m, and a total weight of 14000 tons. The CMS detector is made of different subdetectors; each one has a precise scope. The information deriving from the various pieces is combined to reconstruct the full kinematics of final state particles. In the nearest part to the collision point, the



Figure 2.4: LHC baseline plan of LS and Run. In the upper line, the collision energy is reported. In the lower line, the luminosity is shown. Because of Covid-19 restrictions, the beginning of Run III has been shifted to February 2022. From Ref. [26].

tracker system (made of silicon pixels and strips) registers the tracks of the charged particles (Sec. 2.2.1). The tracker is surrounded by an electromagnetic calorimeter and a hadronic calorimeter. The first measures the energy of electrons and photons (Sec. 2.2.2), while the latter measures hadrons' related observables (Sec. 2.2.3). These three detectors are located inside a superconducting solenoid of length 13 m and diameter 6 m, which provides a 3.8 T magnetic field that ensures the precise measurement of the momentum of even very high energy charged particles. Outside the solenoid, only the muon chambers are placed (Sec. 2.2.4). Here, the return magnetic field saturates the 1.5 m of iron of the holding structure, between which the muon stations are inserted. In figure Figure 2.5, a slice of the CMS detector with all its subdetectors is shown. In the following subsections, the various detectors are briefly described; for a detailed discussion on the CMS detector, see Ref. [27].

The CMS coordinate system sets its origin in the nominal interaction point inside the experiment. It is a right-handed coordinate system: the x-axis points radially toward the center of the LHC; the y-axis is directed vertically upward; finally, the z-axis lies on the beam direction. A spherical coordinate system (r, ϕ, θ) is chosen as it is suited to the detector's geometry. Here, r is the radial coordinate in the (x, y) transverse plane; ϕ is the azimuthal angle, measured from the x-axis in this plane; θ is the polar angle, measured from the z-axis along the beam direction. The pseudorapidity is defined as $\eta = -\ln(\tan \frac{\theta}{2})$ and is usually adopted instead of θ . Indeed, the scattering processes mediated by QCD, which are the most frequent interactions occurring at the LHC, have a distribution almost uniform in η . Moreover, for boosts along the z-axis, the pseudorapidity difference for massless particles is a Lorentz invariant quantity. In the (θ, ϕ) plane,

$$\Delta R = \sqrt{(\Delta\eta)^2 + (\Delta\phi)^2} \quad (2.3)$$

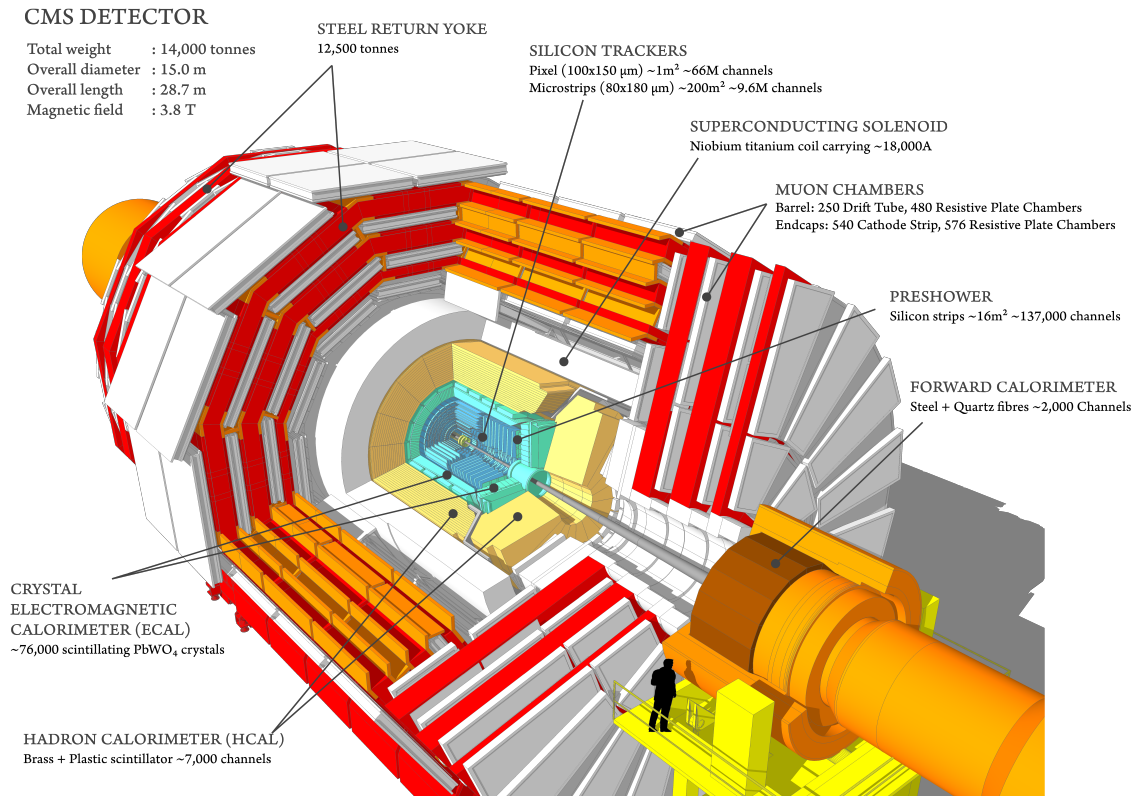


Figure 2.5: A view of the CMS detector and its main components [28].

expresses the angular separation of two particles. For boosts along the z-axis, this ΔR calculated for massless particles is a Lorentz invariant observable. In the transverse plane, the transverse momentum (p_T) and the transverse energy (E_T) denote the momentum projection in this plane and its magnitude, respectively; whereas p_T^{miss} indicates the momentum's imbalance measured in this plane.

2.2.1 Tracker

The inner tracking system of the CMS detector has a length of 5.8 m and a diameter of 2.5 m. A high spatial granularity and a fast response are qualities required to work in the LHC environment. Indeed, the tracker must precisely reconstruct the interaction vertex and secondary vertices; the latter is a fundamental requirement to tag the presence of b-hadrons. It is also expected to disentangle all the trajectories of charged particles and relate them precisely to the corresponding bunch crossing in a thorough environment. As mentioned in Section 2.2, the pileup during LHC operation may reach an average of order 50 simultaneous interactions per bunch crossing. Moreover, the high flux of particles damages the detector. Thus, a good radiation hardness is required. The silicon chosen to build the tracker provides all the three features mentioned above. The overall system operates at a temperature of -20 °C to reduce the radiation damage; the temperature is maintained constant by an efficient cooling system.

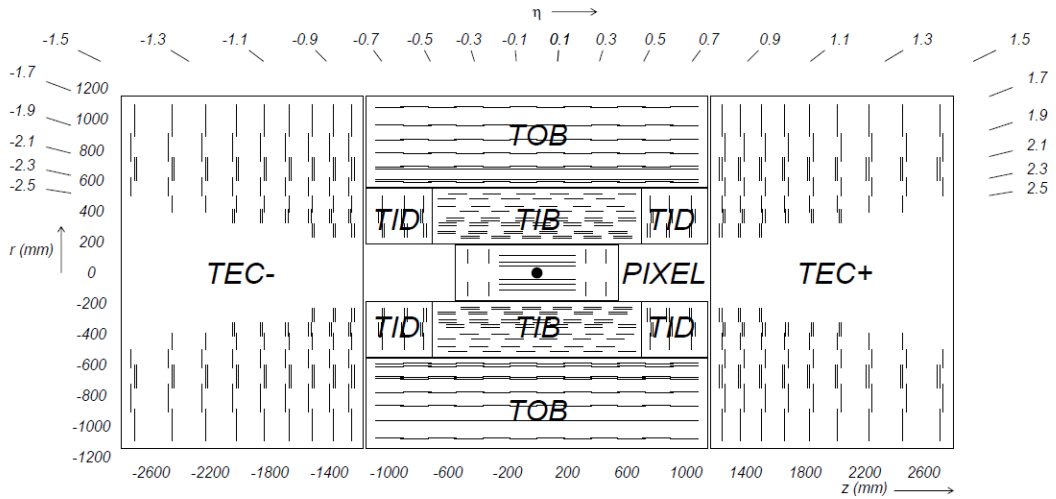


Figure 2.6: Schema of the inner tracker before the pixel update. The various substructures are shown: Tracker Inner Barrel and Disks (TIB/TID); the Tracker Outer Barrel (TOB); the Tracker EndCaps (TEC+ and TEC-). From Ref. [27].

The CMS tracker, reported in Figure 2.6, is constituted by a silicon pixel detector and a silicon strip detector. The whole detector contains 66 million pixels, covering an area of about 1 m^2 , and 9.3 million strips with a 198 m^2 of active silicon area. The whole apparatus reaches a coverage in pseudorapidity of 2.5.

In the nearest region to the interaction point, three cylindrical layers of silicon pixel detectors are mounted at radii of 4.4, 7.3, and 10.2 cm; two disks of pixel modules are placed on each endcap at the side of the cylinder. During the year-end technical stop of 2016/17, this pixel system has been replaced by four layers/three disks of low mass silicon pixels [29]. In the new detector, the innermost layer in the barrel is placed nearer to the origin ($r = 3 \text{ cm}$). Moreover, a fourth layer is added to the outermost layer in the barrel system; another pixel disk is added in each endcap. Thus, the new pixel detector provides higher efficiency and precision in reconstructing tracks and secondary vertices. Furthermore, this new asset reduces the amount of material in the tracking region.

The silicon strip tracker is located outside the pixel, in the region between $20 \text{ cm} < r < 116 \text{ cm}$; it is composed of three main parts: the Tracker Inner Barrel and Disks (TIB/TID); the Tracker Outer Barrel (TOB); the Tracker EndCaps (TEC+ and TEC- where the sign indicates the location along the z-axis). The TIB and TID cover the region up to $r=55 \text{ cm}$. The TIB contains four barrel layers, while the TID includes three disks positioned at each end of the barrel. The Tracker Outer Barrel (TOB) consists of six layers; the outermost is positioned at $r=116 \text{ cm}$. Finally, each TEC is arranged in nine disks, which increase the coverage in the z-direction up to 280 cm.

All the various barrel layers are made of silicon strips but with different thicknesses and lengths, depending on the distance from the interaction points. Inner

layers have finer strips with smaller dimensions. Moving toward the external layers, the space granularity of the strips reduces since the density of particles' tracks decreases. In this way, the average occupancy is maintained at about 2-3% per bunch crossing.

2.2.2 ECAL

The electromagnetic calorimeter of CMS (ECAL) is hermetic and homogeneous to provide an excellent energy resolution; 61200 lead tungstate (PbWO_4) crystals constitute the central barrel part (EB), while 7324 crystals form each of the two endcaps (EE). Moreover, a preshower detector (ES) is placed before each EE. Crystals are read out through avalanche photodiodes (APDs) in the barrel and vacuum photodiodes (VPTs) in the endcaps. As for the tracker, the ECAL was built to satisfy fast response, fine spatial granularity, and radiation hardness requirements.

The PbWO_4 was chosen since it has a high density (8.28 g/cm³), short radiation length ($X_0 = 0.89$ cm), and small Moli  r radius (2.2 cm); thus, it allows the construction of a compact calorimeter with a fine granularity. Moreover, about the 80% of the scintillation light is delivered in the first 25 ns. This time is compatible with the time distance of the LHC bunch crossings. The light output depends on temperature; at the operation temperature (18 °C), the emission is relatively low, corresponding to 4.5 photoelectrons per MeV. The scintillation light has a wavelength in the blue-green spectrum, with the maximum reached at 420–430 nm.

A schematic disposition of the various components of the ECAL is reported in Figure 2.7. The EB covers the pseudorapidity region up to $|\eta| = 1.479$. The barrel is made of 170 rings centered in the z direction; each ring is placed at a fixed η position and contains 360 crystals covering the ϕ angle. The total volume occupied by the crystals is 8.14 m³; their weight is 67.4 tons. The crystals have a length of 230 mm (equal to 25.8 X_0); they have a tapered shape with the front (rear) surface being 22×22 mm² (26×26 mm²). Crystals are arranged in a quasi-projective geometry; their axes form an angle of 3° with respect to the nominal interaction vertex. This disposition prevents the formation of gaps between crystals aligned with particle trajectories. Crystals are assembled in alveolar structures, called submodules; submodules are arranged in modules. Eventually, four modules are contained in a supermodule. There are 36 supermodules, each covering 20° in ϕ and containing 1700 crystals.

The EE extends in the region from $|\eta| = 1.479$ to $|\eta| = 3$; each endcap is divided into two Dees, where crystals are distributed along an x-y grid. The crystals have a length of 220mm (24.7 X_0) and a front (rear) surface of 28.62 × 28.62 mm² (30 × 30 mm²).

Finally, the preshower detector is a sampling calorimeter of two layers of silicon strip sensors (active element), which are preceded by two layers of lead (the absorber). Preshower is placed before each endcap, covering a pseudorapidity range of $1.653 < |\eta| < 2.6$ and having a thickness of 20 cm. This detector is used to identify photons deriving from the decay of neutral pions in the endcaps; moreover, it helps

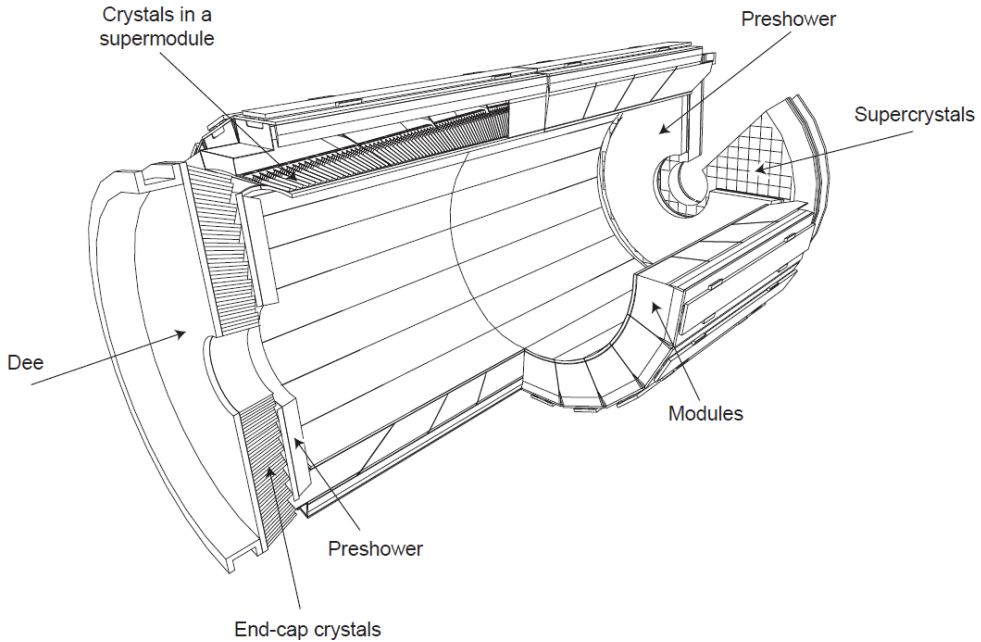


Figure 2.7: The layout of the ECAL. The barrel and the two endcaps plus the preshower are shown. From Ref. [27].

the position measurements of electrons and photons.

The energy resolution of a calorimeter can be expressed as the quadratic sum of three different terms, the stochastic term (S), the noise term (N), and the constant term (C), as follow

$$\left(\frac{\sigma_E}{E}\right)^2 = \left(\frac{N}{E}\right)^2 + \left(\frac{S}{\sqrt{E}}\right)^2 + C^2. \quad (2.4)$$

The values of these three terms were measured in a test beam with electrons before the data-taking [30] to be $S = 2.8\%$, $N = 12\%$, and $C = 0.3\%$. The formula above remains valid for energies below 500 GeV; after this threshold, the electromagnetic shower is not well contained in the calorimeter.

The stochastic term accounts for fluctuations in the lateral containment of the electromagnetic showers, possible variations in the number of photoelectrons emitted per GeV in APD or VPT, and the randomness of the energy deposited by the particle in the preshower absorber.

The noise term includes all the electronics, digitization, and pileup noise contributions. The electronic noise also includes the photodetector noise due to leakage current.

Finally, the non-uniformity of the longitudinal light collection and the imperfection of crystals' intercalibration contribute to the constant term. A small contribution also derives from the leakage of energy from the back of the crystal. All these effects do not depend on energy; thus, the constant term becomes the main

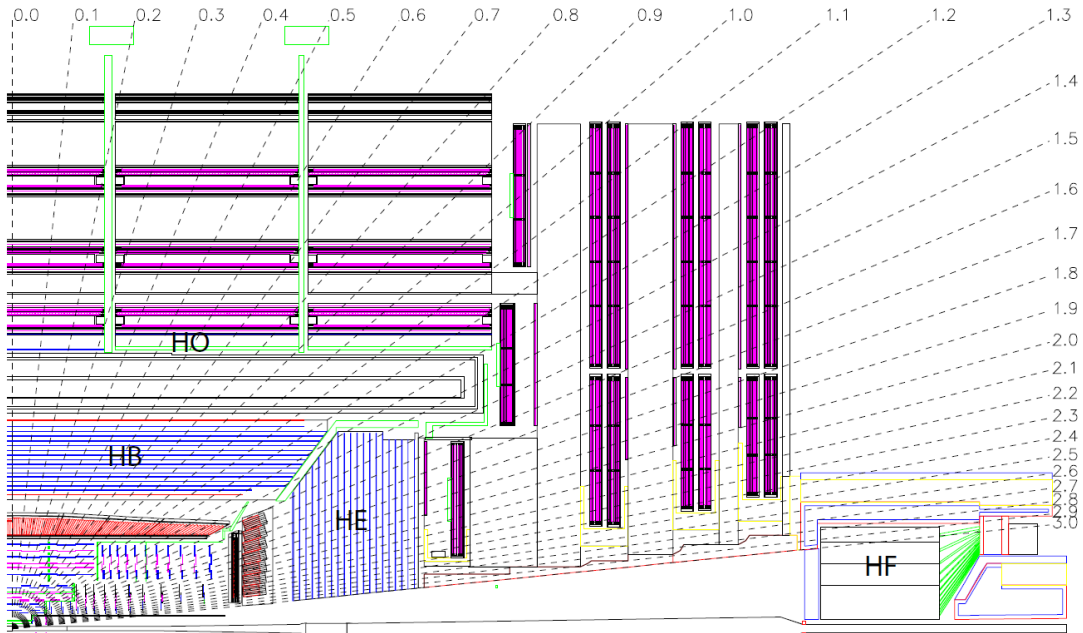


Figure 2.8: Longitudinal view of CMS, lines are drawn at fixed η . The four different subdetectors forming the HCAL are shown. From Ref. [27].

contribution in energy resolution at high energy. Hence, a precise calibration that standardizes the crystals' response is an essential step to achieve an excellent performance of the ECAL. The methods used to calibrate the crystals' response will be explained in Chapter 3.

2.2.3 HCAL

The CMS hadron calorimeter (HCAL) was designated to have high granularity. Indeed, the HCAL measures not only the energy of jets, but also their direction. As ECAL, the HCAL is a hermetic calorimeter to provide a good containment of hadronic showers. In this way, HCAL ensures estimation of the missing transverse energy, which is usually associated with the presence of neutral weakly interacting particles, such as neutrinos or even potential exotic particles.

Figure 2.8 shows the four subdetectors forming the HCAL system: the hadron calorimeter barrel (HB) and endcaps (HE), which are placed inside the solenoid magnet, covering a pseudorapidity region of $|\eta| < 1.3$ and $1.3 < |\eta| < 3$, respectively; the outer hadron calorimeter (HO) that covers the $|\eta| < 1.3$ region; the forward hadron calorimeter (HF) that extends rapidity coverage up to $|\eta| = 5.2$.

The hadron calorimeter barrel is a sampling calorimeter made of a brass absorber and a plastic scintillator, which is read out by wavelength shifters. The amount of the absorber material is limited since the HB must be inserted between the end of the ECAL system and the solenoid magnet coil. Thus, an additional sub-detector, the HO, is added outside the magnet coil in the same η region covered by HB to

ensure a satisfying shower containment. The HO uses the solenoid material as an absorber. The same plastic scintillator as HB is used as active material.

The HE is a sampling calorimeter inserted in the endcap iron yokes. It is made of layers of brass absorber alternated by a plastic scintillator as the HB.

Finally, the HF is a Cherenkov calorimeter of cylindrical shape; it is located at 11.2 m from the interaction point (calculated with respect to the cylinder's front face). The impressive dose of radiation in this high η region imposed restrictions on the material choice. Indeed, the material chosen must feature great radiation hardness. For this reason, the quartz fibers, read out by photomultipliers, are used as the active material. The absorber material chosen is steel. Due to its coverage of the high pseudorapidity region ($3 < |\eta| < 5.2$), the HF ensures a good identification of forward jets, which are the essential signature of VBS and VBF processes (cf. Sec. 1.2). Moreover, it also helps to have a more reliable measure of the p_T^{miss} .

The HCAL read-out system (both photodetectors and electronics) was upgraded during Run II [31] to improve the detector performance.

2.2.4 Muon Chambers

The muon system of CMS detector focuses on three main objectives: identification of muons, their momentum measurement, and triggering. It was designed to perform precise and robust muon measurements. Indeed, reliable muon identification and good momentum resolution over all the LHC energy and angles range, good dimuon mass resolution (about 1 % at 100 GeV), and reliable charge measurements of muons with $p < 1$ TeV were some of the requirements in the design project of CMS. The high magnetic field helps to achieve these requirements. Moreover, the magnet return yokes act also as further hadron absorbers, for hadron escaping the hadron calorimeter.

The muon momentum resolution reached using only the muon system is about 9 % for small values of η and p for transverse momenta up to 200 GeV [32]. Indeed, the presence of budget material before the muon station spoils the resolution as multiple scattering of muons occur before they reach the muon system. A 15% - 40% resolution, depending on $|\eta|$, is achieved for 1 TeV muons. Adding inner tracker information improves the performance. With this combination, at low p_T , the momentum resolution is improved by one order of magnitude, whereas at high p_T (1 TeV) goes down to 5% in the barrel region. The final optimization of the muon momentum resolution is achieved by an alignment system that measures the positions of the muon subsystems with respect to the other components of the CMS detector.

In the muon system, three different types of gaseous particle detectors are installed; they are arranged in the usual cylindrical shape: a barrel enclosed by two endcaps at each end. The disposition of the gaseous detectors is shown in Figure 2.9.

Drift chambers (DT) with standard rectangular drift cells are installed in the barrels to cover the pseudorapidity region of $|\eta| < 1.2$, where there is a uniform magnetic field, a low muon rate, and a small background contamination from neutrons.

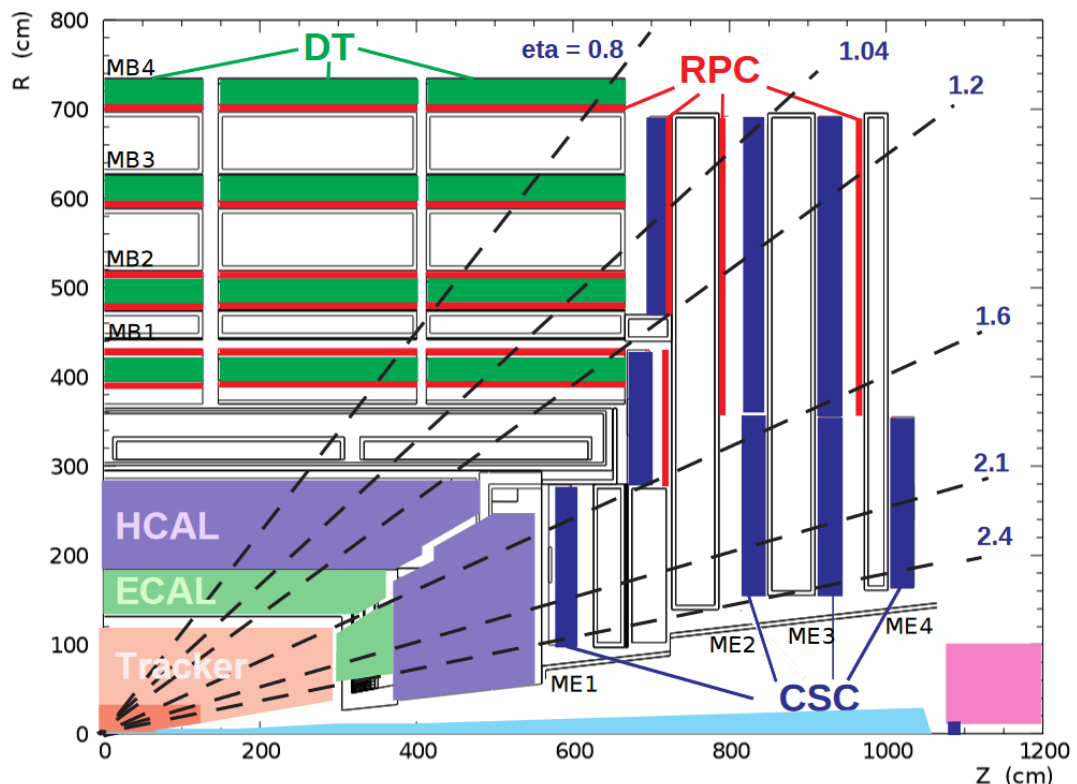


Figure 2.9: Longitudinal layout of one quadrant of the CMS detector. The four DT stations in the barrel (MB1–MB4, green), the four CSC stations in the endcap (ME1–ME4, blue), and the RPC stations (red) are shown. From Ref. [33]

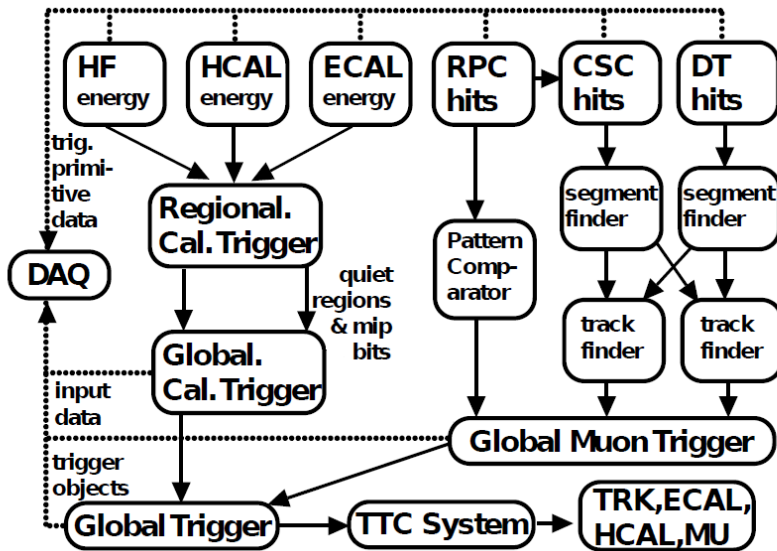


Figure 2.10: Schema of the L1 Trigger flow. From Ref. [34]

The DTs are assembled into four stations, which are inserted in the interspaces between the magnet yokes. These detectors provide muon time measurements with an excellent resolution.

The cathode strip chambers (CSC) are grouped into four stations disposed in each endcap, covering the region of $0.9 < |\eta| < 2.4$. They are suited to work in this region that has a large non-uniform magnetic field. Moreover, CSCs feature fast response time, fine granularity, and radiation hardness, which are necessary to deal with high muon rates, large background contamination, and high radiation dose. CSCs measure the η position and the crossing time of a muon.

The barrel and the endcaps are equipped with resistive plate chambers (RPC) up to $|\eta| < 1.6$. RPCs ensure an independent trigger system as they can provide a fast response and a good time resolution; they are avalanche-mode double-gap chambers, which guarantee good operation even at high rates. Six layers of RPCs are inserted in the barrel muon system, whereas three are placed in the endcap one. The redundancy is used to reduce the background contamination and thus, achieve the expected time and p_T resolution.

2.2.5 Trigger

The CMS trigger system reduces the very high rate of events originating from the LHC bunch crossings to an acceptable rate that can be safely stored. The reduction is performed in two steps, saving only interesting events. The Level-1 (L1) [35] trigger is the first step of filtering that reduces the rate to 100 kHz. After L1, the High-Level Trigger (HLT) [34] filters out more events, further decreasing the events rate down to 1 kHz. A software system, the Trigger Supervisor, controls the configuration and operation of the trigger components.

The L1 Trigger consists of a hardware system that analyzes every bunch crossing. It has a latency of about $4\ \mu\text{s}$; during this time, it analyzes raw data from the muon and calorimeters subsystem to decide if the event should be discarded or passed to the HLT trigger. As reported in Figure 2.10, the L1 Trigger has a hierarchical structure. The Local Triggers (or Trigger Primitive Generators) analyze energy deposits in calorimeter trigger towers or track segments and hit patterns in muon chambers. Data from the calorimeters are passed through two steps; they are aggregated by Regional Triggers (RTC) to form trigger objects, such as electrons, photons, or jets. These are then transferred to the global calorimeter trigger (GCT). Similarly, hits in the gas chambers of the muon system are analyzed through a pattern comparator or passed through segment finders and track finders. Muon candidates are transferred to the global muon trigger (GMT). Finally, the GCT and GMT convey the information to the global trigger (GT), which decides if the event must be discarded. The decision is transmitted to the subdetectors via the Timing, Trigger, and Control system.

Accepted events are then transferred to the HLT trigger, which decides if the event should be permanently stored. The HLT hardware is a farm made of thousands of computers; it performs calculations to reconstruct and identify objects from the complete set of data acquired by all the subdetectors. HLT applies some criteria, related to the needs of data analysis performed at LHC, to select only interesting events. The operations performed by the HLT are made through the so-called HLT paths, which are defined as sequences of processing steps involving both reconstruction and selection operations. Different paths can be specified, depending on the particular data analysis. Moreover, special HLT paths are defined to store data for calibration and monitoring purposes. An event accepted by an HLT path is permanently stored.

2.3 Event reconstruction

In the following section, the Particle Flow reconstruction algorithm (PF) [36] is briefly described; it allows a precise identification and reconstruction of the final state particles in the CMS environment. The CMS detector provides subdetectors with properties (described in Sec. 2.2) that are optimal for this algorithm to work. Indeed, PF algorithm exploits all the data deriving from the subdetectors to achieve the best performance in the reconstruction of jets, muons, electrons, photons; it also computes missing transverse momentum and performs tagging of jets containing b-hadrons. Moreover, this algorithm remains efficient in the case of several simultaneous interactions. Indeed, it can identify particles from these pileup vertices, which can be correctly subtracted from the interesting event.

The identification and reconstruction of physical objects start from the PF elements, which are the tracks in the tracker and muon stations and the clusters of energy in the calorimeters. Then the PF algorithm proceeds by connecting these fundamental elements to obtain PF blocks. The identification and reconstruction of different objects start from these PF blocks following a specific order. Muons are

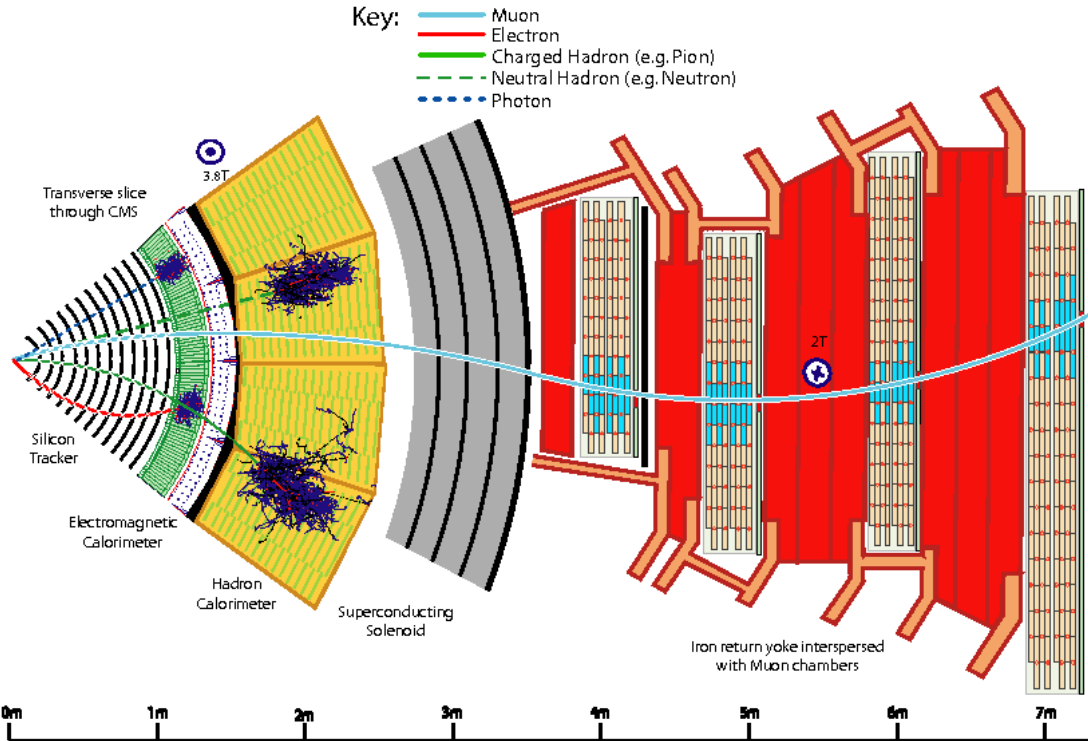


Figure 2.11: A slice of the CMS detector with a schematic representation of the particles' interaction. From Ref. [36].

identified and reconstructed linking tracks in the muon station with tracks in the inner tracker, as will be explained in Sec. 2.3.1; after this step, the PF elements associated with these muon candidates are subtracted from the PF blocks. Electrons are reconstructed by combining energy deposits in the ECAL with tracks in the silicon detector, as described in Sec. 2.3.2; tracks and energy clusters associated with electrons are then removed from the event. In the same step, isolated photons are identified as well. At this stage, as described in Sec. 2.3.3, using the information from HCAL in association with ECAL and tracker, neutral and charged hadrons are reconstructed and then merged to form the jets. Finally, the total imbalance of energy (Sec. 2.3.3) is calculated. A sketch representing the idea underneath the PF algorithm is reported in Figure 2.11.

2.3.1 Muons

Muons are categorized into three different types based on the approach used during their reconstruction [37]. “Standalone muons” are reconstructed only from hits in the muon stations, which are combined using a track finder exploiting Kalman filter technique [38]. The label “tracker muon” is applied to all candidates with a silicon tracker track that matches at least one segment in the DT or CSC muon stations. Finally, “global muons” have a track in the muon stations linked to a track of the

inner tracker. Muons may be reconstructed both as global and tracker muons; if they have the tracker track in common, the two objects are merged into a single one.

Standalone muons are contaminated by cosmic muons. Their momentum resolution is usually worse than the resolution of global or tracker muons; thus, they are usually not used at the analysis level.

Tracker muons have high efficiency for muons with low p_T , since this kind of muons is usually scattered from the material before muon station and does not reach the end of the muon system. Their purity is spoiled by the presence of hadron background since sometimes hadron showers may reach the innermost layer of the muon station.

Global muons are usually high p_T muons. They have a low misidentification rate since they combine both tracker and muon station information. The combination of information also reflects positively in the measurements of the momentum. In particular, global muons allow a more precise measure of p_T than tracker muons for $p_T > 200$ GeV.

Finally, the overall efficiency in the reconstruction of muons reaches 99% within the CMS geometrical acceptance.

2.3.2 Electrons

Electrons are built starting from an ECAL cluster of energy linked to a track in the silicon detector. When electrons interact with the tracker material budget, they may emit photons due to the bremsstrahlung effect. Electrons are deflected by the magnetic field. Thus, these photons are usually found along the ϕ direction, while the spread in the η direction is usually negligible. The energy of radiated photons must be considered to have a reliable measure of the electron's energy.

The reconstruction in the calorimeter starts from a crystal with energy over the threshold. All neighbor crystals satisfying some reasonable requirements are added, moving along the ϕ and η direction for the EB (or the x-y plane for the EE). Finally, superclusters are created, merging the initial reconstructed clusters. More details are discussed in Ref. [39].

In the tracker, the track reconstruction uses two different approaches depending on the amount of bremsstrahlung emission. The usual Kalman filter, which is used for all the charged particles, is applied when the bremsstrahlung emission is low. In the case of high energy loss due to this effect, the Gaussian Sum Filter [40] suits better since it can recover dislocated hits due to change in the electron direction.

Electrons can be reconstructed starting from either an ECAL supercluster or a GSF track. In the first case, the position of the ECAL SC (calculated as the weighted sum of all the crystals belonging to the SC) is extrapolated back to the tracker to see if it matches any track. A selection on the energy of the SC is applied to avoid confusion with hadrons, which can deposit energy in the electromagnetic calorimeter. Indeed, the ratio between the energy SC and the corresponding energy deposited in the HCAL must be less than 0.15; the energy computed in HCAL contains the

contributes of all the towers in a cone of $\Delta R = 0.15$ around the electron direction. The approach of the reconstruction starting from ECAL is used for high-energy electrons.

In the tracker-based case, the GSF track is extrapolated to match an ECAL supercluster. This method is adopted to guarantee high efficiency and accuracy in the reconstruction of either low p_T or nonisolated electrons.

Finally, the momentum resolution of electrons varies from 1.7%-4.5%; the reconstruction efficiency varies from 88% to 98% (from 90% to 96%) in the barrel (endcaps) in the p_T range from 10 to 100 GeV. These values depend on the electron η position and the amount of bremsstrahlung emission [39].

2.3.3 Jets and missing transverse momentum

After muons, electrons and photons are reconstructed, their tracks and clusters are removed from the event. The left tracks and clusters are attributed to hadron (charged or neutral) and nonisolated photons, which constitute the basic elements of jets.

Photons and hadrons are reconstructed from ECAL and HCAL clusters. Within tracker coverage ($|\eta| < 2.5$), HCAL clusters associated with a track are related to charged hadrons; ECAL clusters without any match in the tracker are classified as photons; HCAL clusters without any link to a track are attributed to neutral hadrons. In the region not covered by the tracker ($|\eta| > 2.5$), ECAL clusters associated with an HCAL cluster are related to hadrons (either neutral or charged), whereas ECAL clusters only (without any link to HCAL clusters) are identified as photons.

Jets are assembled from these PF candidates through the anti- k_T algorithm [41, 42] with a distance parameter $R = 0.4$ (AK4 jets). The p_T of an AK4 jet is the vectorial sum of p_T of all the PF candidates contained in it.

Jet energy scale corrections (JEC) are obtained from data and simulated samples as a function of η and p_T . These corrections are needed to account for pileup effects and uniformity in detector response; they also adjust additional differences, which may arise in the jet energy scale between data and simulations. The achieved resolution in measuring jet energy depends on the jet energy itself and its η position; in the central region of the CMS barrel, jet energy resolutions are 15-20% at 30 GeV, about 10% at 100 GeV, and 5% at 1 TeV [43].

After all the PF candidates are reconstructed, the negative sum of their p_T is computed. This quantity, called missing transverse momentum (p_T^{miss}) [44], accounts for the presence of undetectable particles, such as neutrinos. The experimental resolutions, the misreconstruction of particles, the non-hermeticity of the detector, and the presence of other non-primary vertices are among the main things affecting the p_T^{miss} measured value. Thus, these effects have been studied in data and simulated samples [44] to improve the reconstruction efficiency and the precision of p_T^{miss} . A precise measurement of p_T^{miss} is of particular interest for the analysis carried on during this thesis work since the leptonic final state of W bosons is involved.

3 Calibration of the electromagnetic calorimeter

As already mentioned in Section 2.2.2, the ECAL is crucial not only in the reconstruction of photons and electrons but plays an important role also in the reconstruction of jets since it measures the electromagnetic component of their shower. Hence, it is of primary interest that these measurements are the most accurate and efficient. Indeed, the correct reconstruction of every object guarantees the goodness and reliability of each analysis within the CMS Collaboration. Excellent calibration of the detector is essential to achieve the best performance.

In this section, the work needed to calibrate the ECAL is summarized, showing how the energy of each crystal is computed (Sec. 3.1) and why time and space-dependent corrections are needed (Sec. 3.2). Finally, a new method (Sec. 3.3) that will be implemented in Run III to monitor, stabilize, and equalize crystals' response is shown. This method, called energy flow (EFlow), was developed during this work.

3.1 Energy reconstruction

When a particle interacts in the ECAL, it deposits energy in a bunch of crystals. The energy of each crystal is reconstructed as follow:

$$E_{ch}[\text{GeV}] = A[\text{ADC}] \times G[\text{GeV}/\text{ADC}] \times LC_{ch}(t) \times IC_{ch} \quad (3.1)$$

where

- A_{ch} is the reconstructed amplitude of the signal in the crystal, expressed in ADC counts;
- G is the factor used to convert ADC counts in energy (measured in GeV); this factor amounts to about 40 MeV/ADC in EB and 60 MeV/ADC in EE; this value is estimated before any radiation damage.
- $LC_{ch}(t)$ are the laser corrections; they account for the losses in response of crystals and photodetectors due to irradiation; they are time-dependent corrections, estimated separately for each crystal.
- IC_{ch} are the intercalibration constants; they equalize the response among crystals located in different positions of the ECAL.

The scintillation light emitted by a PbWO₄ crystal is collected by photodetectors, which provide an analogical electrical signal. This signal is amplified and digitalized through a multigain preamplifier (MGPA) with three different ADC gains (x1, x6, x12). The choice of the gain is performed dynamically; the highest gain, in which the pulse is not saturated, is automatically chosen. In this way, the energy range covered for a single channel spans from 35 MeV up to 1.7 (2.8) TeV in the barrel (endcaps). The pulse is then acquired with a frequency of 40 MHz as ten consecutive samples spaced in time by 25 ns. The pulse starts on the fourth of these samples and reaches its amplitude maximum on the sixth one; the first three samples could be used to determine the pedestal that will be subtracted from each signal.

From this set of ten samples, the amplitude of the ECAL crystal is reconstructed through the multifit algorithm [45]. The multifit algorithm was introduced at the beginning of Run II to reduce the contamination of signals coming from different bunch crossings within the acquisition window. Indeed, the overlap of these out-of-time (OOT) signals to the in-time one (IT) worsens the energy resolution of the ECAL. The multifit algorithm determines simultaneously through a χ^2 minimization the amplitudes of up to ten consecutive templates shifted by intervals of 25 ns. In this way, it may disentangle the contribution of IT signal from the OOT ones. The shape of the templates is identical and is measured directly from data. Indeed, the templates are obtained for each crystal using events from the collisions of isolated bunches, i.e. bunches inserted in the filling scheme with bigger time spacing than the usual 25 ns one. When two isolated bunches collide, no OOT pileup contribution is present. From these particular bunch crossings, random events are selected by dedicated HLT paths. Their weighted average pulse normalized to the same amplitude is taken as the IT signal template. OOT templates have the same shape as the IT signal one but are shifted in time. An example of this multifit procedure is reported in Figure 3.1 for the barrel (left) and the endcap (right). All the templates (dashed and dotted lines) contributing to the measured pulse (black circles) are shown. Their amplitude, constrained to be positive, is extracted by the multifit algorithm. The sum of all the OOT and IT signal contributions is superimposed as the blue solid line histograms. The red dashed line, peaking at the sixth sample acquired, represents the IT signal. Its amplitude is assigned as the amplitude of the measured pulse.

When at least one of the ten digitalized samples is amplified through the x6 or x1 gain, a small non-linearity in electronics distorts the signal shape, making the use of the multifit algorithm not possible. However, these pulses have a negligible OOT contribution. Therefore, their IT signal can be estimated as the difference between the sixth sample amplitude and the pedestal.

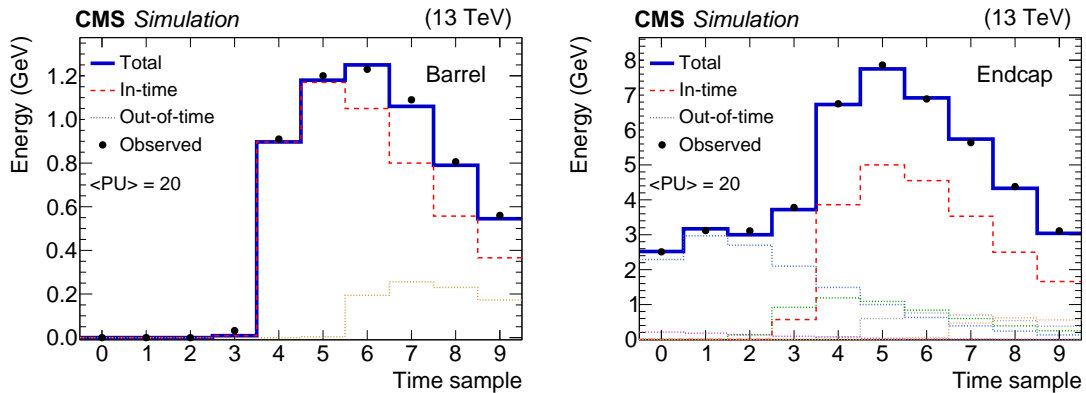


Figure 3.1: Example of a pulse fitted with the multifit algorithm in barrel (left) and endcap (right). Events are simulated with 20 average pileup interactions and 25 ns bunch spacing. Black circles with error bars represent the ten samples acquired. The red dashed histogram shows the fitted IT signal, while the colored dotted histograms show the contributions of OOT signals. The solid blue histograms represent the sum of all the fitted signal templates. From Ref. [45]

3.2 Response monitoring and calibration methods

During the LHC operation, the PbWO₄ crystals are subjected to radiation damage due to both electromagnetic and hadronic interactions [46]. Electromagnetic interactions cause the formation of color centers in the crystals, which cause a reduction of the crystal transparency. However, this electromagnetic damage is largely cured at the ECAL operating temperature thanks to the spontaneous annealing of these centers. The hadron-induced damage has a more serious impact on the crystals than the electromagnetic one. Indeed, it produces a shift of the transmission band that provokes huge losses in light transmission. Moreover, this kind of damage is not recoverable in time; it only accumulates during the data-taking.

A high-precision light monitoring system (LM) [47] is used to track changes in the crystal response during LHC operation. It is also used to extract the correction factor LC_{ch} to adjust the crystal response and prevent the degradation of the ECAL resolution. Laser light of 447 nm wavelength is injected every 40 minutes at a fixed position at the crystal's front (rear) face and collected by the APD (VPT) of the crystal's rear face in the EB (EE). The laser pulse injected in each crystal is controlled by a PN photodiode, which is usually associated with a set of 100-200 crystals, called a harness. In this way, the measured response does not depend on the possible fluctuations of the injected light. Indeed, the crystal relative response to laser light is computed as the amplitude (\mathcal{A}) of the photodetector signal normalized to the one measured by the PN diode as

$$R_{ch} = \mathcal{A}_{APD}/\mathcal{A}_{PN}. \quad (3.2)$$

In Figure 3.2, the relative response of the ECAL crystals to the laser light as a

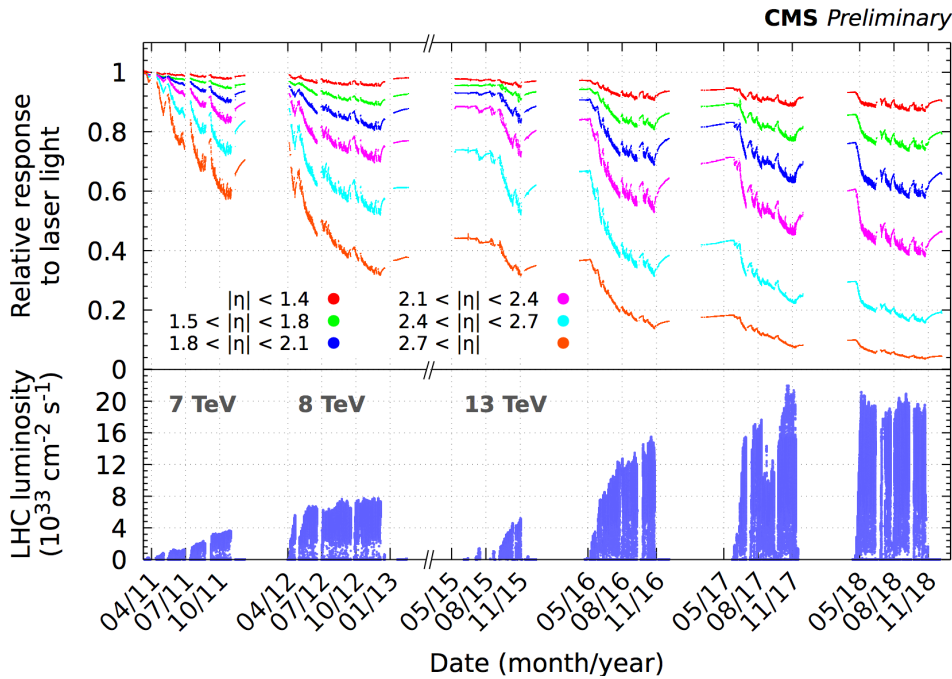


Figure 3.2: Average of the relative response to laser light injected in the ECAL crystals, measured by the ECAL LM system. The average response is obtained mediating over all the crystals in an interval of pseudorapidity, represented by different colors. In the plot, 2011, 2012, 2015, 2016, 2017, 2018 data-taking periods are reported. In the bottom panel, the instantaneous luminosity delivered by LHC is shown. Figure from Ref. [48]

function of time is shown. Different colors represent several pseudorapidity intervals. The change of relative response to laser light during the years is visible; it is more pronounced for crystals in the region near the beam line that receives a higher dose of radiation. In particular, the variation observed in the ECAL channels is up to 10% in the barrel; it grows up to 62% at the limit of the tracker acceptance ($|\eta| < 2.5$). Finally, it reaches 96% in the region closest to the beam pipe. The recovery of the crystals' transparency during the periods without collisions is also visible.

The LM system estimates the response variation of the crystals every 40 minutes to correct for losses in their transparency. The laser corrections are derived for each crystal as a function of time

$$LC_{ch}(t) = \left[\frac{R_{ch}(0)}{R_{ch}(t)} \right]^\alpha,$$

where $R_{ch}(t)$ and $R_{ch}(0)$ are the response of the crystal to laser light at time t and the beginning of the data-taking of each year ($t=0$), and α is a parameter that considers the different paths of laser and scintillation light. The α -parameter has an average value of about 1.5 in EB and 1 in EE. These values, which depend on the specific readout configurations and the crystal's properties, were measured in a test beam before the data-taking and then refined during it to account for transparency losses, using data from the Z boson decay into electrons.

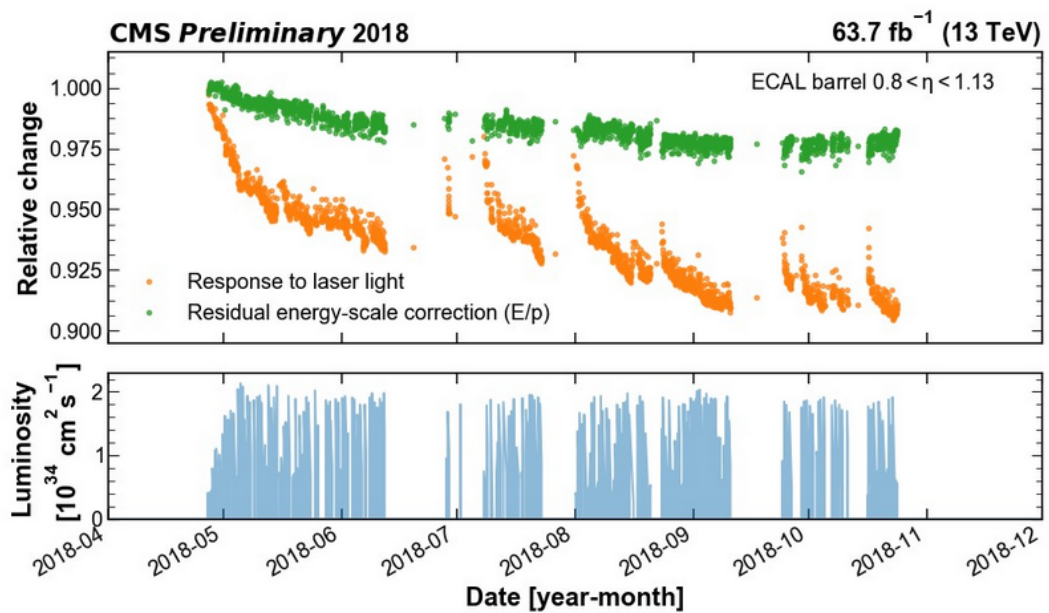


Figure 3.3: Relative change in the response of the crystals in time for a module of the ECAL in the pseudorapidity range $0.8 < \eta < 1.13$. The orange points represent the response to laser light, whereas the green ones show the residual energy-scale evolution, computed as the energy measured by the ECAL (with the laser corrections applied) normalized to the momentum measured by the tracker. In the bottom panel, the instantaneous luminosity is drawn. From Ref. [49].

In Figure 3.3, after the laser corrections, a residual drift of the energy-scale in time, measured as the energy (ECAL) over the momentum (tracker), is still visible (green dots); the effect is up to a few percent per year in the barrel. The causes of this residual drift are still under investigation, but a coherent behavior is observed in crystals belonging to the same harness, indicating that it can be a consequence of the irradiation of the PN photodiodes. Indeed, during the operation of LHC, the PN photodiodes may be subject to radiation damage that causes a reduction in their light emission; in this scenario, a bias is induced in the laser correction, since PN diodes provide the reference to the APD measurements of the injected laser light. This hypothesis explains the residual regional drift of the energy scale that was first observed during the 2016 data-taking; an effective correction for Run II data was extracted using the E/p method, as will be explained in Sec. 3.3.1.

After the time-dependent part of the calibration is applied, an intercalibration is needed to equalize the response of crystals at the same pseudorapidity coordinate. The methods used to derive these intercalibrations (ICs) are the π^0 , the E/p , the Zee, and the ϕ -symmetry. The ICs are derived using the data sample accumulated over one year of data-taking. These four methods are complementary as they use different data samples and techniques. Together they provide a way to achieve adequate stability in response and a fine enough energy resolution, which guarantee optimal performance of the ECAL detector. The π^0 method selects events requiring two photons in a window of invariant mass compatible with the mass of the π^0 ; the intercalibration factor is derived comparing the measured and the nominal π^0 mass. The E/p method compares the energy measured in the ECAL to the transverse momentum measured in the tracker for high-energy electrons deriving from W (Z) boson decay. The Zee method uses the invariant mass of electrons from Z boson decay. The ϕ -symmetry intercalibration (Sec. 3.2.1) exploits minimum bias events produced in low energy collisions, which are expected to have an energy distribution uniform in ϕ . The methods based on electrons (E/p and Zee) are the most precise in providing intercalibrations due to the purity of the sample used. The intercalibrations derived with different calibration methods are combined as a weighted sum; the weight chosen is the relative IC precision of each method.

Finally, the absolute energy scale is derived and applied as a function of η to equalize the response of the different η regions. The absolute energy scale is derived with events from Z decay into electrons, imposing that the observed invariant mass for electrons reconstructed in data matches the Monte Carlo simulation in all the different η -rings.

3.2.1 The ϕ -symmetry method

The ϕ -symmetry method extracts the ICs from events in low energy proton-proton interactions, which preserve the azimuthal symmetry of the energy distribution. In the limit of a large sample of these low energy events, the energy deposited in crystals belonging to the same η -ring of the ECAL is expected to be, on average, the same. Thus, the ratio between the transverse energy deposited in the specific crystal E_T^{ch}

and the average transverse energy deposited in the corresponding η -ring $\sum_j E_T^j/N$ is computed to correct for any possible deviation in the response of different crystals, through the following formula

$$IC_{ch} = \frac{\sum_j E_T^j/N}{E_T^{ch}} \cdot \kappa, \quad (3.3)$$

where the κ accounts for the limited energy window of the events, as will be explained in the text below.

Events used by the ϕ -symmetry are selected by a specific CMS trigger that allows one to save a higher number of events by reducing the information collected; for each event, only signals from the ECAL crystals above a certain energy threshold are stored, without using the information from the other detectors. At the L1 trigger, no specific requirements on detector activity are imposed to exclude a calibration bias; random events from the various bunch crossings are selected. The rate of this trigger can be scaled to match the desired bandwidth. The HLT selects events where at least one ECAL crystal has an energy above 7 times the expected noise. In this way, the ϕ -symmetry trigger rate spans from 2 kHz (during standard data-taking) up to 30 kHz (during commissioning periods), whereas standard physics triggers have about 1 kHz rate (cf. Sec. 2.2.5). An offline selection of events is performed, tightening the energy threshold up to 10 times the RMS noise. Moreover, an upper energy threshold is applied to exclude rare events from hard interactions, which may induce bias in the calibration. The window in energy selected has a range of 1 GeV.

The κ -parameter, mentioned above, is a correction factor to account for the migration of events outside the selected energy window induced by mis-calibration. This threshold effect is shown in the left panel of Fig. 3.4, where an applied mis-calibration of $\pm 5\%$ produces a shift of the energy spectrum (red and green histograms) and consequently a fall of events outside the boundaries of the selected energy interval. For each crystal, a set of known mis-calibrations is introduced in the data. Thus, the observed mis-calibrations are derived from the ratio of the IC calculated with and without mis-calibrations applied. The plot of these observed mis-calibrations versus the true ones is reported in Figure 3.4. A linear fit is performed to extract the slope, which is the κ -factor; its typical values are between 2 and 2.5.

The ϕ -symmetry method is used to derive the IC constants and monitor the transparency loss during data-taking.

However, additional corrections are needed to account for the tracker services and support structure, which are placed in front of the ECAL. These constitute a non-uniform material budget that absorbs part of the particles' radiation. Thus, the ECAL crystals behind these structures systematically measure less energy than the others in the corresponding η -ring, causing an artificial enhancement of their ICs. In the EB, these structures are placed at fixed ϕ , causing a relative effect on the ICs constant in η . Hence, a correction factor can be calculated from data for the EB to restore the real IC values. On the contrary, EE corrections can not be derived because of the different positions and geometry of the structures.

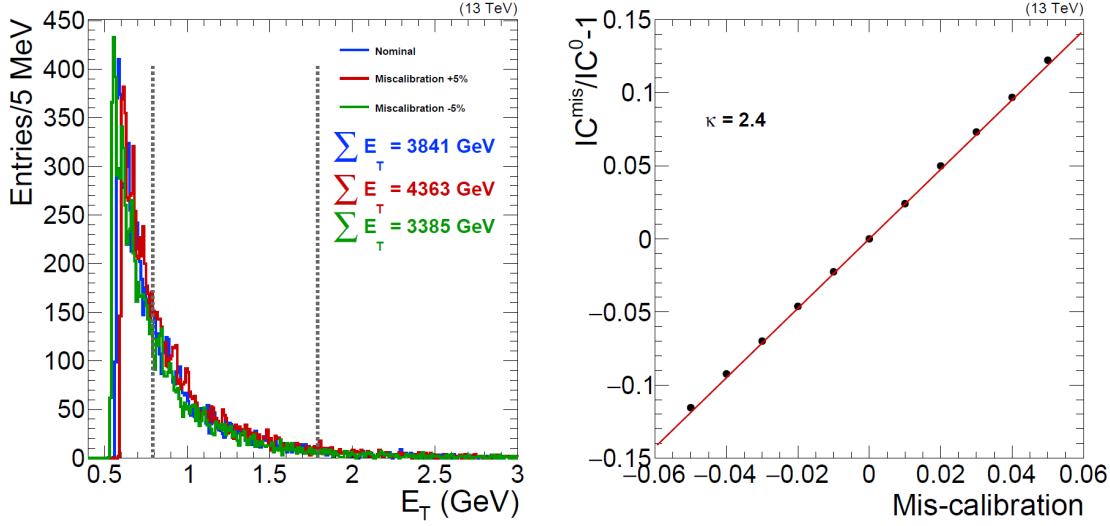


Figure 3.4: On the left panel, the energy spectrum of events selected by the ϕ -symmetry HLT path in a crystal of the central EB. The blue histogram represents the measured energy spectrum; the red and green ones are obtained from the blue histogram by introducing a mis-calibration of $\pm 5\%$. Vertical lines are the bounds of the energy interval selected. For each histogram, the sum of the energy of the selected events is also reported. On the right panel, a typical fit to extract the κ -factor. The x-axis is the injected mis-calibration, while the y-axis is the observed mis-calibration, computed as the variation in the IC constant with a given mis-calibration, minus one. The red line is the linear fit. The κ -factor is the slope of this red line; its value is reported in the same figure.

The ϕ -symmetry method reaches a statistical precision better than 0.5% with an integrated luminosity of 0.5 fb^{-1} . However, its total precision is dominated by systematic uncertainties related to the material budget in front of the ECAL. Thus, the precision of the method is around $2 - 5\%$ (depending on η). During Run II, ϕ -symmetry was mainly used as a cross-check of the other methods' performance, since its uncertainty on intercalibration is much larger than the other methods, which have precision around $0.5 - 1.5\%$.

During data-taking, the ϕ -symmetry can be used to check the performance of the laser correction. The data are divided into time intervals, such that a large number of events is collected in each crystal. The ICs are then computed for each crystal in these several time intervals with Eq. 3.3. The ratio between the IC in a given time interval and a reference value, usually the first time interval of each year, is considered. In this way, the effect of the material structure in front of ECAL, constant in time, cancels out, and the method provides a reliable way to monitor the evolution in time of the ECAL calibration with crystal granularity.

3.3 The EFlow method for the regional energy drift corrections

In this section, a new intercalibration method is presented; it aims to correct the residual energy drift due to PN aging. As already explained in Sec. 3.2, after the laser corrections are applied, a residual regional drift is visible during the data-takings. For the Run II data sample, corrections to this behavior were extracted thanks to the E/p method, as will be explained in Sec. 3.3.1. A novel method, called EFlow, exploits an idea similar to the ϕ -symmetry one (Sec. 3.2.1) to correct for the residual regional drift. The method, described in Sec. 3.3.2, allows per-crystal monitoring of the light response with granularity in time of the order of 1-2 days; its performance is derived and compared with the baseline from E/p correction (Sec. 3.3.3).

3.3.1 The Run II regional energy drift corrections

The residual drift due to PN irradiation is monitored using the E/p method; an effective correction with the per-harness granularity is implemented and applied to Run II events. As mentioned in Section 3.2, the E/p method uses events with electrons from the W and Z boson decay. The HLT trigger selects events with one or two-electron candidates to obtain a sample of $W \rightarrow e\nu$ and $Z \rightarrow e^+e^-$ events, respectively. A set of selections, including electron identification and isolation criteria and some cuts on the events' kinematics, is applied to increase the purity of these samples. The distribution of the E/p for electrons belonging to a specific harness is fitted with a template to obtain the relative energy scale; a different template for each harness η interval is obtained through data in each data-taking period since the E/p distribution depends on η (cf. Fig. 3.5). The relative energy scale measured with E/p is then expressed as a function of the integrated luminosity and fitted through a linear function to extract the corrections for the crystals in the harness; an example is reported in the right panel of Figure 3.5.

3.3.2 Regional energy drift corrections with EFlow + global scale

For Run III, another method has been studied to correct the residual regional drift in the energy scale. This method constitutes an alternative to the per-harness correction that was implemented in Run II with E/p.

The new method consists of two different steps. Firstly, a local correction, which has a per-crystal granularity, is applied to equalize the response of the crystals. Secondly, a global correction (the same for all the EB crystals) is applied to restore the original light response and adjust the global energy scale.

As mentioned in Sec. 3.2, the observed drift is supposed to be related to radiation damage of the PN diodes. Hence, since the dose of radiation absorbed depends mostly on η , crystals belonging to different harnesses (placed at different η) experience a different degradation of light response. The energy flow (EFlow) method

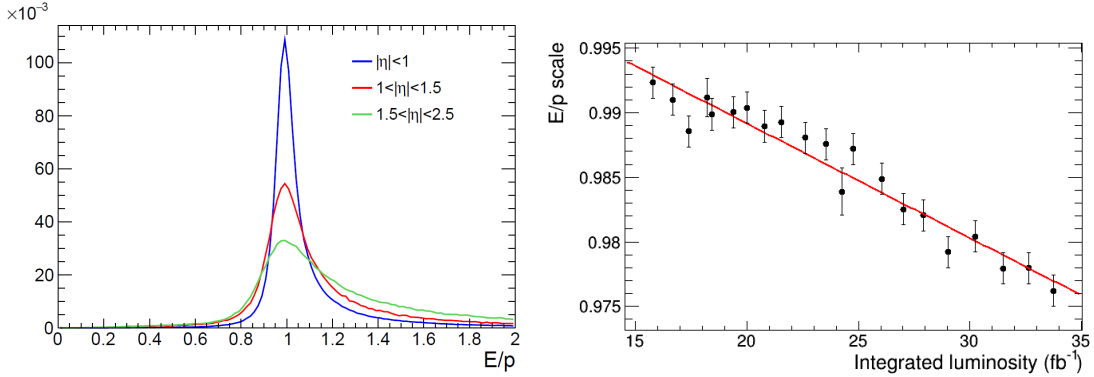


Figure 3.5: On the left, E/p distributions from data in different intervals of pseudorapidity. On the right, the relative energy scale of the E/p for electrons from W and Z bosons decay as a function of the integrated luminosity for one harness. The red line represents the linear fit to the points; the linear fit is used to extract the corrections.

is used to derive time-dependent ICs to standardize each crystal’s residual loss to the average loss of the barrel. The EFlow method relies on minimum bias events, selected with the same requirements of the ϕ -symmetry (Sec. 3.2.1); the energy deposited in a single crystal is normalized to the average energy computed considering all the crystals in the barrel. ICs are thus calculated in several times intervals, of about 1-2 days of duration, through a formula similar to Eq. 3.3

$$IC_{ch} = \frac{\sum_{j,EB} w_j(\eta) E_T^j / N}{E_T^{ch}} \cdot \kappa, \quad (3.4)$$

where now the sum $\sum_{j,EB} E_T^j$ extends over all the N crystals of the EB.

Moreover, the crystal’s energy in the total sum of the barrel is multiplied by a weight ($w_j(\eta)$), which is inversely proportional to the number of electrons collected in the η -ring in events with W/Z bosons. These weights are inserted to compare the results from minimum bias events, which have a flat distribution in η , with the results from events containing electrons from Z (W) boson decay. Indeed, after the EFlow corrections are applied, either the E/p or the Zee method must be used to adjust the global drift of the barrel, as will be explained below.

In Figure 3.6, the E/p relative energy scale versus time (red dots) is shown for two harnesses, which have different degradations of response during data-taking; in particular, the left one has a more pronounced residual loss than the right one. The objective of the EFlow calibration is equalize the drift in time. Hence, the corrections are derived with respect to the average energy of the barrel with the formula in Equation 3.4. The EFlow ICs (blue dots) are normalized to the IC of the first time interval. The IC ratios derived with EFlow for the harness in the left panel are greater than one, suggesting that the residual loss for that particular harness is more than the average of the barrel. On the contrary, ICs in the right plot are smaller than one, indicating that the the residual loss of the harness is less than the barrel average.

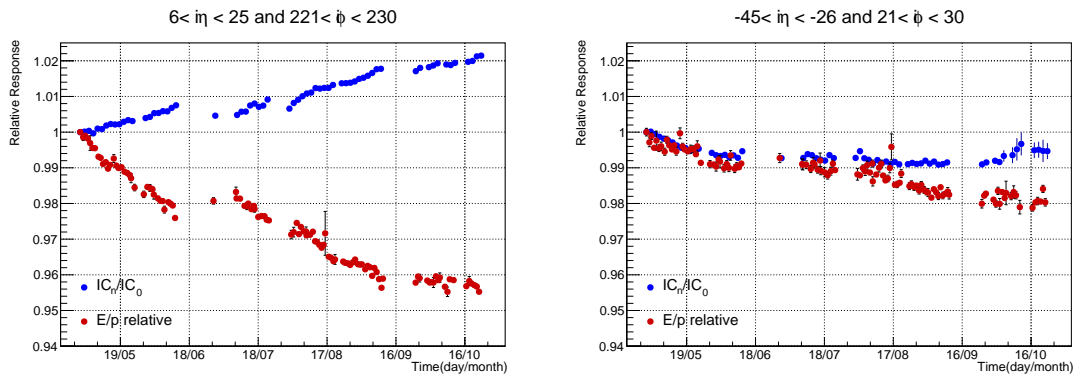


Figure 3.6: The relative light response as a function of time in two different harnesses for the 2018 data-taking period. Blue dots show the ICs of the EFlow method (normalized to the IC calculated in the first time interval) versus time. Red dots show the E/p relative energy scale. The harness shown in the left panel has a more pronounced residual loss than the average of the barrel, whereas the one in the right panel experiences a minor residual loss with respect to the barrel mean.

After EFlow corrections are applied, all the crystals show a similar trend of the residual loss in time; the average drift of the barrel is still to be corrected. However, the EFlow method is blind to this global effect for construction; thus, it can not be exploited to this scope. Another method, based on electrons from the W/Z boson decays, is used to adjust the global energy scale. Figure 3.7 shows the relative energy-scale of the barrel (measured with E/p) over time; as expected, a decrease in time is observed as a consequence of the radiation damage of the PN. An empirical correction can be extracted as the inverse of the value of each point to restore to one the relative light response in each time interval.

In Figure 3.8, the relative response of two harnesses (the same of Figure 3.6) is monitored with the E/p method. The blue dots show the relative response of the harnesses before any correction is applied. After the application of the per-crystal EFlow ICs, crystals' response is equalized; indeed, the red dots in the left and right panels show a similar trend. Finally, the green dots show the final result of the calibration as a closure test of the method. The global scale correction obtained with the E/p method makes the trend over time constant; the relative response of the crystals is equal to one, as expected.

A closure test has been performed to assess the consistency of the EFlow plus global scale method. Corrections are extracted for the 2018 data sample with all the space and time calibrations applied except the E/p corrections for PN-drift.

The slope of the relative response versus time is obtained for each harness through a linear fit. This observable is used to monitor the correct functioning of the method. Another observable used is the RMS of the energy scale distribution of all the harnesses in a defined time interval. The results of the closure test performed are reported in Figure 3.9. In the left panel, the slopes of the harnesses before and after the corrections are reported. As expected, after the EFlow corrections (red histogram), the RMS of the distribution of the slopes is highly reduced; the appli-

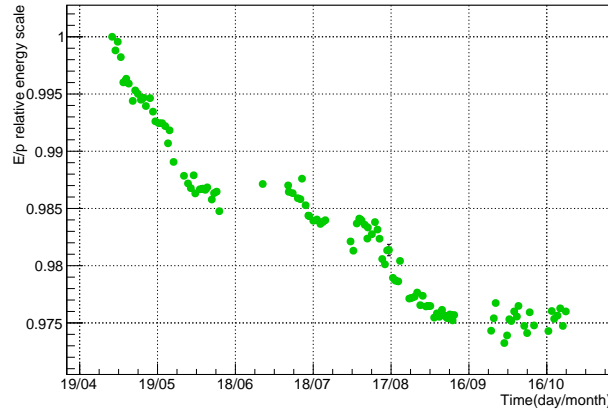


Figure 3.7: The E/p relative energy scale versus time for 2018 data-taking period after the application of the EFlow per-crystal corrections. The E/p value is computed as an average over all the EB crystals in the time interval. The inverse of these E/p values is used as an empirical correction to correct the global drift of the barrel. Every time interval has a duration of the order of one day.

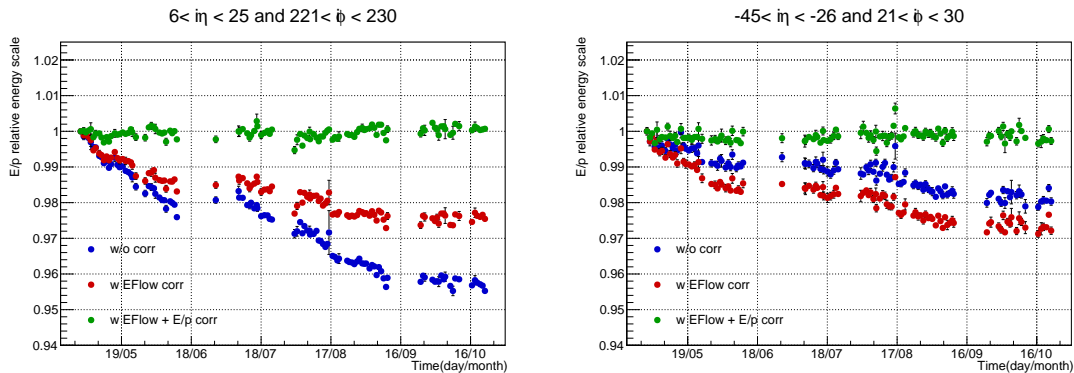


Figure 3.8: The E/p relative energy scale as a function of time for two harnesses in the 2018 data-taking period. Blue dots show the relative response of the harness before any correction is applied. Red dots are obtained from the blue ones by applying the EFlow corrections. Green dots represent the final result after local (EFlow) and global (E/p) intercalibrations are applied; the relative response of the two harnesses is restored to one, as expected.

cation of the global scale correction produces a shift toward 0 of the mean of the distribution (green histogram). In the right panel, the spread of the energy scale (measured with the E/p method) in each time interval is monitored. Before any correction (blue dots), the trend has a positive slope since the evolution of each harness is different. As expected, the application of the EFlow corrections flattens the RMS distribution versus time (red points) since it produces an equalization of the time evolution of crystals. The application of E/p corrections, which only affect the global scale, does not change the RMS (green points).

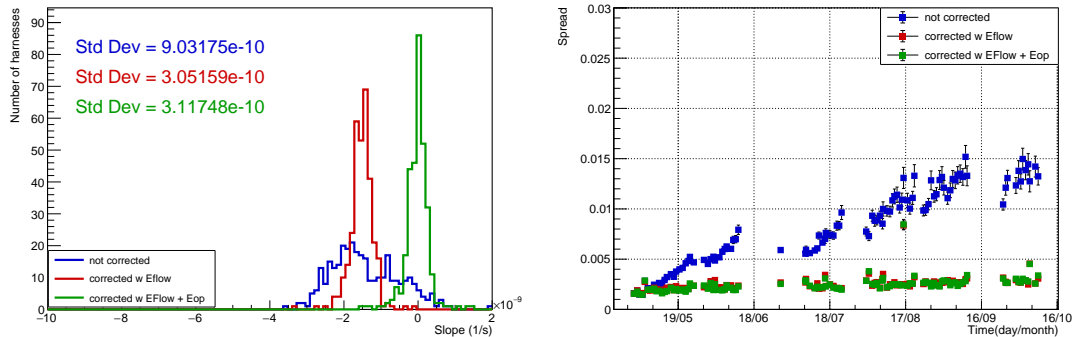


Figure 3.9: On the left panel, the histograms of the slopes of the harnesses' relative response versus time (monitored with E/p) before (blue solid line histogram) and after the corrections (red and green solid line histograms) are applied. Values of the RMS of these histograms are also reported. The slopes are obtained through a linear fit on the E/p scale as a function of time. On the right panel, the monitoring of the spread of the distribution of the E/p scale is reported for each harness. Blue dots are before any corrections. Red and green dots report the behavior after the EFlow and the EFlow + E/p corrections are applied, respectively.

3.3.3 Performance of regional drift corrections for Run III

As mentioned in Sec. 3.3.1, during Run II the drift due to PN aging was corrected offline, thanks to a per-harness linear fit of the energy-scale measured with the E/p template fit.

For Run III, two complementary methods can provide a prompt calibration. The first method relies on the E/p ratio but with some differences with respect to Run II. The observable monitored to measure the energy-scale is now the median of the E/p distribution, which is more stable than the one extracted with the template fit procedure. Moreover, corrections are derived with a two days granularity in time. The second method is the EFlow plus global scale correction (EFlow+E/p) described in Section 3.3.2.

To study the ECAL energy scale stability and resolution a sample of electrons from the $Z \rightarrow ee$ process is used. For this study, the energy of the electrons is reconstructed only from ECAL information (not using the tracker-related observables, as in the usual CMS reconstruction, described in Section 2.3.2).

The stability of the energy scale is estimated by the median value of the invariant mass distribution of electrons (m_{ee}) from Z boson decays, as reported in Figure 3.10. In the top right panel, the median of m_{ee} as a function of time is reported for the two calibration methods; in the right panel, the inclusive m_{ee} is shown over the whole year of data-taking. The stability achieved by the EFlow+E/p method is better than the one of the E/p alone by about 10%. After the time-dependent EFlow+E/p corrections, the energy scale remains stable within an RMS of 0.1 GeV (0.1%). The result is comparable with the one achieved by the calibration obtained after a careful analysis of all the Run II data set (Ultra Legacy).

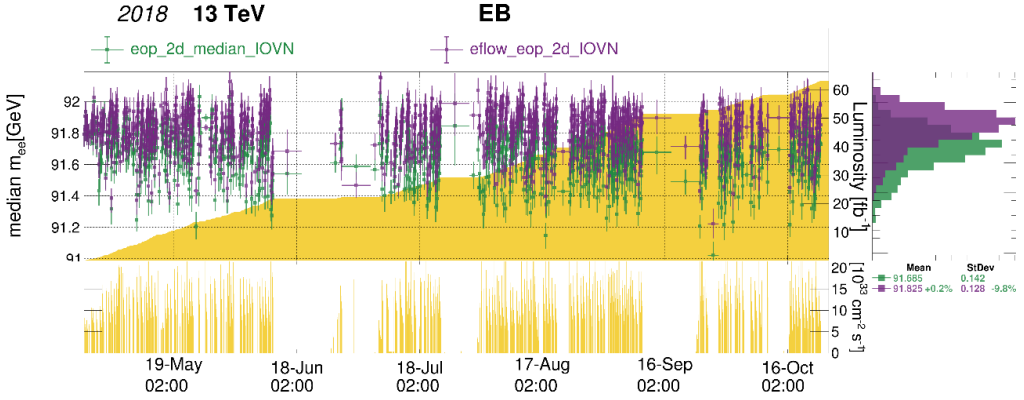


Figure 3.10: In the left panel, the median of m_{ee} as a function of time is reported for the EFlow+E/p (purple points) and the E/p calibration (green points) method. In the bottom left panel, the luminosity delivered by LHC is shown; the integrated one is shown (in the yellow histogram) in the upper left panel. In the right panel, the inclusive m_{ee} distribution is shown for the whole year of data-taking.

The electron energy resolution is estimated from a likelihood fit, performed with a Breit-Wigner convoluted with a Gaussian function, on the invariant mass distribution of m_{ee} . In the left panel of Figure 3.11, the relative resolution of the two methods in different η regions is reported. The Ultra Legacy calibration of Run II is used as a benchmark. Both the EFlow and E/p calibrations methods reach the same level of precision.

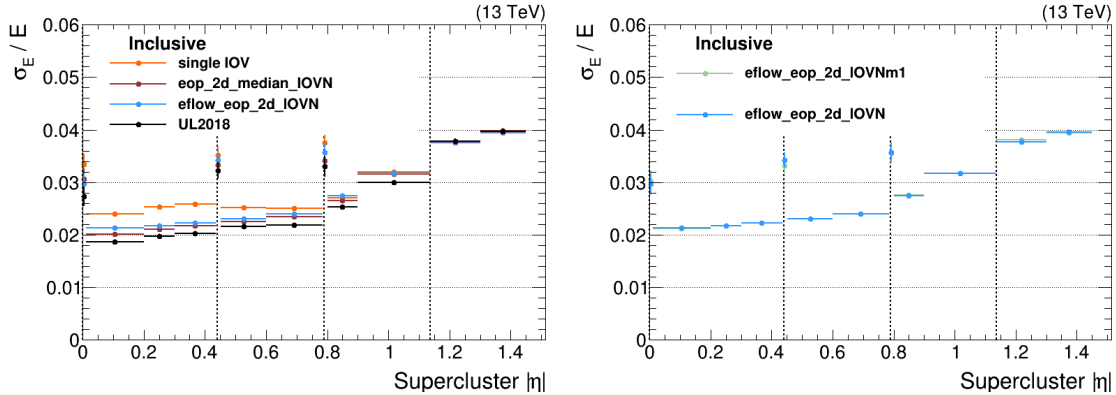


Figure 3.11: The relative resolution in the ECAL barrel calculated through the peak of $Z \rightarrow ee$ events for the 2018 data-taking period. Points at $\eta = 0, 0.45, 0.8, 1.15$ correspond to the inter-module boundaries of the ECAL barrel. On the left panel, the singleIOV (without PN corrections applied) is reported in orange; the Run II finest calibration (UL) is reported in black. Run III methods are compared to the Run II baseline (single IOV). The light blue points are obtained using the EFlow+E/p method with a time granularity of two days, while the purple ones are derived with the E/p corrections per-harness with a 2 fb^{-1} granularity. On the right panel, the relative energy resolution is reported for the IOV-Nm1 / IOV-N scenarios for the EFlow+E/p method with a two days time granularity.

Moreover, two possible schemes for the calibration methods have been tested. Events of a Run are split into time intervals (IOV) with a time granularity (order 1-2 days) needed to obtain the desired calibration precision. The scenario (IOV-Nm1) where data of an IOV N are corrected with intercalibrations derived in the IOV before (N-1) is preferred since this scenario does not need a delay in the processing of the data. The IOV-Nm1 scenario is compared with the one (IOV-N scenario) in which data in IOV N are corrected with intercalibrations derived from data of the same IOV. Results of these studies are reported in the right panel of Figure 3.11; both the calibration schemes produce the same electron relative energy resolution. Thus, the use of intercalibrations from the IOV N-1 to calibrate the data of IOV N does not spoil the resolution.

3.3.4 Summary and perspective for Run III

The details of a new method (EFlow) for deriving time-dependent intercalibrations have been shown. The method corrects the residual drift in the energy scale that is still visible after laser corrections. The EFlow method provides ICs with fine time and spatial granularities; indeed, corrections may be derived per every single crystal, using minimum bias data in a time interval of order one or two days.

The method, after the global scale corrections derived with electrons, produces results competitive with the standard E/p method used for Run II that provides per-harness corrections (order of 100 - 200 crystals) with a similar time granularity (cf. Sec. 3.3.3). In these preliminary results, the correction to the global scale has been performed with E/p. During the writing of this thesis, the implementation of the global scale correction through the median of the m_{ee} distribution is ongoing. The scope is to construct a calibration method (EFlow plus Zee for the global scale) that depends only on ECAL observable and is thus more stable; moreover, it is complementary to the E/p one. Indeed, the two calibration processes are supposed to be used to check on each other.

Finally, due to their time granularity, these calibrations will allow one to have a calibration of the new data collected by CMS during Run III, on a timescale that is compatible with the prompt reconstruction after the data-taking. The idea is to correct data taken in a time interval with the intercalibrations derived in the time interval before. It has been shown that this approach does not spoil the energy resolution. These methods are expected to avoid the effort of deriving all the corrections at the end of each year and reprocessing all the data using the final calibration.

4 Electroweak production of a pair of W^+W^- bosons in association with two jets

The following chapter reports the first observation at the LHC of the electroweak production of W^+W^- bosons in association with two jets in the fully leptonic final state. The analysis is performed on a data sample of 138 fb^{-1} , collected by the CMS experiment from 2016 to 2018 (full Run II data set) during the LHC proton-proton collisions at $\sqrt{s} = 13 \text{ TeV}$. The signal is observed with a statistical significance of 5.6 standard deviations. The measured fiducial cross section is $10.2 \pm 2.0 \text{ fb}$ in agreement with the standard model prediction.

The signal topology and the main backgrounds of the analysis are explained in Section 4.1. The data and the MC simulations used are reported in Section 4.2, while the reconstruction of the final state objects is described in Section 4.3. The selections applied on the events to define the several categories used in final fit are reported in Section 4.4. A deep neural network, described in Section 4.5, has been trained to cope with the very large $t\bar{t}$ contamination and the irreducible QCD-induced W^+W^- background. Control regions used to monitor the agreement between data and simulations are reported in Section 4.6. Methods used to estimate background contamination in the signal region are described in Section 4.7. The systematic uncertainties affecting the measurement are discussed in Section 4.8. Section 4.9 summarizes the statistical procedure used to extract the signal and the final results obtained. Eventually, Section 4.10 reports a summary of the obtained results and an outlook on the future developments of this work.

4.1 Signal topology and main backgrounds

In Section 1.2.1, it was shown that VBS processes are defined by the presence of two vector bosons in association with two high-energy and well-separated jets. Figure 4.1 shows a Feynman diagram of the signal; the gray circle includes all the possible interactions that may occur, as explained in Section 1.2.1. This analysis selects events in which the two W bosons decay leptonically in an electron or a muon plus the corresponding neutrino. Hence, the signal final state is characterized by two jets, two leptons of opposite charge, and an amount of missing transverse energy.

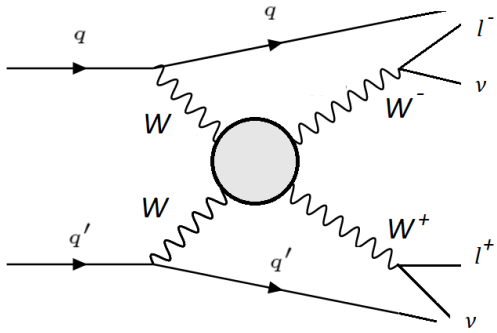


Figure 4.1: Schematic representation of the VBS W^+W^- process in the fully leptonic channel. The gray circle stands for all the possible interactions described in Sec. 1.2.1.

Events are then divided based on the flavor of final state leptons into three different categories: ee , $\mu\mu$, $e\mu$.

Some explicative Feynman diagrams for the main background processes, with a final state similar to the signal one, are reported in Figure 4.2. The main contribution to background arises from decays of top quarks from $t\bar{t}$ processes. A smaller contribution comes from single top (tW) production. Indeed, the top quark decays in a b quark and a W boson, which subsequently may decay leptonically, mimicking the VBS final state. However, the jets originating from b quarks (b jets), characterizing these processes, can be identified through sophisticated algorithms. Therefore, a veto against b jets is applied to suppress the contamination of $t\bar{t}$ - tW background in the signal region.

As explained in Sec. 1.2.1, the QCD-induced W^+W^- production shares the same final state of the signal, thus can only be reduced by requirements on the dijet invariant mass and separation in pseudorapidity of VBS jets.

The contamination from Drell-Yan (DY) processes ($pp \rightarrow Z/\gamma^* \rightarrow ll$) is due to detector effects: a fake high missing transverse energy is reconstructed together with the two leptons and jets from ISR. This background is large in the ee and $\mu\mu$ categories, while it is highly reduced in the $e\mu$ one. Indeed, in the $e\mu$ final state, the DY contribution only comes from the leptonic decays of tau leptons in $Z/\gamma^* \rightarrow \tau\tau \rightarrow ll$ processes.

Finally, another background contribution originates from the $W +$ jets production, where one lepton arises from the W boson decay, while the second (nonprompt lepton) derives from a reconstruction of a hadron, which is misidentified as a lepton. In the following, this background is referred to as nonprompt background.

The Higgs boson production and the multiboson processes, including diboson (ZZ , $WZ/\gamma^{(*)}$, $Z\gamma$) and triboson (WWW , ZZZ , WWZ , WZZ) productions, are considered in the analysis as well. However, they constitute only minor contributions to the total background since they are highly reduced by the requirements on the VBS jets and the leptons, as will be explained in Sec. 4.4.

In Section 4.7, the methods used in this analysis to estimate the contributions

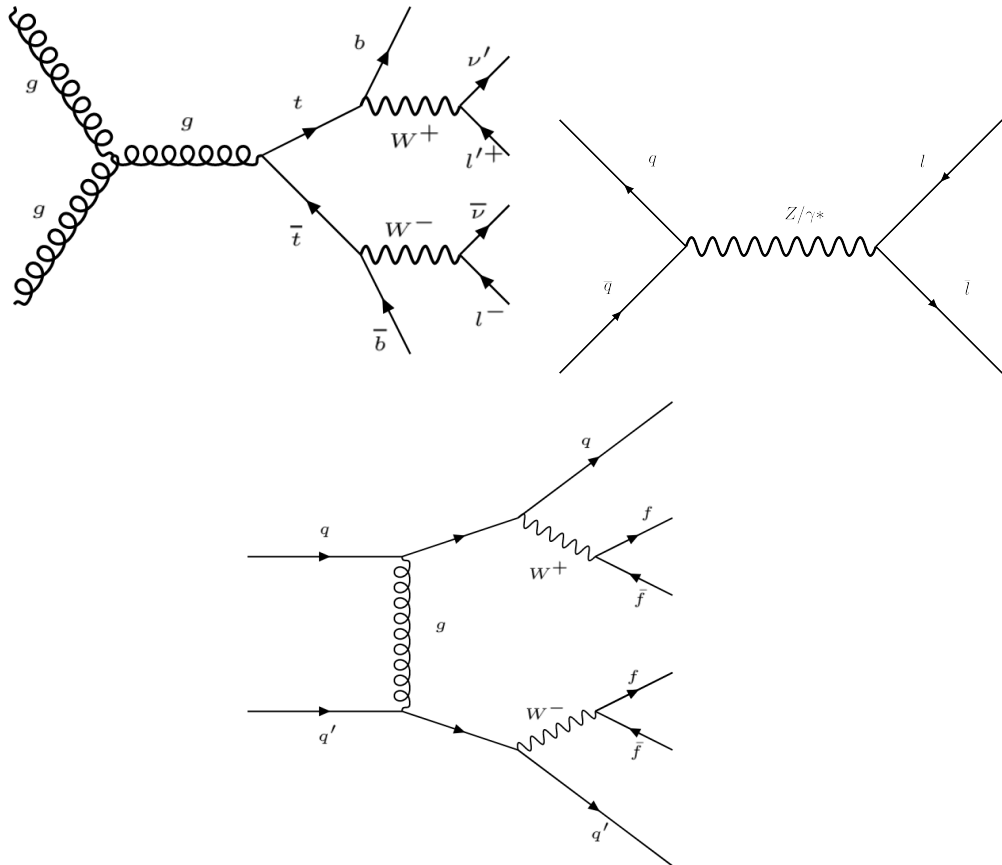


Figure 4.2: Feynman diagrams representative of the backgrounds affecting the analysis. Top left: our main background from $t\bar{t}$ production. Top right: DY process, mostly affecting final state with leptons of the same flavor. Bottom central: the irreducible QCD background described in Sec. 1.2.1.

from all the different sources of background in the signal region are explained. In particular, data-driven techniques are used to achieve better modeling of the main background processes such as $t\bar{t}$ - tW , DY, QCD-induced W^+W^- , and nonprompt; whereas, the estimation of minor background is entirely based on Monte Carlo simulations.

4.2 Data set, triggers and simulated samples

The data sets correspond to the 2016, 2017, and 2018 data-taking periods, with integrated luminosities of 36.3 fb^{-1} , 41.5 fb^{-1} , and 59.7 fb^{-1} , respectively [50, 51, 52].

4.2.1 Triggers

The analysis selects events with two leptons (electrons or muons) in the final state. Hence, a combination of both single and double lepton HLT triggers filters candidate events. The single lepton triggers require the presence of one high- p_T lepton, whereas the double lepton ones ask for two leptons with a lower p_T threshold. In both cases, leptons have to pass identification and isolation criteria. Trigger requirements are always less stringent than those used in the off-line analysis (cf. Sec 4.4). The triggers used in the analysis with their p_T -thresholds for all the three years are reported in Table 4.1.

Table 4.1: p_T requirements of HLT triggers used in the analysis.

Single lepton triggers		
One muon	2016	$p_T > 23 \text{ GeV}$ in $ \eta < 2.4$
	2017	$p_T > 27 \text{ GeV}$ in $ \eta < 2.4$
	2018	$p_T > 24 \text{ GeV}$ in $ \eta < 2.4$
One electron	2016	$p_T > 25$ (27) GeV in $ \eta < 2.1$ ($2.1 < \eta < 2.5$)
	2017	$p_T > 35 \text{ GeV}$ in $ \eta < 2.5$
	2018	$p_T > 32 \text{ GeV}$ in $ \eta < 2.5$
Dilepton triggers		
Two muons	2016-2018	Leading $p_T > 17 \text{ GeV}$ & trailing $p_T > 8 \text{ GeV}$
Two electrons	2016-2018	Leading $p_T > 17 \text{ GeV}$ & trailing $p_T > 8 \text{ GeV}$
One muon and one electron	2016 begin	Leading $p_T > 23 \text{ GeV}$ & trailing $p_T > 8 \text{ GeV}$
	2016 end - 2018	Leading $p_T > 23 \text{ GeV}$ & trailing $p_T > 12 \text{ GeV}$

4.2.2 Simulated samples

The analysis uses several Monte Carlo (MC) generators to simulate the signal and background processes. Different simulations are generated for each of 2016, 2017, and 2018 data set to account for changes in the detector conditions, different pileup conditions, and updates of the reconstruction software. The samples are generated using either POWHEG v2 [53], MADGRAPH5_aMC@NLO (v2.4.2) [54], or MCFM (v7.0) [55, 56, 57], depending on the particular hard scattering process. The simulations reach an accuracy up to next-to-LO (NLO) in QCD for most of the samples. The PYTHIA 8.226 (8.230) generator is interfaced to the hard scattering generators to simulate parton-shower and hadronization processes with the CUETP8M1 [58] CP5 [59]) underlying events (UE) tune in 2016 (2017 and 2018). The set of parton distribution functions (PDFs) is NNPDF 3.0 [60, 61] (3.1 [62]) for 2016 sample (2017-2018 samples). Eventually, the interaction of the particles with the CMS detector is simulated through the GEANT4 package [63] for all the processes.

Moreover, to achieve a more accurate description of the collision data, simulated events are multiplied by weights; these weights are obtained from data as functions of relevant lepton or jet kinematic observables. Indeed, events in MC samples are not filtered by any trigger but are multiplied by weights to emulate trigger efficiency. Trigger weights are derived from data and applied as a function of the p_T and η of the lepton candidate. For each year, a reweighting factor, as a function of the true number of generated inelastic collisions in the event, is applied to reproduce the actual pileup profile in data. This factor is obtained for each year as the ratio between the normalized distributions of the number of inelastic collisions and the Monte Carlo pileup profile. Additional corrections are applied to account for efficiencies in the reconstruction, identification, and isolation of electrons and muons. The “tag-and-probe” technique [64] is used to estimate all these weights as a function of the lepton p_T and η from events with leptonic Z boson decay. The b quark tagging efficiency is measured through data samples enriched in b jets; the weights, depending on the jet p_T , η , flavor, and the b tagging discriminator value, are applied to MC events. In addition, the p_T distribution of $t\bar{t}$ process and the p_T distribution of the Z boson in DY samples are multiplied by specific weights to improve the agreement of these simulations with data.

The VBS electroweak process, with two quarks and two leptonically-decaying W bosons in the final state, is simulated at leading order (LO) through MADGRAPH5_aMC@NLO. The generator is interfaced with PYTHIA 8 [65] using the so-called dipole recoil scheme; a discussion on the parton shower setting for the signal modeling is reported in the next Section 4.2.3. Diagrams containing contributions from top quarks are subtracted. On-shell Higgs boson production mechanisms are considered background sources and simulated with POWHEG v2 at NLO accuracy in QCD, with the gluon-gluon fusion (ggF) production mode further reweighted to match next-to-NLO (NNLO) accuracy in the NNLOPS scheme [66]. The QCD-induced W^+W^- background is generated at the NNLO accuracy in QCD for the inclusive process through POWHEG v2, with the second jet simulated at LO accuracy [67]. The interference term between the purely EW signal and the QCD-

induced background is of the order of a few percent with respect to the signal yield; its negligible contribution has not been taken into account in the analysis.

In Table 4.2, a list of the different processes simulated and of the MC generators used to produce them is given.

Table 4.2: Signal and background processes simulated with MC generators. If not specified, the generators are the same for all the three years and have NLO accuracy in QCD. The PYTHIA 8 generator is used for parton shower and hadronization simulation.

Signal	Generator
VBS $W^+W^- jj \rightarrow 2l2\nu$ no top quarks	MADGRAPH5_aMC@NLO (LO)
Background	Generator
$t\bar{t}$, tW	POWHEG v2
$DY \rightarrow ll + jets$	MADGRAPH5_aMC@NLO (LO)
$DY \rightarrow \tau\tau \rightarrow ll + jets$	MADGRAPH5_aMC@NLO
Gluon fusion W^+W^-	MCFM v7.0
QCD-induced W^+W^-	POWHEG v2 (NNLO)
$Z + 2$ jets EW	MADGRAPH5_aMC@NLO
$W \gamma$	MADGRAPH5_aMC@NLO (LO)
$Z \gamma$	MADGRAPH5_aMC@NLO
$W Z/\gamma^*$	POWHEG v2
$W Z \rightarrow 2l2q$	MADGRAPH5_aMC@NLO
$Z Z \rightarrow 2l2q, 2l2\nu, 4l$	POWHEG v2
$Z Z \rightarrow 2l2q$ (2017/2018)	MADGRAPH5_aMC@NLO
$Z Z Z, W Z Z, W W Z, W W W$	MADGRAPH5_aMC@NLO
Higgs boson production: gluon fusion, VBF ...	POWHEG v2

4.2.3 Signal modeling

Some studies on MADGRAPH5_aMC@NLO samples have been performed to compare different parton shower algorithms and to evaluate their impact on the analysis. In particular, the standard PYTHIA 8 shower using a “global” recoil scheme is compared to the one implementing a “local” recoil scheme (dipole recoil). In the global recoil scheme, any particle involved in the scattering may absorb the recoil of the parton splittings. However, the color flow in VBS diagrams occurs only between an initial-state quark and a final-state quark [68]; hence, a more natural description of the process is provided by the dipole recoil scheme.

Figure 4.3 shows some variables of interest for signal samples generated with the two different parton shower settings. Observables most affected are the ones related to the third jet; indeed, the dipole recoil scheme mitigates the third jet production activity. Therefore, only small differences arise in inclusive variables (such as m_{jj} and $\Delta\eta_{jj}$). As will be explained in the following sections, this analysis does not exploit observables related to the third jet. Hence, the impact of the parton shower setting on the analysis is not dramatic.

The comparison between the global and dipole recoil samples has been drawn with selections similar to the signal region one, explained in Table 4.3 of Section 4.4. All the final state flavor categories are merged, applying no event categorization in the Zeppenfeld variable [69] and requiring $m_{\ell\ell} > 50$ GeV and $p_T^{\text{miss}} > 20$ GeV.

The 2017 and 2018 signal samples are generated through MADGRAPH5_aMC@NLO (v.2.4.2), while the 2016 one uses MADGRAPH5_aMC@NLO (v.2.6.5). The cross section is 0.09283 ± 0.00016 pb for the samples produced with MADGRAPH5_aMC@NLO (v.2.4.2) and 0.09217 ± 0.00020 pb for the samples produced with MADGRAPH5_aMC@NLO (v.2.6.5). Finally, since the dipole recoil scheme is expected to provide a better description, it has been used to produce the signal samples employed in this analysis.

4.3 Physical objects identification

The CMS particle-flow algorithm (PF) [36], described in Section 2.3, elaborates the information provided by the various CMS subdetectors to reconstruct kinematic observables and identify the related particles. In the following, the different final state objects used in this analysis are described, along with the requirements that they have to satisfy.

4.3.1 Electrons

The reconstruction of electrons is obtained by connecting tracks in the silicon tracker to energy deposits in ECAL. Electron candidate are required to be within the tracker acceptance ($|\eta| < 2.5$). In prompt electrons identification [39], background sources arise from photon conversions, semileptonic decays of b and c quarks, or jets with a large electromagnetic component, which can be reconstructed as electrons. Several observables are used to distinguish prompt electrons from the background processes. Calorimetric observables, such as the dimension of the ECAL shower or the ratio between ECAL and HCAL energy deposits, are employed to reject the contamination of jets. Indeed, a hadron shower is usually larger and deeper than an electromagnetic one. Exploiting information from the reconstructed tracks helps to distinguish electrons from charged hadrons. Eventually, variables comparing the momentum measured in the tracker with the energy measured by ECAL and observables evaluating the compatibility between the track and the ECAL supercluster's position are used.

The relative isolation variable is defined as the p_T sum of all the PF candidates (subtracting the pileup contribution) in a cone of $R=0.3$ around the electron candidate, normalized to the electron p_T

$$ISO_{\text{rel}} = \frac{\sum p_T^{\text{charged}} + \max(0, \sum p_T^{\text{neutral}} + \sum p_T^\gamma - \frac{1}{2} \cdot \sum p_T^{\text{PU}})}{p_T} \quad (4.1)$$

where $\sum p_T^{\text{charged}}$, $\sum p_T^{\text{neutral}}$, $\sum p_T^\gamma$ are the p_T sums of charged hadrons from primary vertex and neutral particles (hadrons and γ) within the isolation cone, while $\frac{1}{2} \cdot \sum p_T^{\text{PU}}$

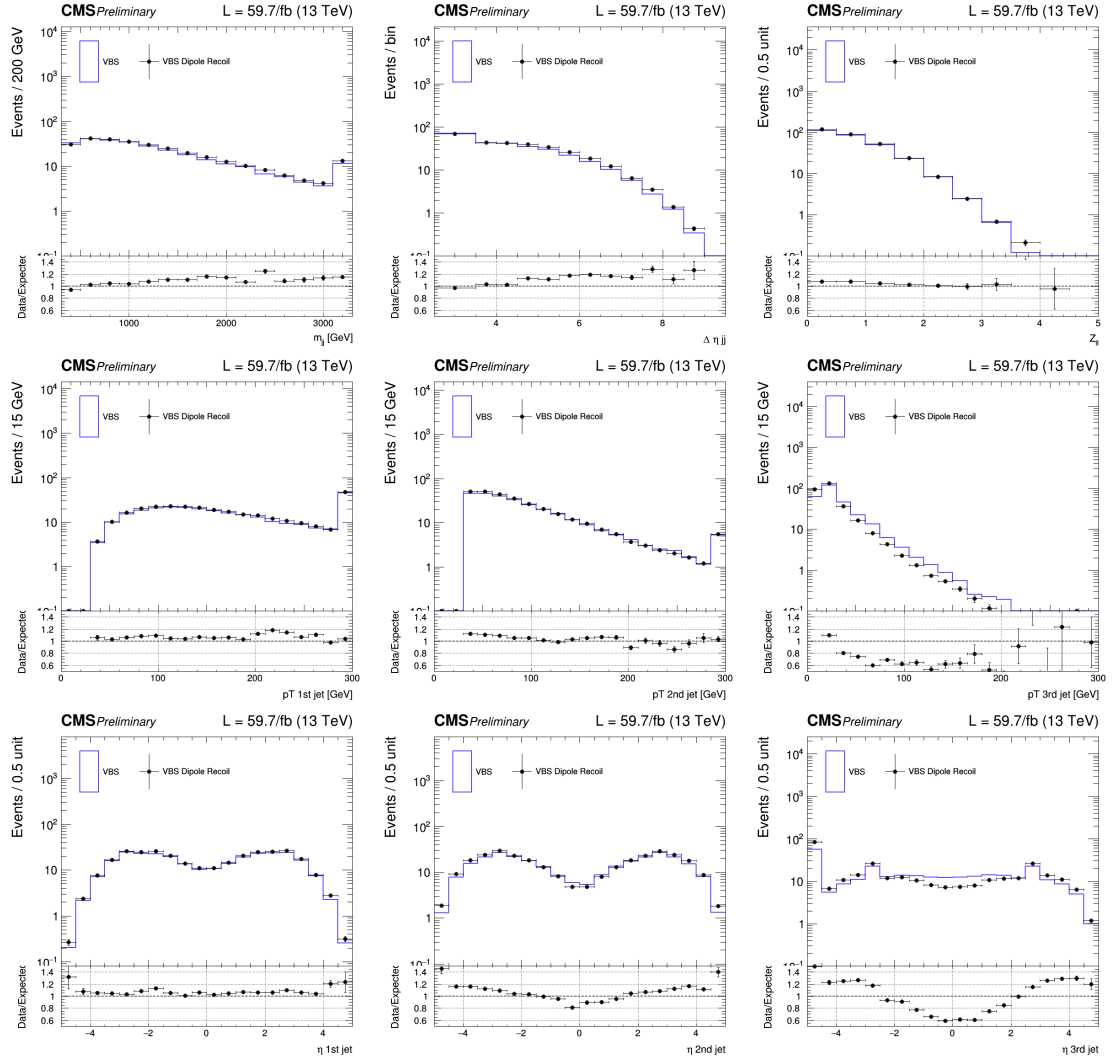


Figure 4.3: Comparison between different parton shower algorithms applied to 2018 MADGRAPH5_aMC@NLO signal samples; first row: dijet mass of the two tagging jets, pseudorapidity gap of the two tagging jets and $Z_{\ell\ell}$ (Equation 4.2) [69]; second row: p_T of the first, second, and third jet, respectively; third row: η of the first, second, and third jet, respectively. The second panel in each plot shows the ratio between dipole recoil and global recoil signal samples. Underflow events and overflow events are folded in the first and last bin, respectively. The peak in the first bin of the third jet η is due to events without a third jet.

is an estimate of the contribution of neutral hadrons from pileup vertices, which is correctly subtracted.

A single discriminator variable exploiting a multivariate technique is trained to improve the separation between prompt electrons and backgrounds. The Boosted Decision Tree (BDT) algorithms are fed with the observables mentioned above (including the isolation) to condense all the relevant pieces of information into a single

discriminator output [39]. Selecting different thresholds of the discriminator output (working points) provides different percentages of signal efficiency and background rejection. The working point used in this analysis ensures 90% of signal efficiency. Moreover, a tight cut on the relative isolation of the electron candidate (required to be $< 6\%$) is applied to avoid confusion with jets or real electrons, from semileptonic decays of b or c quarks, within a jet.

4.3.2 Muons

Muons are reconstructed from tracks in the inner tracker and the outer muon system, as explained in Section 2.3.1. A muon candidate is required to have a $p_T > 10$ GeV, to be in the region $|\eta| < 2.4$ and pass the tight selection described in Ref. [37]. Tight muons are those reconstructed as tracker muons and global muons by the PF algorithm. Requirements on the number of hits in the tracks (at least six in the tracker layers, one in the pixel detector, and two in the muon system) are applied; the χ^2/dof of the track fit should be less than 10. Moreover, requirements on the muon’s impact parameters with respect to the primary vertex are imposed to avoid contamination from muons originating from a secondary vertex. On the transverse plane, the tight muon must have an impact parameter $|d_{xy}| < 0.2$ cm, while on the longitudinal direction it must have $|d_z| < 0.5$ cm. In this analysis, stricter conditions are applied on the impact parameters, to further reduce background contamination: $|d_{xy}| < 0.01$ cm for $p_T < 20$ GeV or $|d_{xy}| < 0.02$ cm for $p_T > 20$ GeV and $|d_z| < 0.1$ cm. The relative isolation is defined for muon as well, similarly to the one used for electrons (Equation 4.1), but in a cone of $R=0.4$ centered in the muon direction. A condition on the relative isolation to be less than 15% is applied to exclude real muons within jets and jets misidentified as muons. Eventually, the MVA discriminator developed for the ttH analysis [70] is used. A cut on its output (> 0.8) is applied on top of all the selections described above.

4.3.3 Jets

Jets are made by several particles, originating from the hadronization process. In this analysis, jets are reconstructed starting from particle flow candidates through the anti- k_T algorithm [41, 42] with a distance parameter of $R=0.4$, which guarantees robustness against collinear and soft divergences. Charged particles from non-primary vertices are removed before the clustering through the Charged Hadron Subtraction (CHS) method. In the analysis, jets have to be within $|\eta| < 4.7$ and must have a $p_T > 30$ GeV. To correct for possible discrepancies between data and MC events, jet energy corrections (JEC) are applied. Jet energy resolution (JER) scale factors are used to smear the jet transverse momentum only in 2017 and 2018 MC events since in 2016 they led to a worsening of data-MC agreement. In the reconstruction of a jet, background sources arise either from electronic noise in the calorimeters (noise jets) or from particles originating from non-primary vertices (pileup jets). Identification criteria are defined to separate the physical jets from

noise jets using jet-related observables, such as the hadronic (charged and neutral) and electromagnetic energy fractions of the jet and the multiplicity of PF candidates within the jet. All the jets in the analysis with $p_T > 30$ GeV have to pass the tight working point of the jet identification, as defined in [71]. A BDT that uses jet-shape and tracking observables has been trained to discriminate and exclude pileup jets. In the analysis, jets with $p_T < 50$ GeV are required to pass the loose working point of this pileup jet ID [71] to suppress contribution from pileup interactions. Selected jets are also required to not overlap with leptons within a ΔR of 0.4.

4.3.4 B tagged jets

The b tagging refers to all the different reconstruction techniques used to identify b jets in an event; it is a fundamental tool to reject $t\bar{t}$ -tW background events. The various b tagging algorithms exploit track information, secondary vertex information, soft lepton information, or some combination of the above to produce an output discriminator, which describes how likely a jet derives from a b quark. Three values of the discriminator, i.e. working points, are recommended: loose, medium, and tight. The three correspond to different b tagging efficiencies and have misidentification probabilities for light-flavor jets of around 10%, 1%, and 0.1%, respectively. In this analysis, jets are defined as b jets if they are above the loose working point of the DeepJet algorithm [72, 73], which is an algorithm based on a neural network. The discriminator values corresponding to the loose working point are 0.0614, 0.0521, and 0.0494 for 2016, 2017, and 2018, respectively.

4.3.5 Missing transverse momentum

The missing transverse momentum vector is computed as the negative vector sum of the transverse momenta of all the PF particles reconstructed in the event; its magnitude is known as p_T^{miss} [44]. The Pileup Per Particle Identification (PUPPI) [74] is employed to reduce the contribution to the p_T^{miss} of particles deriving from pileup vertices. Indeed, the PUPPI algorithm computes the p_T^{miss} , weighting each PF candidate by the probability to derive from the primary interaction vertex. In this way, a better resolution and a better agreement between the data and the simulation are achieved. Moreover, jet energy corrections are propagated to the PUPPI p_T^{miss} to improve further the resolution.

4.4 Selections

A set of basic selections (referred to as preselections) are applied to identify events with a VBS-like signature. Events containing two leptons (electrons or muons) with opposite sign charges, at least two jets, and a certain amount of missing transverse energy are selected. The p_T thresholds for the leading and trailing leptons are set to 25 GeV and 13 GeV, respectively; any event with an additional loosely identified lepton with $p_T > 10$ GeV is rejected to suppress contamination from multiboson

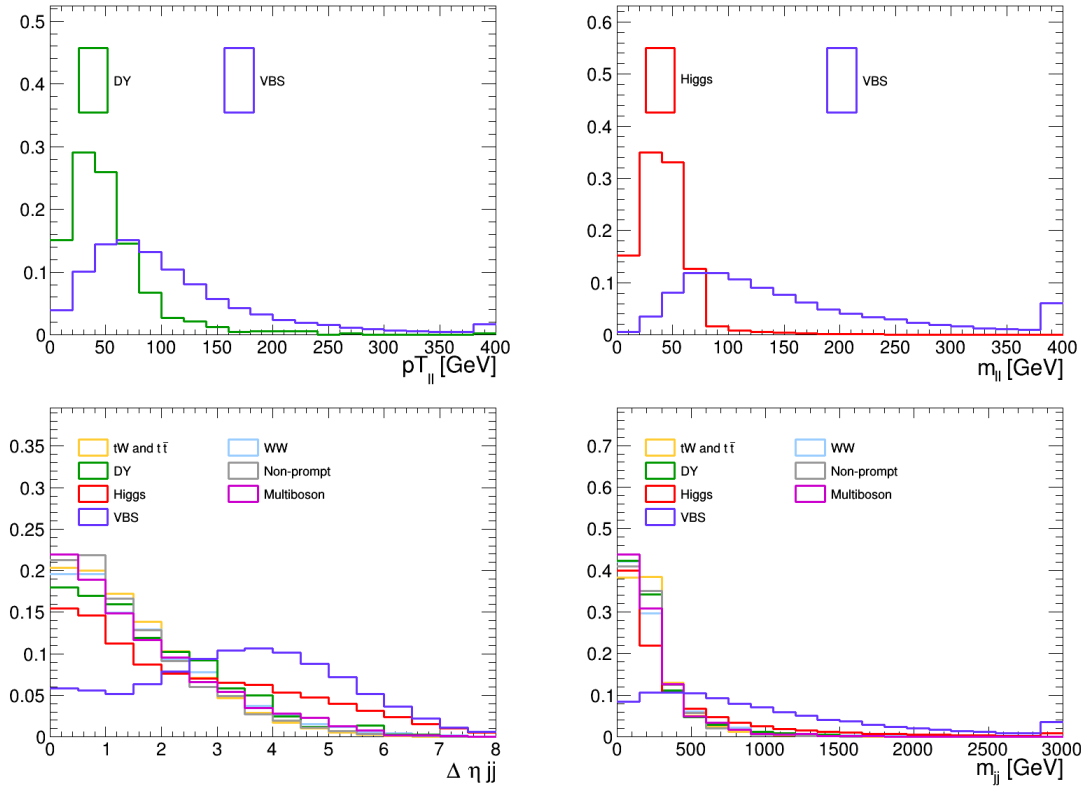


Figure 4.4: Normalized distributions of the VBS signal (violet line) and the backgrounds (multicolored lines) in some of the discriminating observables. The plots refer to the 2018 data sample in the $e\mu$ final state.

interactions. The event is selected if at least two jets with $p_T > 30$ GeV are present; the two jets with the highest- p_T are tagged as the VBS jets. Moreover, a threshold on the p_T^{miss} is set to 20 GeV to account for the presence of neutrinos.

In Figure 4.4, the normalized distribution of the signal and the various backgrounds components are reported for some discriminating observables; all the cuts mentioned above are applied. Further selections on these variables are needed to suppress background contamination. The dilepton invariant mass $m_{\ell\ell}$ is required to be greater than 50 GeV to minimize the contamination from $H \rightarrow WW$; the dilepton transverse momentum $p_T^{\ell\ell}$ is required to be above 30 GeV to reduce the presence of leptons from DY production. The invariant mass of the VBS jets (m_{jj}) is required to be greater than 300 GeV; their pseudorapidity gap ($\Delta\eta_{jj}$) must be at least 2.5. The selections on these last two observables reduce the contamination from all the background sources, defining a VBS-like phase space. All the preselections are summarized in Table 4.3.

On top of preselections, further requirements are applied to obtain the optimal signal-to-background ratio in the signal region, as detailed in the following. Moreover, two control regions are defined to study the agreement between data and simulation; they are also employed to constrain the normalization of the top quark processes and DY production. Control regions are enriched in one of these two

Table 4.3: Preselections applied to all events to define a loose VBS-like phase space.

Observable	Selection
Leptons' pairs	e^+e^- , $\mu^+\mu^-$, $e^+\mu^-$, $e^-\mu^+$
p_T of leading (trailing) lepton	$p_T^{\ell_1} > 25$ ($p_T^{\ell_2} > 13$) GeV
Invariant mass of leptons' pair	$m_{\ell\ell} > 50$ GeV
p_T of leptons' pair	$p_T^{\ell\ell} > 30$ GeV
p_T of additional leptons	$p_T^{\ell_3} < 10$ GeV
p_T of VBS jets	$p_T^j > 30$ GeV
Dijet invariant mass	$m_{jj} > 300$ GeV
Pseudorapidity gap	$\Delta\eta_{jj} > 2.5$
Missing transverse momentum	$p_T^{\text{miss}} > 20$ GeV

backgrounds through selections that make them orthogonal to the signal region. Each region is further categorized based on the lepton flavor: two electrons (ee), two muons ($\mu\mu$), or one electron and one muon ($e\mu$).

The signal region is defined by excluding the presence of b jets (b veto) to reduce the contamination from $t\bar{t}$ -tW events. In the $e\mu$ category, the transverse mass formed by the combination of $p_T^{\ell\ell}$ and p_T^{miss} (m_T) is required to be above 60 GeV. In ee and $\mu\mu$ categories, no selection is applied to m_T , but more stringent cuts on p_T^{miss} and $m_{\ell\ell}$ are required to suppress the contamination from DY events. Hence, the p_T^{miss} threshold is raised to 60 GeV and $m_{\ell\ell}$ is set to be greater than 120 GeV to discard events from Z boson production.

The signal region is further divided into two subregions to maximize the signal significance. The categorization is based on the dilepton Zeppenfeld variable [69]

$$Z_{\ell\ell} = \frac{1}{2}|Z_{\ell_1} + Z_{\ell_2}|, \quad (4.2)$$

where $Z_\ell = \eta_\ell - \frac{1}{2}(\eta_{j_1} + \eta_{j_2})$,

that measures the centrality of the dilepton system with respect to the tagging jets. Since the decay products of the W^+W^- bosons are expected to be in the inner space between the two VBS jets, categories with $Z_{\ell\ell} < 1$ are enriched in signal events and benefit of less background contamination (Figure 4.5).

The $t\bar{t}$ -tW control regions are defined similarly to signal ones but inverting the b veto, thus requiring the presence of at least a b jet with $p_T > 20$ GeV in the final state. The fraction of $t\bar{t}$ -tW processes in their control regions reaches $\sim 95\%$.

In DY control regions, the b veto is applied (as in the signal region) to keep this phase space orthogonal to the $t\bar{t}$ -tW control region. Different selections are then applied for $e\mu$ and $ee/\mu\mu$ final states to ensure the orthogonality with the corresponding signal regions. In the DY $e\mu$ category, the m_T cut is reversed with respect to the $e\mu$ signal region and a 50 GeV $< m_{\ell\ell} < 80$ GeV window is selected; in

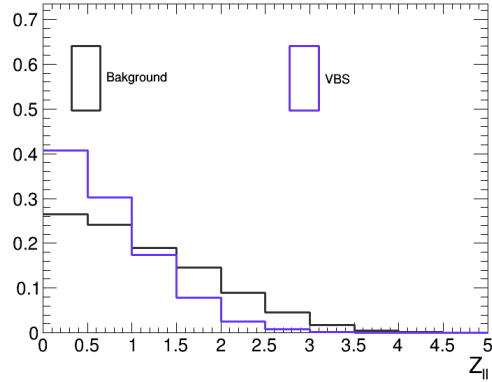


Figure 4.5: Normalized distributions of the VBS signal (violet line) and the backgrounds (black line) in the $Z_{\ell\ell}$ variable (as defined in Equation 4.2). The plots refer to the 2018 data sample in the $e\mu$ final state.

DY ee and $\mu\mu$ categories, $m_{\ell\ell}$ is restricted to a region near the Z boson mass peak ($|m_{\ell\ell} - m_Z| < 15$ GeV). Moreover, in the ee and $\mu\mu$ final state, the DY control region is further split into two $\Delta\eta_{jj}$ bins, one of each enriched in a different component of the DY background, as explained in Section 4.7. The fraction of DY events in the $e\mu$ DY control regions is $\sim 64\%$, whereas it reaches $\sim 91\%$ in the ee - $\mu\mu$ ones.

Table 4.4 summarizes all the different categories used in the analysis and the selections applied to define them.

Table 4.4: Summary of the selections defining all the signal and control regions of the analysis. These selections are applied on top of the preselections of Table 4.3.

VBS	$e\mu/\mu e$	$Z_{\ell\ell} < 1$	$m_T > 60 \text{ GeV}$ $m_{\ell\ell} > 50 \text{ GeV}$ no bjet with $p_T > 20 \text{ GeV}$
		$Z_{\ell\ell} \geq 1$	
	ee	$Z_{\ell\ell} < 1$	
		$Z_{\ell\ell} \geq 1$	$m_{\ell\ell} > 120 \text{ GeV}$ $p_T^{\text{miss}} > 60 \text{ GeV}$
$t\bar{t}\text{-tW}$	$e\mu/\mu e$	$Z_{\ell\ell} < 1$	
		$Z_{\ell\ell} \geq 1$	no b jet with $p_T > 20 \text{ GeV}$
	ee	$Z_{\ell\ell} < 1$	
		$Z_{\ell\ell} \geq 1$	$m_{\ell\ell} > 50 \text{ GeV}$ at least one b jet with $p_T > 20 \text{ GeV}$
DY	$e\mu/\mu e$	ee	$m_{\ell\ell} > 120 \text{ GeV}$ $p_T^{\text{miss}} > 60 \text{ GeV}$ at least one b jet with $p_T > 20 \text{ GeV}$
		$\mu\mu$	
	$e\mu/\mu e$	$\mu\mu$	$m_T < 60 \text{ GeV}$ $50 \text{ GeV} < m_{\ell\ell} < 80 \text{ GeV}$ no b jet with $p_T > 20 \text{ GeV}$
		ee	$\Delta\eta_{jj} < 5$ $\Delta\eta_{jj} \geq 5$
		$\mu\mu$	$ \Delta\eta_{jj} < 5$ $ \Delta\eta_{jj} \geq 5$
			$ m_{\ell\ell} - m_Z < 15 \text{ GeV}$ $p_T^{\text{miss}} > 60 \text{ GeV}$ no b jet with $p_T > 20 \text{ GeV}$

4.5 Deep neural network for the $e\mu$ category

In the $e\mu$ signal region, a feed-forward deep neural network (DNN) is used as a discriminator to separate signal events from the background. The task consists in classifying events into only two categories (binary classification): the signal (1) or the background (0). Thus, the output of the network (DNN output) is a floating point number in this range [0, 1]. The DNN is trained to recognize the VBS signal against the two main backgrounds: the $t\bar{t}$ process and QCD-induced W^+W^- production. Two different models are built and trained in the $e\mu$ signal region (as defined in section 4.4), one optimized for the $Z_{\ell\ell} < 1$ and the other for the $Z_{\ell\ell} \geq 1$ phase space. The two models share the same architecture and receive as input the same nine discriminating variables, wisely chosen among a larger number of observables. In the following, the concept of DNN (Section 4.5.1) is briefly introduced; the details of the two models used in the analysis are described in Sections 4.5.2-4.5.6.

4.5.1 Deep neural networks

Neural networks are made of computing units called nodes (or neurons). A node is a basic unit that performs a weighted linear combination of the N inputs (x_i) received and produces, following an activation function (ϕ), a single output ($y_j(\vec{x})$)

$$y_j(\vec{x}) = \phi\left(\sum_{i=1}^N w_{ij}x_i + b_j\right), \quad (4.3)$$

where w_{ij} are the weights given to each input and b_j is the bias.

Nodes can be organized in different patterns, depending on the particular task of the network. For the binary classification task, the typical architecture chosen is the feed-forward neural network, in which nodes are organized in layers with a hierarchical structure. In this way, the inputs flow from the input layer through hidden layers to the output layer. When the hidden layers are more than one, the neural network becomes “deep”.

The number of hidden layers and their number of nodes are tunable parameters of a network among the so-called hyper-parameters. The hyper-parameters of a network are all those parameters that can be adjusted before the training starts and remain fixed during it. Contrarily, the weights and the biases of each node are optimized by supervised learning. In supervised learning, the network receives input events from both the signal and background samples, together with their correct labels. Thus, the network prediction for the inputs is compared with the correct answer to estimate the error, which is quantified through the loss function. The usual choice for a binary classification task is the binary cross-entropy loss function, defined as follow

$$L = -\frac{1}{N} \sum_{i=1}^N [y_i \log(y(\vec{x}_i)) + (1 - y_i) \log(1 - y(\vec{x}_i))], \quad (4.4)$$

where y_i are the labels and $y(\vec{x}_i)$ are the predictions of the network.

The objective of the training in supervised learning consists in minimizing the loss function to obtain the optimal configuration of the network and thus a prediction as close as possible to the desired one. To obtain this, after the forward propagation of the input layer by layer, a backward propagation is needed. During this step, the flow goes from the output layer to the input one and the parameters are updated according to

$$\theta_{ij} \rightarrow \theta_{ij} - lr \cdot \frac{\partial L}{\partial \theta_{ij}} \quad (4.5)$$

where L is the loss function and lr is the learning rate, an hyper-parameter that controls the step-size of the updates.

Each iteration of the network, consisting of a forward and a backward propagation through all the data set, is called an epoch. The data set is usually divided into batches, containing only a limited number of the training events. The number of events of each batch is set through the batch-size hyper-parameter.

4.5.2 Preparation of samples

In the training process, simulated events for the signal and background ($t\bar{t}$ and QCD-induced W^+W^- production) are employed; they are reported in Tables 4.5. These training samples differ from the ones used in the analysis (cf. Section 4.2.2), as this helps guarantee the reliability of the models.

A large training data set makes it possible to build larger regularized models and to prevent overtraining since, with more examples, the DNN improves its ability to generalize. Thus, samples from 2016, 2017, and 2018 are weighted according to their integrated luminosity and merged to enlarge the training data set. Eventually, one network only is built for all three years in both $Z_{\ell\ell} < 1$ and $Z_{\ell\ell} \geq 1$ models.

The training sample is divided into a training data set (80%) and a validation data set (20%). The training data set is used by the DNN during its learning process, while the validation one is employed to monitor the training process. The validation sample contains events not shown to the network during the training to test the predictivity of the models and reject overtrained ones.

During the training, each sample is weighted according to its cross section and the integrated luminosity. Moreover, all the corrections explained in Section 4.2.2 are considered. The weights are considered in the computation of the loss, so that the back-propagation will give more importance to the events with higher weights.

However, background events ($t\bar{t}$, QCD-induced W^+W^-) acquire more importance than signal ones after this reweighting, because of their higher cross sections. If not treated carefully, this large difference in the number of weighted events of the two categories may lead to biased training. Indeed, the network would be more attentive to not misclassify background events than signal ones. Therefore, the number of weighted events of the signal and background data set are equalized (balancing)

to avoid biases by multiplying each event with

$$\frac{w_i}{\sum_i w_i} \cdot nS, \quad (4.6)$$

where w_i are the weights of each event accounting for the cross section, the luminosity and the corrections (as explained above), nS is the number of non-weighted simulated signal events after the selections (Sec. 4.4) and the sum \sum runs over the total unweighted number of signal (or background) events.

Table 4.5: Simulated samples used in the training of the DNN. Simulated processes and generators used are reported. All are interfaced to PYTHIA 8 for parton shower and hadronization simulation.

Process	Generators
VBS $W^+W^- jj \rightarrow 2l2\nu$	MADGRAPH5_aMC@NLO
QCD-induced $W^+W^- \rightarrow 2l2\nu$	POWHEG v2
$t\bar{t}$ + jets (2016)	MADGRAPH5_aMC@NLO (LO)
$t\bar{t}$ (2017)	POWHEG v2
$t\bar{t}$ (2018)	MADGRAPH5_aMC@NLO / POWHEG v2

4.5.3 Phase space selection

Various sets of selections have been tested to define the optimal DNN training phase space. The first tested training phase space was similar to the one described in Section 4.4, but with tighter selections on the two main discriminating observables: $m_{jj} > 500$ GeV and $\Delta\eta_{jj} > 3.5$. The selections on m_{jj} and $\Delta\eta_{jj}$ have been loosened to increase the number of events in the phase space region where the DNN was trained, allowing complexification of the network's structure (i.e. more nodes, layers, input variables). A more complex structure enhances the network's capability of processing information, resulting in better discrimination of the signal against the background.

Eventually, the training phase space was set equal to the signal region described in Section 4.4. Lowering more the m_{jj} or $\Delta\eta_{jj}$ selections only leads to an increase of background contamination with no significant gain in DNN discrimination power. On the other hand, tightening these selections produces a purer phase space at the expense of smaller training samples, increasing the probability of overtraining, thus reducing the network's performance.

4.5.4 Building a network

Two different models have been trained for the $Z_{\ell\ell} < 1$ and the $Z_{\ell\ell} \geq 1$ phase spaces. Their output combination is used to extract the results through a differential likelihood fit, as explained in Section 4.9. Particular caution is needed in the network

creation to find the minimum number of input variables and the best structure configuration. Indeed, by increasing the network dimension (number of layers and nodes) or the number of input variables, the model reaches a better discrimination power; unfortunately, too many variables and a complex structure may also lead to overtraining.

To find the optimal configuration, at first a very small DNN (2 hidden layers with 20 neurons each) with only a few variables (2-3) was created. Several models with the same number of variables but various architectures (number of nodes and layers) have been tested until the most performing one has been found. After this optimization in terms of the structure ended, new variables have been added to boost the network performance. A large set of observable (Table 4.6), including kinematic and angular variables of leptons and jets, among the most discriminating ones, have been tested as possible inputs of the DNN.

Table 4.6: Set of variables among the most discriminating ones, tested to be input of DNN. Their correlation matrix is reported in Figure 4.6.

Variable	Description
$\Delta\eta_{jj}$	Pseudorapidity interval between the two jets.
$p_T^{\ell\ell}$	Transverse momentum of the dilepton system.
$\Delta\eta_{ll}$	Pseudorapidity interval between the two leptons.
$p_T^{j_1}$	p_T of the leading jet.
$p_T^{j_2}$	p_T of the trailing jet.
p_T^{miss} (MET)	Missing Transverse Momentum.
$\Delta\phi_{ll}$	Difference in azimuth angle ϕ between the two leptons.
$\Delta\phi_{jj}$	Difference in azimuth angle ϕ between the two jets.
$m_{\ell\ell}$	Invariant mass of the dilepton system.
$\Delta R_{j,l_1}$	Distance of the leading lepton from the nearest jet in the $\phi - \eta$ plane.
$\Delta R_{j,l_2}$	Distance of the trailing lepton from the nearest jet in the $\phi - \eta$ plane.
Z_{ℓ_1}	Centrality of the leading lepton as defined in Equation 4.2.
Z_{ℓ_2}	Centrality of the trailing lepton as defined in Equation 4.2.
$m_T^{W_1}$	Transverse mass of the $(p_T^{\ell_1}, p_T^{\text{miss}})$ system.
$m_T^{W_2}$	Transverse mass of the $(p_T^{\ell_2}, p_T^{\text{miss}})$ system.
m_{jj}	Invariant mass of the dijet system.
$qgl_central$	Quark gluon discriminator of the first most central jet.
$qgl_forward$	Quark gluon discriminator of the forward jet.

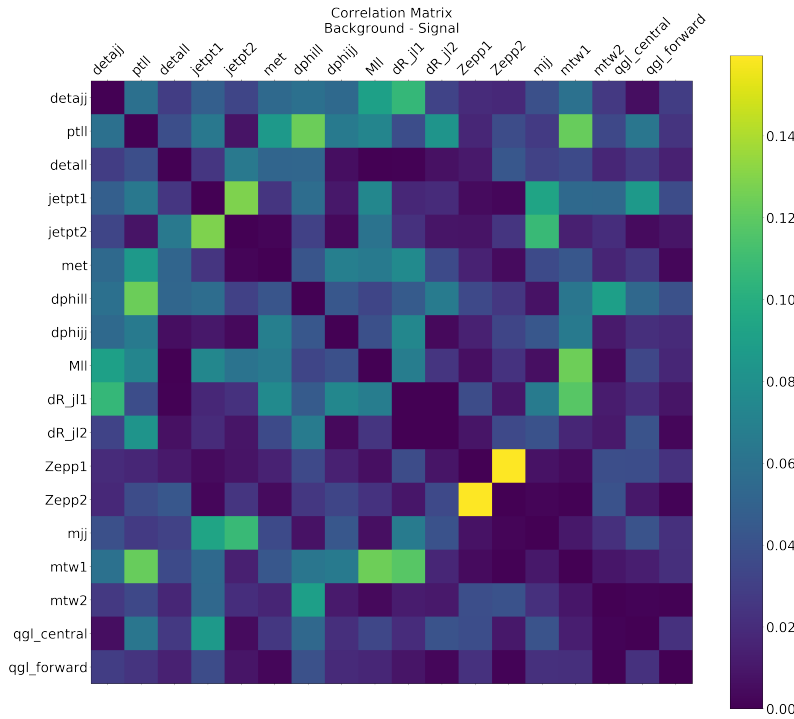


Figure 4.6: Difference between the input variables correlation matrix of backgrounds and signal in $Z_{\ell\ell} \geq 1$ phase space used to choose suitable input variables. A definition of the variables is reported in Table 4.6. Observables such as Z_{ℓ_1} or Z_{ℓ_2} , where differences are evident, have been preferred. Indeed, the DNN learns to distinguish signal events from the background through their differences.

The difference between the correlation matrices of signal and background for a set of possible input variables is reported in Figure 4.6; the difference of correlation matrices was studied to select the most suitable observables for the DNN. Indeed, the DNN exploits the differences between signal and background to learn how to separate them. Hence, variables such as Z_{ℓ_1} or Z_{ℓ_2} , where differences are enhanced, have been preferred. The procedure of feeding new variables to the DNN was repeated until the addition of a new input provided no further separation power.

The optimization of the models has been performed first in the $Z_{\ell\ell} \geq 1$ region, as it is the most challenging due to the limited amount of signal. In the $Z_{\ell\ell} < 1$ phase space, the same architecture of $Z_{\ell\ell} \geq 1$ was found to be the best choice. Moreover, the same input variables of the $Z_{\ell\ell} \geq 1$ model are used.

4.5.5 Final architecture and input variables

The two DNNs have been implemented in Keras, using the same structure for both the $Z_{\ell\ell} < 1$ and the $Z_{\ell\ell} \geq 1$ model: five hidden layers with 128, 128, 64, 64, 64 neurons, respectively. A schematic view of the network is reported in Figure 4.7. Since the task of the networks is binary classification, the most suitable choice for the loss function is the binary cross-entropy. The activation function for hidden

layers is the Rectified Linear Unit (ReLU) defined as $f(x) = \max(x, 0)$, while the sigmoid is chosen for the output layer.

The batch normalization technique [75] is applied before the activation function to standardize the mean and variance of the inputs in each layer. This procedure helps regularize the networks, thus improving the generalization capacity of the models. It also speeds up the training process, reducing the number of epochs needed.

Other regularization techniques are implemented to prevent over-fitting. L2 regularization of weights added as a penalty factor in the loss reduces the adaptation to the training data set. The early stopping [76] monitors and prevents overtraining by evaluating the loss on the validation data set. Indeed, it stops the training when the difference between the loss values calculated on the validation data set for two consecutive epochs is less than 0.0002 after 30 epochs.

The Adam optimization algorithm [77] is used to implement the stochastic gradient descent with an adaptive learning rate for each weight, leading to fast convergence of the training.

Table 4.7: Set of variables used as inputs to the DNN for both $Z_{\ell\ell} < 1$ and $Z_{\ell\ell} \geq 1$ models. The order of the table does not correspond to variable importance.

Variable	Description
m_{jj}	Invariant mass of the two VBS jets
$\Delta\eta_{jj}$	Pseudorapidity gap between the two VBS jets
$p_T^{j_1}$	p_T of the leading jet
$p_T^{j_2}$	p_T of the trailing jet
$p_T^{\ell\ell}$	p_T of the lepton pair
$\Delta\phi_{\ell\ell}$	Azimuthal angle between the two leptons
Z_{ℓ_1}	Zeppenfeld variable of the leading lepton
Z_{ℓ_2}	Zeppenfeld variable of the trailing lepton
$m_T^{W_1}$	Transverse mass of the $(p_T^{\ell_1}, p_T^{\text{miss}})$ system

Nine variables have been selected, with the procedure described in Section 4.5.4, as inputs of the two networks, including both kinematic and angular properties of leptons and jets. They are a subsample of the observables described in Table 4.6 and are reported, along with their description, in Table 4.7.

The shape of final input variables for the electroweak W^+W^- signal (violet), $t\bar{t}$ - tW (yellow) and QCD-induced W^+W^- backgrounds (light blue) is reported in Figure 4.8 for $Z_{\ell\ell} \geq 1$ phase space. The observed shape differences between signal and background in those variables give a rough idea of their discrimination power. Indeed, shape differences in the input observables are one of the features exploited by the DNN to predict if the event is signal or background.

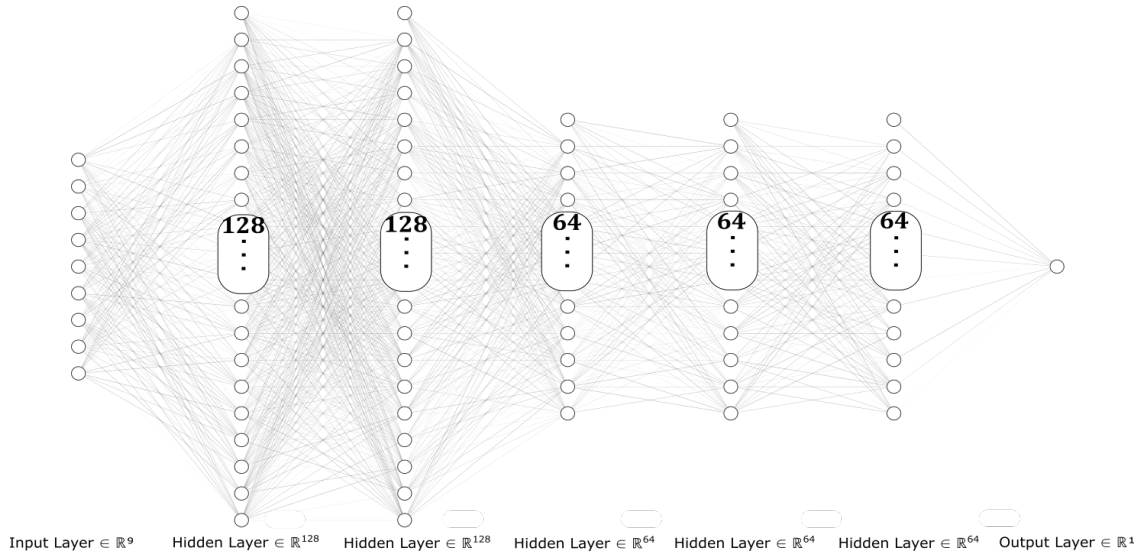


Figure 4.7: Schematic view of the DNN architecture: one input layer, five hidden layers, and an output layer. The five dense layers are composed of different numbers of neurons. Each circle represents a neuron, biases are also shown.

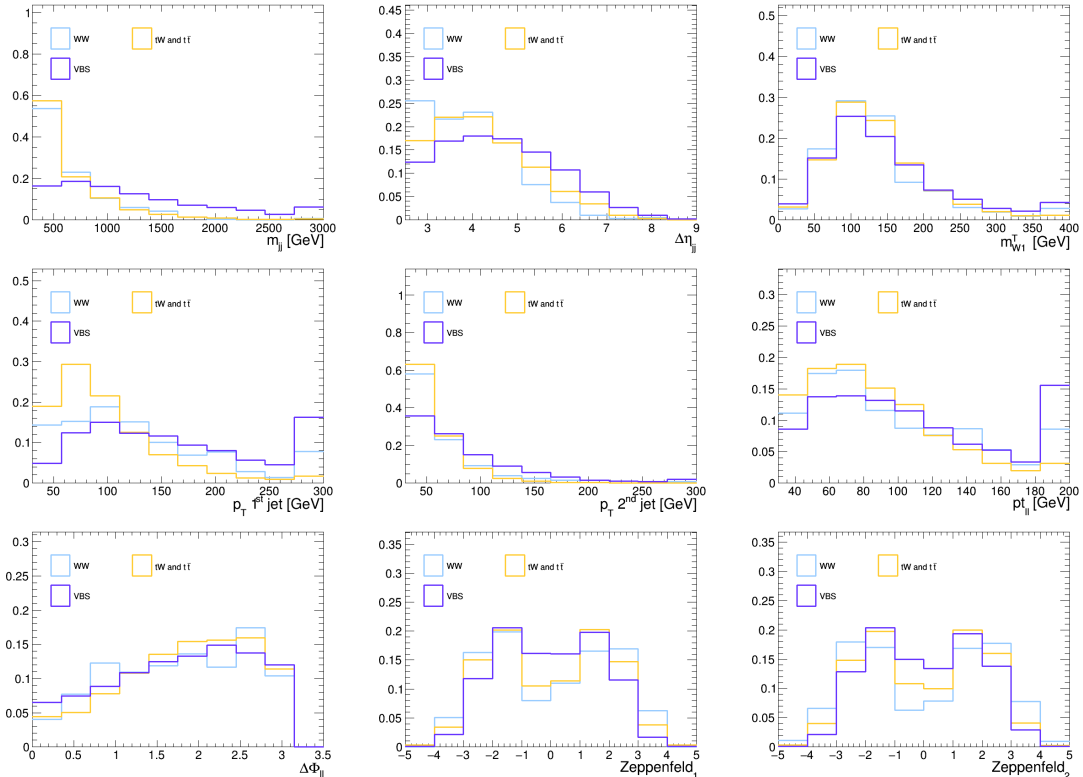


Figure 4.8: Shape of the input variables in the $Z_{\ell\ell} \geq 1$ signal region for the signal (violet), $t\bar{t}$ - tW (yellow) and QCD-induced W^+W^- (light blue). Histograms are normalized to one.

4.5.6 Training monitoring and performance

The training monitoring is performed with metrics evaluated on the training and validation data set. The splitting of the training sample into a training and a validation data set (as explained in Section 4.5.2) is essential to check the training process of the network, identifying any possible hint of overtraining and evaluating the model's performance.

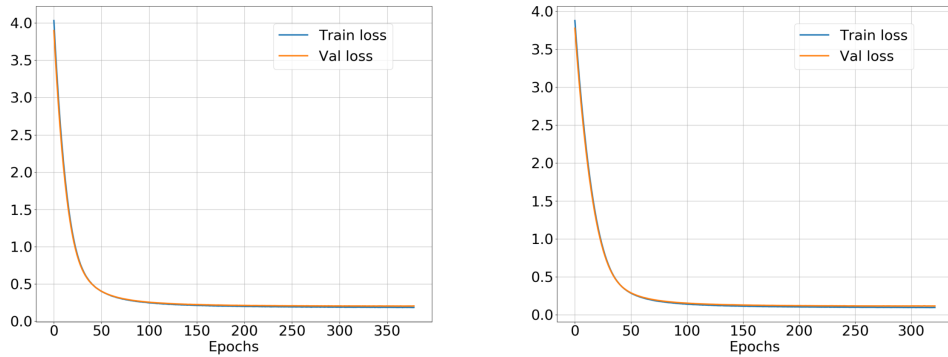


Figure 4.9: Loss function for the two DNN models. $Z_{\ell\ell} < 1$ on the left and $Z_{\ell\ell} \geq 1$ on the right.

The binary cross entropy (the loss function) is used as a metric. Indeed, a characteristic sign of overtraining is when the value of the loss function estimated on the training data set monotonically decreases, whereas the one evaluated on the validation data set increases. In Figure 4.9, the loss functions, evaluated on the training (blue line) and the validation (orange line) data set, monotonically decrease during all the training, showing no sign of overtraining.

The efficiency (or recall) and the purity (or precision) metrics are considered as well; they are defined as follow

$$\text{Efficiency} = \frac{\text{True Positive}}{\text{True Positive} + \text{False Negative}},$$

$$\text{Purity} = \frac{\text{True Positive}}{\text{True Positive} + \text{False Positive}},$$

computed both with a threshold on the DNN output to be classified as positive set at 0.85.

In Figure 4.10, the evolution of these other two metrics during the training of the $Z_{\ell\ell} < 1$ and $Z_{\ell\ell} \geq 1$ models are drawn as a function of the epochs. In the calculation of these metrics, the signal and background data sets are not balanced with weights of Equation 4.6. A difference in the purity calculated on the training and validation data sets is visible, probably caused by the limited size of the background and signal samples used in the training and validation, and the large weights in the

background samples. Indeed, samples used in the training (validation) are different from the ones used in the analysis. As explained in Section 4.5.2, the choice was made in order to give more reliability to the network at a cost of sacrificing a bit of statistical power in the training since alternative data sets were centrally produced with fewer events. So, even though the behavior reported in Figure 4.10 is not optimal, is not even critical and could be ascribed to a lack of statistics of the samples themselves. The behavior of other metrics (in particular the loss but also the recall) on the training and validation samples is more acceptable, showing no concerning pattern and evidencing no sign of overtraining. In addition, as will be explained in the following (cf Figure 4.11), the performance on the samples used in the analysis, which are completely different from those used in the training, show that the network is able to classify events never seen before. Hence, the performance of the models is considered satisfactory and reliable.

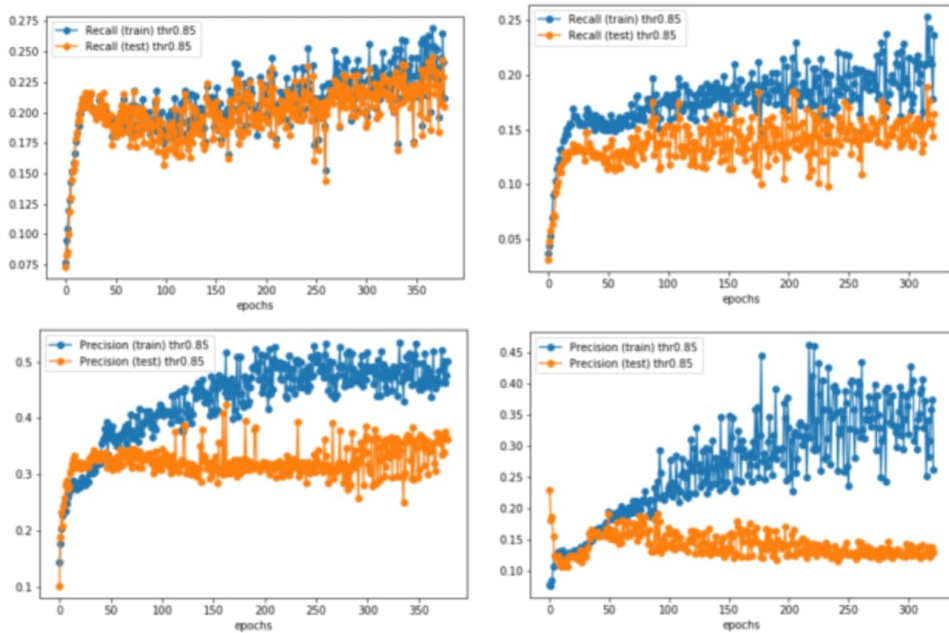


Figure 4.10: Upper row: the efficiency (recall) of the two DNN models. Bottom row: purity (precision) for the two DNN models. The two metrics are both evaluated with a threshold on the DNN output at 0.85. $Z_{\ell\ell} < 1$ on the left and $Z_{\ell\ell} \geq 1$ on the right.

After the training procedure is completed, the models are applied to the samples of the analysis (testing samples) to evaluate their performance. In Figure 4.11, the distributions of the DNN output evaluated on training and testing samples are shown. The overlapping between the blue-azure (background) and the orange-red (signal) curves means that our models can generalize and maintain a good predictivity when applied to new events.

As explained in Section 4.5.4, several models with a different number of variables and various structures have been tested.

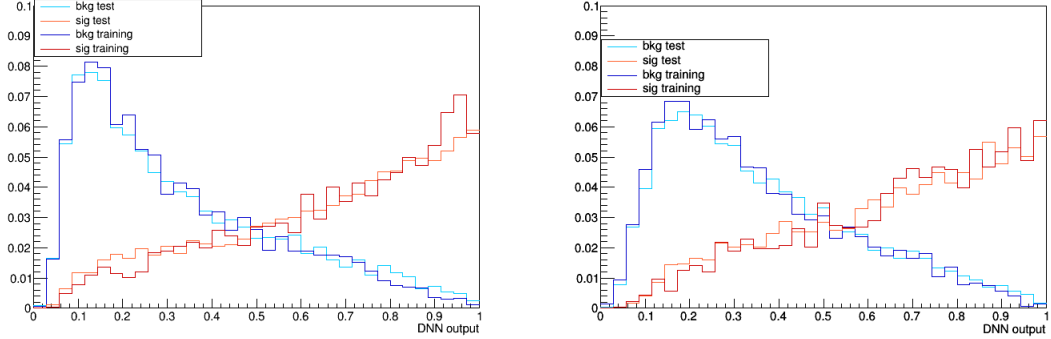


Figure 4.11: DNN score obtained with the training and testing samples. $Z_{\ell\ell} < 1$ on the left and $Z_{\ell\ell} \geq 1$ on the right.

The Receiver Operating Characteristics (ROC) [78] curve represents the signal efficiency (on the y-axis) versus the background contamination (on the x-axis) for several thresholds imposed on a discriminating observable. The ROC curve of each model has been studied using the testing samples to evaluate its performance and choose the most suitable one. The ROC curve obtained using m_{jj} as a discriminating variable is used as a benchmark. This ROC curve is obtained using the binned differential distribution of m_{jj} in a tighter phase space with $m_{jj} > 500$ GeV and $\Delta\eta_{jj} > 3.5$. Indeed, the standard cut-based analysis splits only this purer region in m_{jj} bins (as would be explained in Section 4.9.2). In Figure 4.12 a comparison between the DNN and m_{jj} ROC curves is shown. The two curves are rescaled to consider the different selections in m_{jj} and $\Delta\eta_{jj}$. The DNN curves (blue and red lines) are above the m_{jj} one (black line) in all their phase spaces, even in the very low-efficiency region. For a fixed amount of background contamination, the DNN always reaches a better signal purity than m_{jj} , implying that an improvement in the performance of the analysis is expected when using the DNN output as a discriminator.

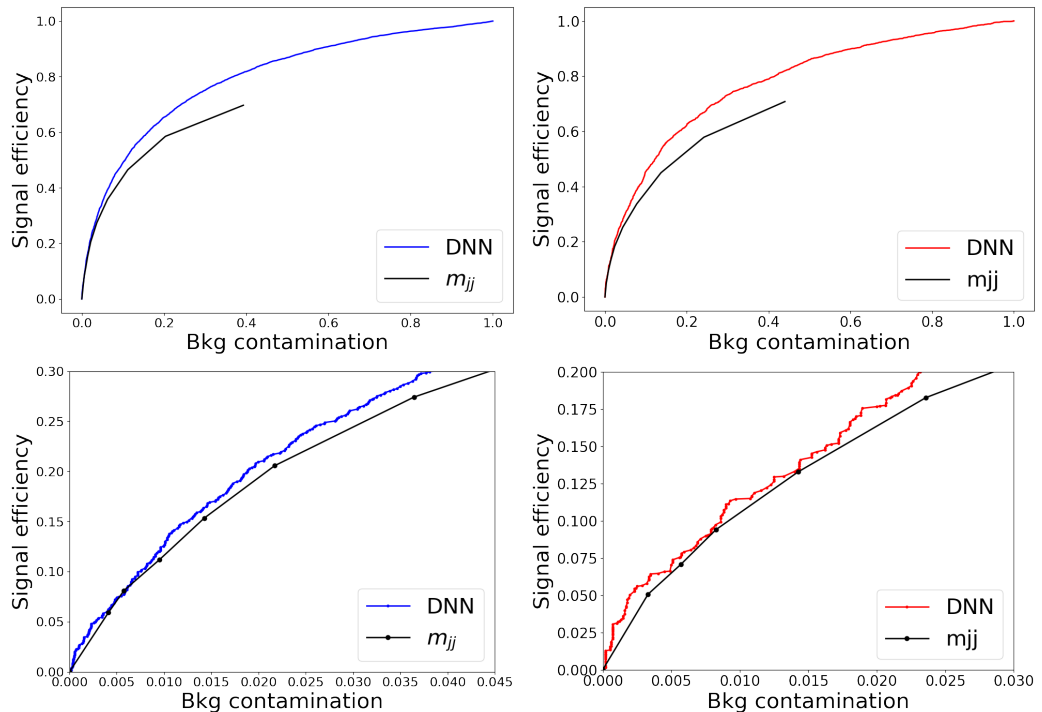


Figure 4.12: Upper row: ROC curves of m_{jj} and DNN for the full Run II data set. Bottom row: zoom in the low efficiency region. On the left: $Z_{\ell\ell} < 1$. On the right: $Z_{\ell\ell} \geq 1$.

4.6 Control regions

As explained in Section 4.4, several control regions, orthogonal to the signal ones, are defined to monitor the agreement of the simulations with the data. These control regions are enriched either in $t\bar{t}$ - tW or DY backgrounds, which constitute two of the main backgrounds.

Figure 4.13 shows the general comparisons of observation and prediction in the $t\bar{t}$ - tW enriched phase space for $e\mu$ category for some of the main discriminating variables (such as m_{jj} , $\Delta\eta_{jj}$, Z_{ℓ_1} and Z_{ℓ_2}), which are also used as input of the DNN (cf. Sec. 4.5.5). The agreement between data and simulations is good in all the observables. The same good agreement is observed in the ee and $\mu\mu$ final states.

Figure 4.14 shows the comparisons of observation and prediction for the same set of variables in the $DY\tau\tau$ enriched phase space. A good agreement is observed between data and MC simulations in all the observables.

In the $ee/\mu\mu$ final state, two different DY sub-samples are defined, as shown in Figure 4.15. One (light green histogram) contains events in which at least one of the two leading jets arises from a secondary vertex (DY PU); the other (dark green histogram) includes all the events with jets only from the primary interaction vertex (DY hard). As can be seen in the figure, the $\Delta\eta_{jj} \geq 5$ is enriched in DY PU events since this region is outside the tracker’s acceptance; while the $\Delta\eta_{jj} < 5$ is more populated by the hard component of the process. The DY control region is split into $\Delta\eta_{jj}$ macro-bins to gain sensitivity on these two different contributions; their normalization is adjusted separately during the maximum likelihood fit, as will be explained in 4.7.

Figure 4.16 and Figure 4.17 show the general comparisons of observation and prediction in the DY enriched control regions for the ee category in the $\Delta\eta_{jj} < 5$ and the $\Delta\eta_{jj} \geq 5$ phase spaces, respectively. Similar behavior is observed in the $\mu\mu$ final state.

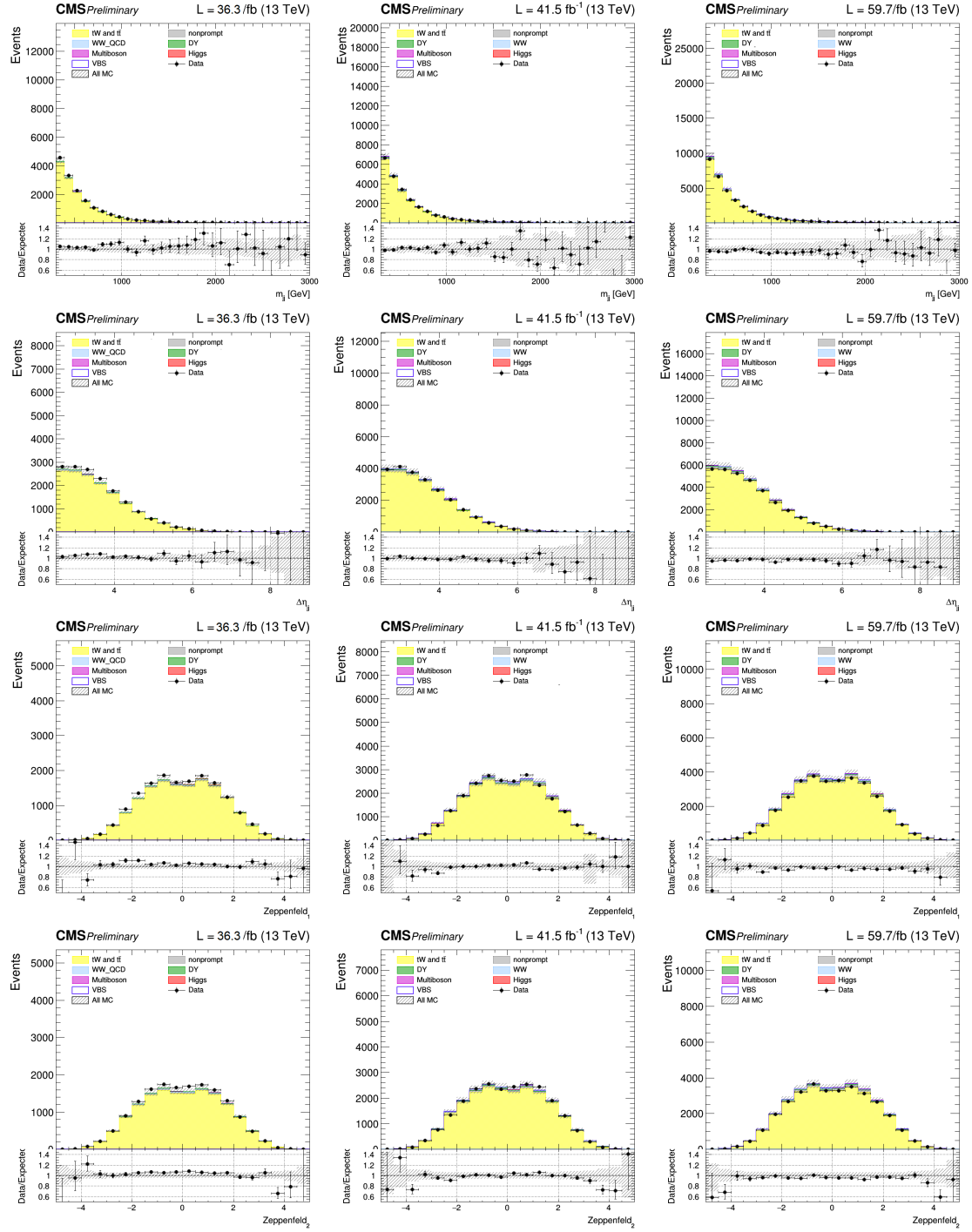


Figure 4.13: Comparison of observation and prediction in the $t\bar{t}$ - tW $e\mu$ control region from the 2016 (left), 2017 (center) and 2018 (right) samples. From top to bottom: dijet mass, pseudorapidity gap of the two jets, the two Zeppenfeld variables.

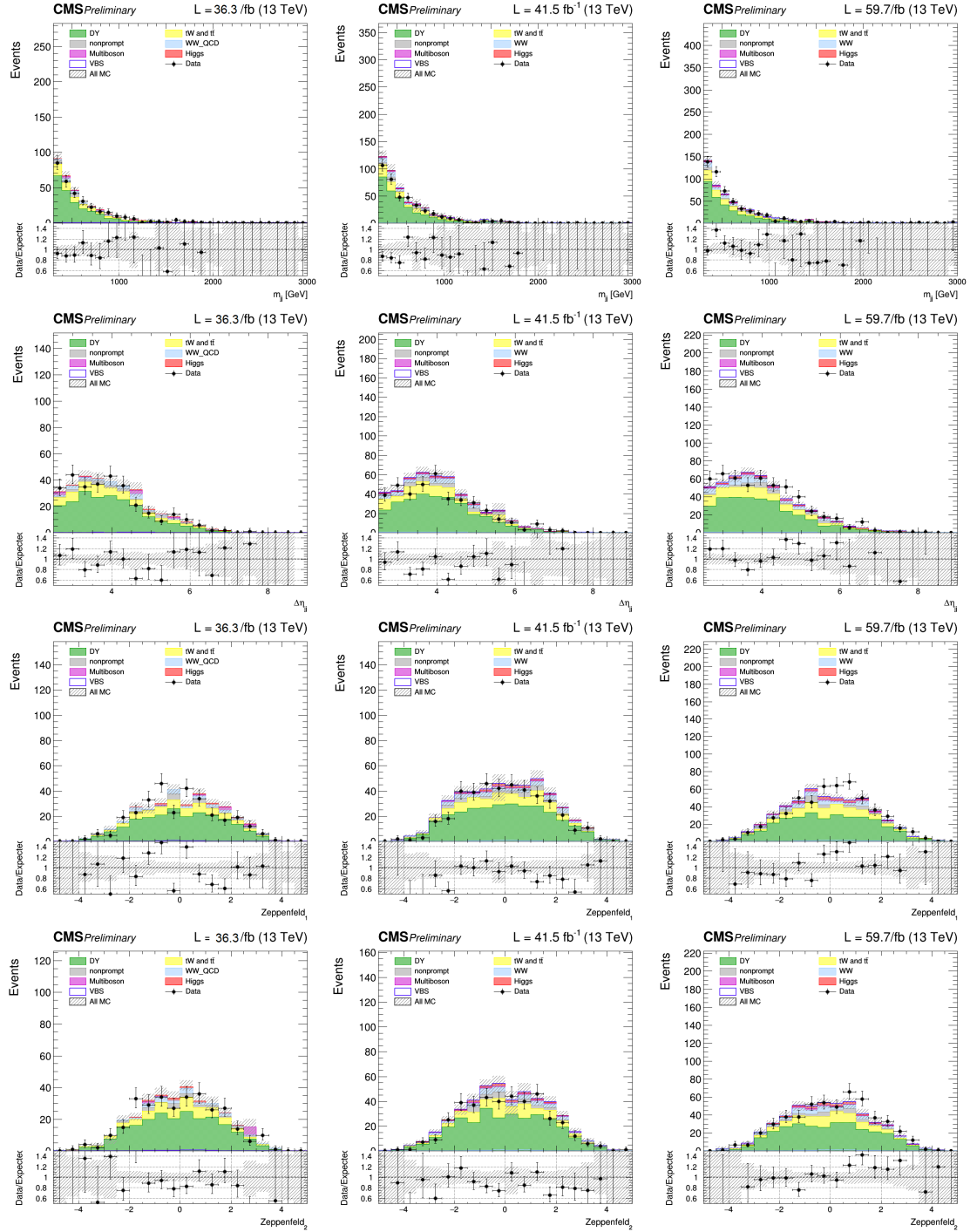


Figure 4.14: Comparison of observation and prediction in the $DY\tau\tau$ control region from the 2016 (left), 2017 (center) and 2018 (right) samples. From top to bottom: dijet mass, pseudorapidity gap of the two jets, the two Zeppenfeld variables.

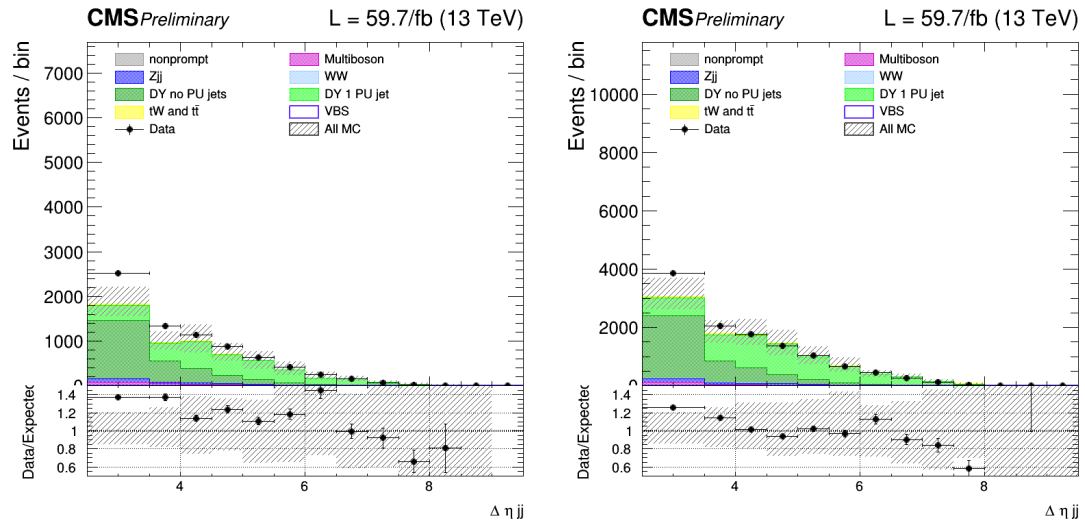


Figure 4.15: The $\Delta\eta_{jj}$ distribution in the ee (left) and $\mu\mu$ (right) DY control regions for the 2018 samples. Different contributions from DY with or without one additional PU jet are reported with different shades of green.

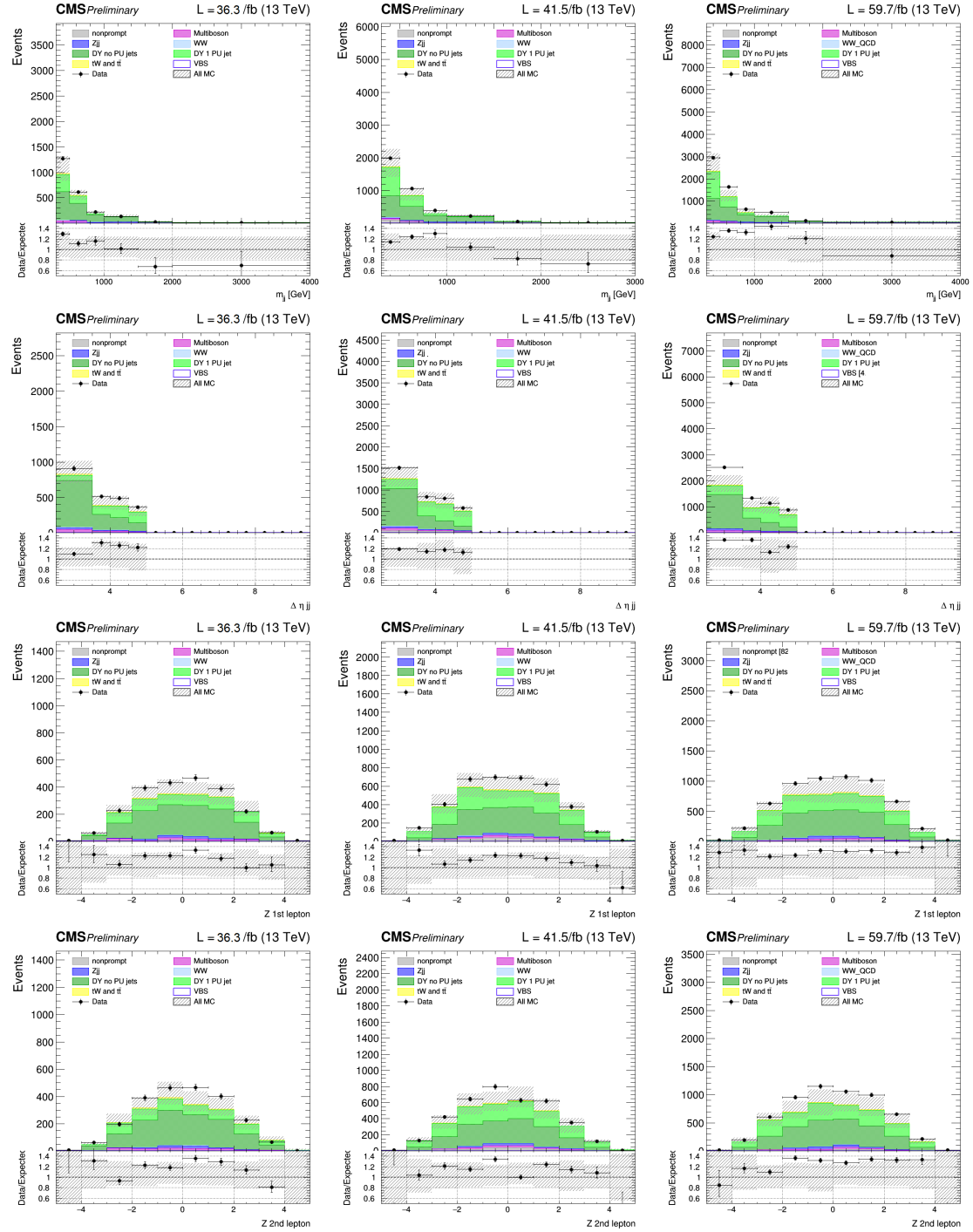


Figure 4.16: Comparison of observation and prediction in the $DY ee$ $\Delta\eta_{jj} < 5$ control region from the 2016 (left), 2017 (center) and 2018 (right) samples. From top to bottom: dijet mass, pseudorapidity gap of the two jets, the two Zeppenfeld variables.

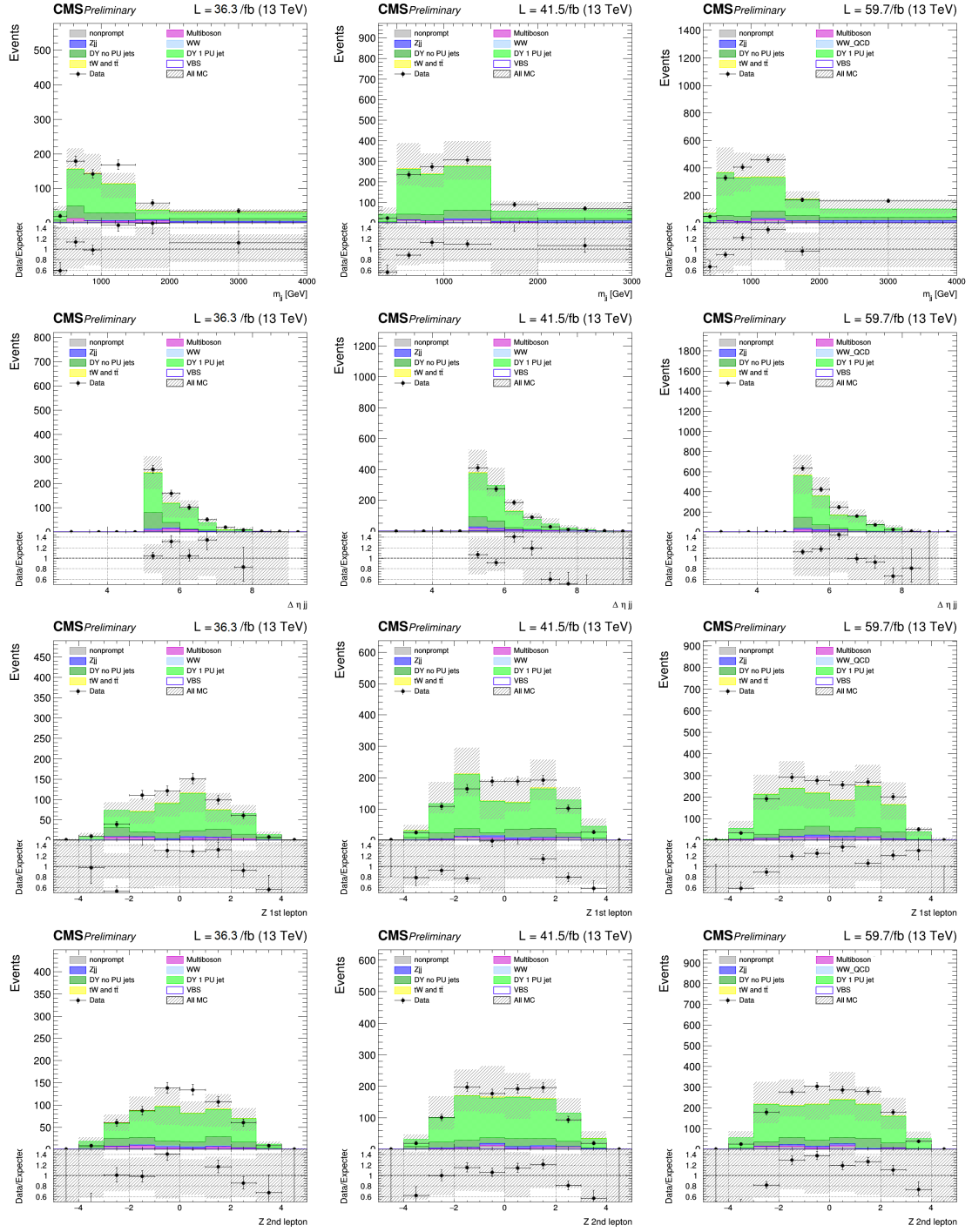


Figure 4.17: Comparison of observation and prediction in the DY ee $\Delta\eta_{jj} \geq 5$ control region from the 2016 (left), 2017 (center) and 2018 (right) samples. From top to bottom: dijet mass, pseudorapidity gap of the two jets, the two Zeppenfeld variables.

4.7 Background estimation

The $t\bar{t}$ - tW production is the main background process; its contribution in the signal region is estimated through a data-driven technique. A control region enriched in $t\bar{t}$ - tW , as defined in Section 4.4, is included in the fit to determine the normalization of this background.

In ee and $\mu\mu$ categories, the DY production is one of the dominant background processes. The tagging jets related to this background derive from the hard interaction vertex only in a fraction of events (hard DY). Indeed, a contribution to this background arises also from events where at least one of the two tagging jets is emitted from a pileup vertex (pileup DY). These two contributions (the hard and pileup ones) are treated as distinct processes with two different parameters, estimated in the fit procedure with two specific control regions. In particular, the DY control region with $\Delta\eta_{jj} < 5$ is enriched by hard events with only jets from the primary vertex, while the one with $\Delta\eta_{jj} \geq 5$ is contaminated mainly by events with jets from pileup interactions.

In the $e\mu$ category, the DY background reduces to DY $\tau\tau$, where the tau leptons decay leptonically. This small contribution is estimated through a so-called embedded sample obtained with data-driven techniques. In the data embedded sample, simulated tau leptons replace the muons in $Z \rightarrow \mu\mu$ events from data. These simulated tau leptons maintain the four momenta of the removed muons. A data embedded sample ensures better modeling than MC simulation for those observables, such as p_T^{miss} , more sensitive to detector response and calibration. The details of this technique are explained in reference [79]. MC simulations are used to model the small number of events entering the analysis phase space that fires the single-lepton triggers and is not included in the data embedded sample. Eventually, the normalization of the DY $\tau\tau$ background is constrained in the fit through the DY $e\mu$ control region.

The normalization of the nonresonant QCD-induced W^+W^- background is not fixed, as the $t\bar{t}$ - tW and DY ones, and it is determined during the fit procedure. Unfortunately, it is not easy to define a pure enough phase space to isolate this background, due to $t\bar{t}$ - tW , $W + \text{jets}$, and DY (mainly in ee and $\mu\mu$) contamination. Therefore, the normalization of W^+W^- is constrained in the fit without a corresponding control region.

Another source of background estimated directly from data is the nonprompt leptons background [64], originating mainly from $W + \text{jets}$ events. The estimate is performed with a control sample, enriched in these events, and a separated control region, enriched in QCD dijet events. The $W + \text{jets}$ events are selected in data requiring one candidate lepton with tight isolation and identification criteria (the same used in the analysis) and a second candidate with loose requirements that fails the tight ones. The dijet control region contains data events filtered with dedicated triggers, requiring one electron and one jet or a single muon, with such loose selections to enrich the sample in nonprompt leptons. In addition, leptons selected in this way are required to be well isolated from the highest- p_T jet. The probability

that nonprompt events from the dijet control region pass also the tight requirements of the analysis is evaluated as a function of the η and p_T of the nonprompt leptons. To avoid biases in this estimate, due to contribution from real leptons, a cut on $p_T^{\text{miss}} < 20 \text{ GeV}$ is applied to suppress events from leptonic W boson decays and subtraction of DY simulated events from data is performed to eliminate the contribution from the electroweak production of Z + jets. The probability is then applied on the W + jets control sample to predict the number of W + jets events entering the signal region.

Other minor background sources include the Higgs boson production and the multiboson processes, which are completely derived from simulation. The Higgs boson production is strongly suppressed by the $m_{\ell\ell}$ cut, whereas the multiboson processes are highly reduced by excluding events with a third additional lepton.

4.8 Systematic uncertainties

In the maximum likelihood fit, systematic uncertainties affecting the measurements are included as nuisance parameters. Correlations between them in different categories are taken into account as well. The systematic uncertainties considered in this analysis may affect the overall normalizations as well as the shapes of the templates for the signal and backgrounds processes.

The integrated luminosity is measured with an uncertainty of 1.2%, 2.3%, and 2.5% for 2016, 2017, and 2018 data sets, respectively [50, 51, 52], producing a 2.1% impact on the signal cross section. Uncertainties related to trigger efficiency affect only the normalization of the templates and are of the order of less than 1%, while the ones in lepton reconstruction and identification efficiencies cause shape variations also with an impact of order 1.5% for electrons and 2% for muons [80, 81]. Additional trigger corrections for the 2016 and 2017 data sets (prefiring corrections) produce a combined 3.3% uncertainty on the signal yield. The effect of the lepton momentum scale and jet momentum scale and resolution uncertainties [82] modify the shape and the normalization of templates. These changes are evaluated by shifting the p_T of the leptons and the jets of one standard deviation from their nominal value. The impact on the signal cross section is less than 1% from the uncertainties related to the leptons and 2.6% from the uncertainties related to the jets. Uncertainties in p_T^{miss} [83] not related to lepton and jet momentum scales are estimated by varying the momentum of each PF candidate not associated with a lepton or a jet; these result in a 2.4% impact on the signal cross section. The b tagging [72] corrections are related to several uncertainty sources, with a total impact on the signal yield of 3.5%. The uncertainty on the pileup reweighting procedure is evaluated to be of order 1.8%.

The theoretical uncertainties related to the choice of QCD renormalization and factorization scales are computed by independently modifying the scales up and down by a factor of two with respect to their nominal values. The extreme cases where they are shifted in opposite directions are not considered [84, 85]. As mentioned in Section 4.7, the normalizations of the main backgrounds are constrained

from data. The normalization of the signal as well is measured directly in the fit. Hence, in the QCD scales, only shape's effects are considered. As explained in Section 1.2, the VBS W^+W^- signal is a purely electroweak process at LO. No effect is thus observed by changing the renormalization scale, which affects the coupling of α_S . Hence, for the signal, only shape effects related to the change of the factorization scale are considered. PDF uncertainties may affect only shapes for both signal and background since their normalizations are constrained in the fit. As to the signal, it has been checked that no significant effects in the shape of the DNN or m_{jj} variable are visible due to PDFs. As to major backgrounds, the only effect of PDF changes should result in a difference in yield between different phase spaces (signal and control regions). However, such uncertainties are already addressed including an error on the yield of the major backgrounds in the control region of 1% and 2% for $t\bar{t}$ and DY backgrounds, respectively. Eventually, uncertainties on PDFs are not included in the fit for signal and background processes. Uncertainties on the modeling of parton shower and underlying event have an impact on the signal yield of 1% and 1.3%, respectively.

Table 4.8 summarizes the percentage values of the most relevant systematic uncertainties affecting the signal cross section measurement. Uncertainties with a value of less than 1% are not mentioned. The most relevant uncertainties are theoretical ones: the QCD factorization scale for the VBS signal and the QCD scale (renormalization and factorization) of $t\bar{t}$ background. Among experimental uncertainties, the b tagging ones are the most impactful since the b veto directly affects the number of events entering the signal region. Statistical uncertainty is still dominating the total uncertainty. Indeed, the sum in quadrature of all the sources of systematic uncertainties amounts to a relative uncertainty on the cross section of 13.1%, while the statistical component is estimated to be 14.9%. The estimate of the statistical uncertainty is performed by setting all the components of the systematic uncertainties to their best-fit values. Eventually, the total relative uncertainty on the signal cross section is 19.9%. This analysis, as the other VBS ones, is therefore expected to benefit from the collection of a larger data sample.

Figure 4.18 shows the best-fit values (left column), and the impacts (right column) of the first 30 nuisance parameters of the fit. The parameters are ordered from the most to the less impactful ones. The impact of a nuisance is calculated performing a maximum likelihood fit where the nuisance value is shifted of one sigma with respect to its best-fit value and the others nuisance parameters are profiled. The impact on the signal strength modifier is then estimated as the difference between the new value of the signal strength and the one found in the nominal fit. Some nuisance parameters are slightly pulled or constrained but no concerning behavior is observed.

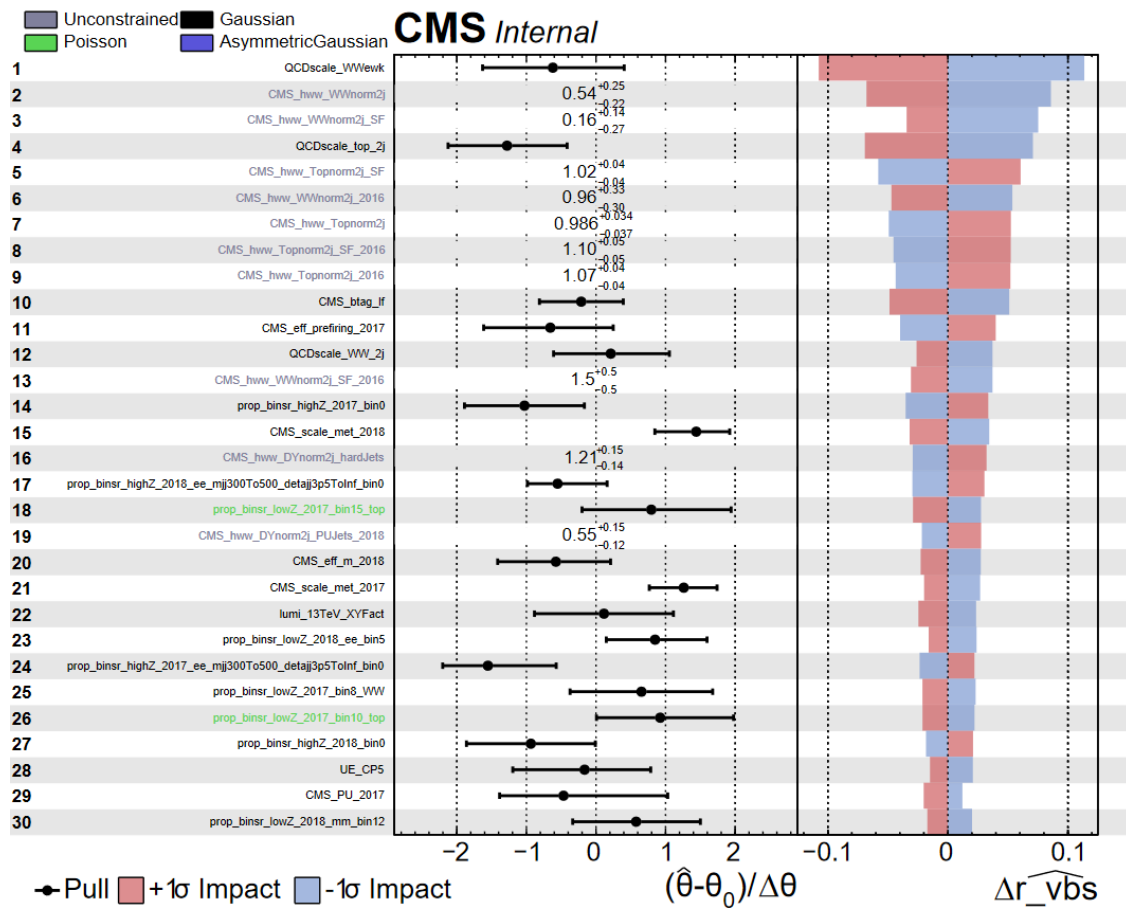


Figure 4.18: Best-fit values and impacts of the first 30 impactful nuisance parameters in the combined fit with the 2016–2018 data sets. Best-fit values are reported in the picture for nuisance parameters (black point) and for normalization parameters (grey) for the $t\bar{t}$, DY and QCD-induced W^+W^- backgrounds, which are constrained directly from the fit to data.

Table 4.8: Systematic uncertainties affecting the signal cross section. Only uncertainties with a value greater than 1% are shown. Statistical uncertainty is also reported along with the sum of systematic contributions and the total contribution.

Uncertainty source	Value
QCD-induced W^+W^- normalization	5.3%
$t\bar{t}$ QCD scale	5.1%
QCD factorisation scale for VBS signal	5.0%
$t\bar{t}$ normalization	4.9%
b tagging	3.5%
Trigger corrections	3.3%
DY normalization	2.9%
Jet energy scale + resolution	2.6%
p_T^{miss} energy scale	2.4%
QCD-induced W^+W^- QCD scale	2.1%
Integrated luminosity	2.1%
Muon efficiency	2.0%
Pileup	1.8%
Electron efficiency	1.5%
Underlying event	1.3%
Parton shower	1.0%
Other	< 1%
Total systematic uncertainty	13.1%
Total statistical uncertainty	14.9%
Total uncertainty	19.8%

4.9 Signal extraction

4.9.1 Statistical procedure

A modified frequentist approach based on a likelihood maximum fit of differential distributions is adopted to extract the VBS signal strength μ , defined as the ratio of the observed to expected signal yields. The signal strength is thus used to scale the expected cross section and extract the observed cross section value.

The likelihood is defined as the product of N Poisson's distributions, one for each bin in the differential distributions of the signal and control regions,

$$\mathcal{L}(\vec{n}|\mu, \theta) = p(\theta) \cdot \prod_{i=1}^N \text{Poisson}(n_i|\mu \cdot s_i(\theta) + b_i(\theta)) \quad (4.7)$$

where n_i is the data yield, s_i and b_i are the expected event yields for the signal

and backgrounds templates in the i -th bin and $p(\theta)$ are the log-normal distributions for the nuisance parameters, θ accounting for systematic uncertainties. A value of μ equal to zero corresponds to the background-only hypothesis, meaning that no signal events are found. Hence, this background-only hypothesis has to be tested and discarded to find evidence of the signal process. This is achieved through the profile likelihood ratio

$$\lambda(0) = \frac{\mathcal{L}(0, \hat{\theta})}{\mathcal{L}(\hat{\mu}, \hat{\theta})} \quad (4.8)$$

The likelihood in the numerator has μ fixed to 0 (background-only hypothesis) and $\hat{\theta}$ fitted, whereas the likelihood in the denominator has both $\hat{\mu}$ and $\hat{\theta}$ fitted to find their values that maximize the likelihood. The profile likelihood ratio defined above spans from zero to one, where values towards zero underline a discrepancy between the data and the background-only hypothesis.

Eventually, a proper test statistic is defined as $t_0 = -2 \ln(\lambda(0))$ [86] to quantify the incompatibility between data and the background-only hypothesis in terms of the p-value [87], computed as

$$p_0 = \int_{t_0^{obs}}^{+\infty} f(t_0|0) dt_0 \quad (4.9)$$

where the $f(t_0|0)$ represents the probability density function of the test statistic, assuming the validity of the background-only hypothesis.

When the p-value is below a fixed threshold, the background-only hypothesis is rejected and discovery of the signal is claimed. In particle physics, it is more convenient to report the results in terms of an equivalent significance, related to the area under the tail of a Gaussian distribution. The threshold set for discovery corresponds to 5 standard deviations.

4.9.2 Results

In the $e\mu$ signal region, the signal phase space is divided into bins of the DNN output, as explained in Section 4.5, whereas in ee and $\mu\mu$ categories, the signal phase space is separated into four m_{jj} and $\Delta\eta_{jj}$ regions, defined as follows:

- $300 \text{ GeV} < m_{jj} < 500 \text{ GeV}$ and $2.5 < \Delta\eta_{jj} < 3.5$;
- $m_{jj} > 500 \text{ GeV}$ and $2.5 < \Delta\eta_{jj} < 3.5$;
- $300 \text{ GeV} < m_{jj} < 500 \text{ GeV}$ and $\Delta\eta_{jj} > 3.5$;
- $m_{jj} > 500 \text{ GeV}$ and $\Delta\eta_{jj} > 3.5$.

The first three are single-bin regions, where the number of events is fit to data. The last one, which has the highest signal-to-background ratio, is further divided

into bins of m_{jj} . Regardless of the final state, in all the control regions the number of events is fit to data to constraint the normalizations of the $t\bar{t}$ - tW and DY backgrounds.

A maximum-likelihood fit is used to discriminate between the signal and the other backgrounds; the signal strength modifier (μ_{EW}) of the EW W^+W^- process is the only parameter of interest in the fit, which includes all the binned distributions of the signal and control regions described above. From the measurement of μ_{EW} , the production cross section of the EW W^+W^- production is estimated into two different fiducial volumes.

In Table 4.9, the post-fit yields of the different processes in the VBS $e\mu$ and $ee - \mu\mu$ signal regions are reported. The categories with the $e\mu$ final state leptons give the main contributions to the significance since they have a better signal-to-background ratio than the ee and $\mu\mu$ ones. Indeed, the purity of the ee and $\mu\mu$ categories is spoiled by the large presence of DY production. However, the same flavor channels produce an improvement in the analysis performance; they help reach the five σ threshold for observation.

Table 4.9: Post-fit yields of the signal process (first row) and different background processes in the signal regions, as defined in Sec. 4.4. The $Z_{\ell\ell}$ categories have been merged as well as the ee and $\mu\mu$ ones.

Process	VBS $e\mu$	VBS $ee/\mu\mu$
$W^+W^- jj$	238.9 ± 21.9	136.3 ± 6.9
Z_{jj}	$- \pm -$	60.8 ± 4.4
$t\bar{t} tW$	3081.9 ± 99.7	1410.3 ± 19.6
DY_PUJets	$- \pm -$	560.1 ± 46.9
DY_hardJets	$- \pm -$	667.7 ± 32.2
DY	171.2 ± 7.3	$- \pm -$
QCD-WW	736.3 ± 98.8	232.6 ± 24.0
Higgs	46.6 ± 1.8	$- \pm -$
Nonprompt	216.8 ± 24.6	62.0 ± 6.4
Multiboson	143.3 ± 9.8	121.1 ± 7.5

The observed post-fit distributions of the binned DNN output in the $e\mu$ categories and the bins in m_{jj} - $\Delta\eta_{jj}$ for the ee and $\mu\mu$ categories are shown in Figures 4.19 and 4.20, respectively. The histograms, stacked on top of each other, represent the contribution of all the background processes and the signal. The signal (in violet) is drawn both standalone and superimposed on the other processes. The dashed grey bands show the systematic uncertainties. Figure 4.21 shows the number of post-fit events in the control regions for all the flavors of the final state leptons. The good agreement between the simulations and the data ensures the reliability of the obtained results.

Figure 4.22 shows the so-called background-subtracted plot for the $e\mu$ categories; the background-subtracted plot helps visualize the signal presence over the background. Indeed, this plot compares the data minus the total post-fit background

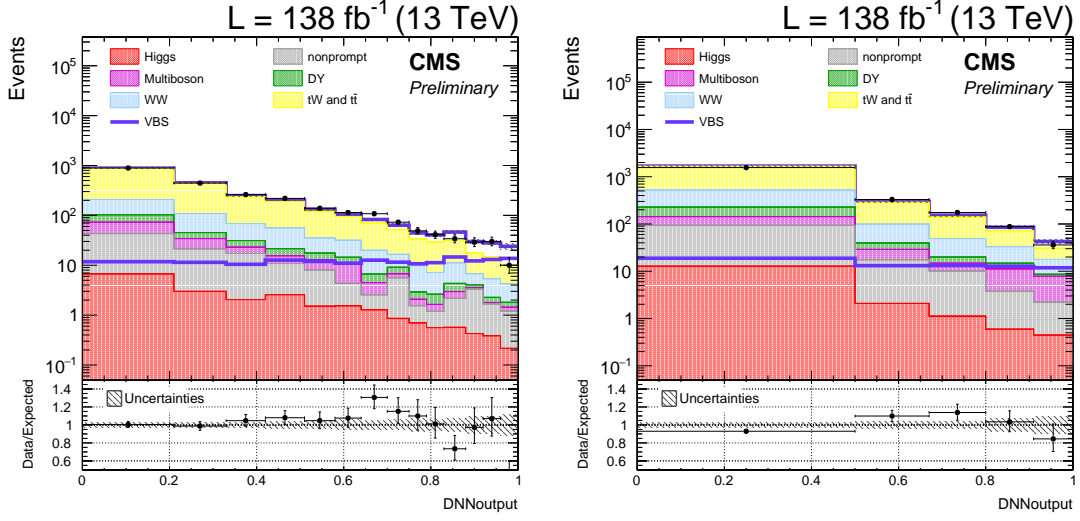


Figure 4.19: Post-fit DNN distributions in $e\mu$ categories for $Z_{\ell\ell} < 1$ (on the left) and $Z_{\ell\ell} \geq 1$ (on the right). The bottom panel of the plots shows the ratio between the number of events in data and the total number of expected events.

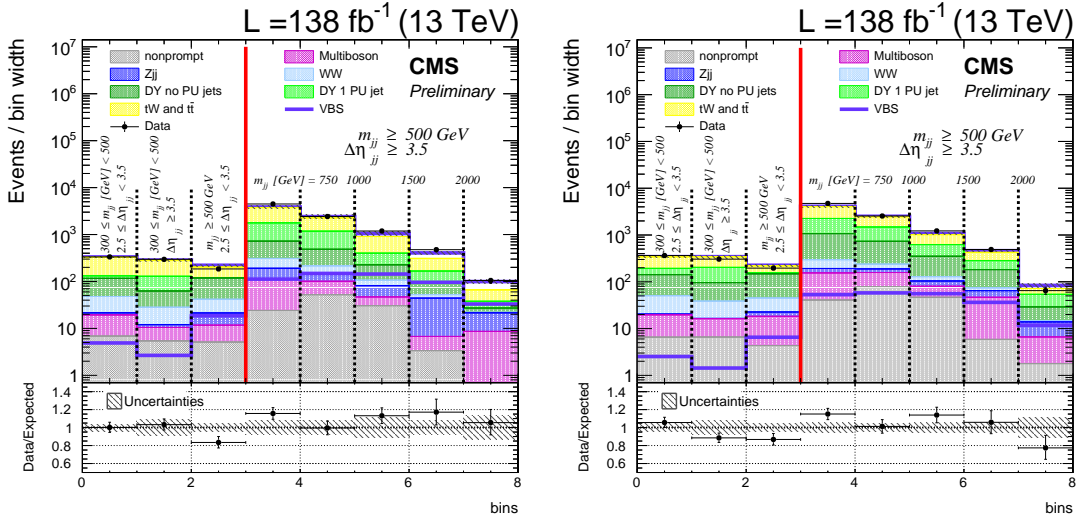


Figure 4.20: Post-fit distributions in the ee and $\mu\mu$ combined and in the $Z_{\ell\ell} < 1$ category (on the left) and $Z_{\ell\ell} \geq 1$ category (on the right). In each plot, all the $\Delta\eta_{jj}$ and m_{jj} bins are reported (see text). The last five bins represent the m_{jj} distribution in the fourth macro $m_{jj} > 500$ GeV and $\Delta\eta_{jj} > 3.5$ region. The bottom panel of the plots shows the ratio between the number of events in data and the total number of expected events.

yield (black dots) with the post-fit signal (red line). In the high score bins of the DNN output, the signal is clearly visible. In particular, it is more evident, as expected, in the $Z_{\ell\ell} < 1$ category.

The electroweak W^+W^- signal is observed with a significance of 5.6 standard

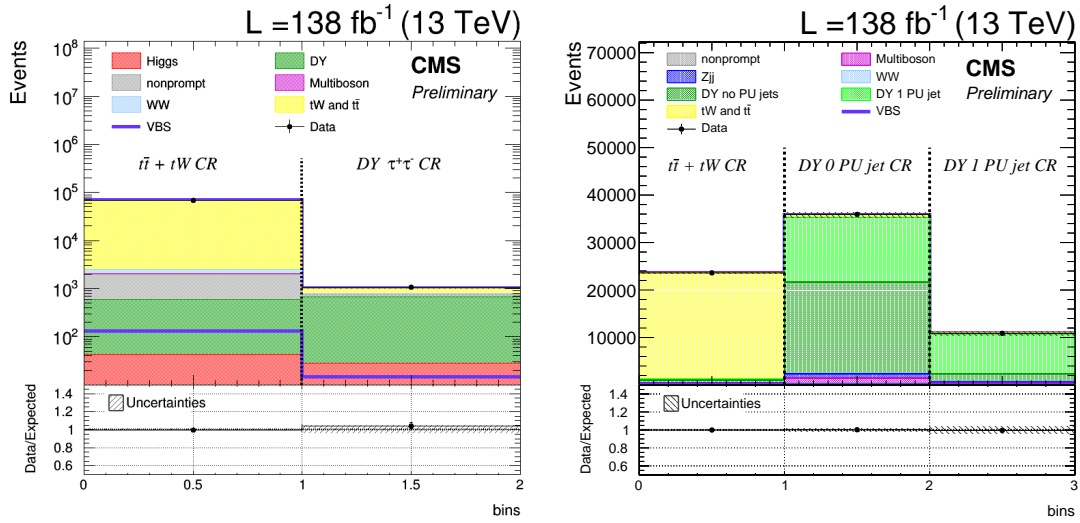


Figure 4.21: Post-fit number of events in the control regions. On the left the $e\mu$ final state: the first bin contains the number of events in the $t\bar{t} + tW$ control region and the second one those in the $DY \tau\tau$ control region. On the right the ee and $\mu\mu$ final state: the first bin shows the number of events in the $t\bar{t} + tW$ control region, the second one those in the $\Delta\eta_{jj} < 5$ DY control region and the third one those in $\Delta\eta_{jj} > 5$ DY control region. The bottom panel of the plots shows the ratio between the number of events in data and the total number of expected events.

deviations, whereas a significance of 5.2 standard deviations was expected with the Asimov data set [86]. The observed signal significance is above the five standard deviation threshold set for discovery; hence, the background-only hypothesis can be discarded with enough confidence.

The cross section's measurement is provided into two different fiducial phase spaces, one more inclusive and one more exclusive with tighter constraints. Indeed, the inclusive fiducial phase space is defined with loose cuts applied on parton-level variables: the two outgoing partons are required to have a $p_T > 10$ GeV and an invariant mass $m_{qq'} > 100$ GeV. In this phase space, the measured cross section is 99 ± 20 fb, whereas the LO prediction is 89 ± 5 fb; the theoretical error on the expected cross section value is evaluated by shifting the QCD factorization scale of the electroweak signal. The exclusive volume is defined by selections on observables at the generator level. These selections mimic the preselections defined in Table 4.3; they are summarized in Table 4.10. At the generator level, so-called dressed leptons and clean jets are used. Indeed, the p_T of all the photons within $\Delta R < 0.1$ around the lepton are summed to the p_T of the lepton itself. Moreover, the jets with at least a dressed lepton inside a cone of $\Delta R = 0.4$ are excluded. The measured cross section in this tighter fiducial phase space is 10.2 ± 2.0 fb to be compared with the LO theoretical prediction of 9.1 ± 0.6 fb. The measured cross sections agree with the predictions of the standard model.

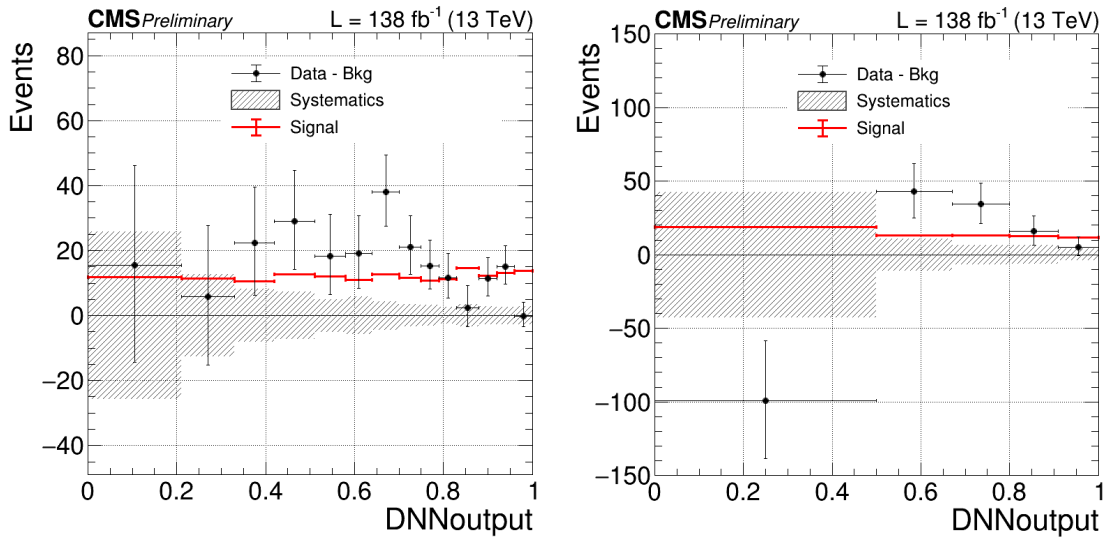


Figure 4.22: The background-subtracted DNN output distribution for the $e\mu$ $Zll < 1$ (on the left) and the $Zll \geq 1$ (on the right) categories. The black dots represent the yield of data minus total post-fit background, while the post-fit signal is drawn as the red line. The dashed band represents the total post-fit uncertainty.

4.10 Summary and outlook

This chapter has reported the first observation at LHC of the electroweak production of W^+W^- bosons in association with two jets.

The measurement has exploited a data set corresponding to an integrated luminosity of 138 fb^{-1} , collected by the CMS detector during 2016–2018 LHC proton-proton collisions at a center-of-mass energy of 13 TeV. The analysis selects events containing two leptons (electrons or muons), two jets, and an amount of missing transverse energy. Interesting events are then categorized according to the flavor of final state leptons into an $e\mu$, an ee , and a $\mu\mu$ category. The very large $t\bar{t}$ background and the irreducible QCD-induced W^+W^- production make the measurement challenging, requiring the use of refined machine learning techniques. Indeed, a deep neural network has been trained to separate the signal in the $e\mu$ categories from the $t\bar{t}$ and QCD-induced backgrounds, boosting the performance of the analysis in the most sensitive final state. Moreover, the ee and $\mu\mu$ categories are included to achieve the final result even if they are strongly contaminated by DY production.

The VBS W^+W^- signal is observed with a statistical significance of 5.6 standard deviations, whereas 5.2 standard deviations were expected.

In addition, cross section’s measurements are performed into two different fiducial volumes, one more inclusive and one more similar to the signal region definition. The fiducial cross section measured in the inclusive phase space is $99 \pm 20 \text{ fb}$, whereas its LO prediction is $89 \pm 5 \text{ fb}$. In the tighter phase space, the EW W^+W^- signal cross section is $10.2 \pm 2.0 \text{ fb}$, to be compared with the LO theoretical prediction of $9.1 \pm 0.6 \text{ fb}$. These results are both found to agree with the standard model prediction;

Table 4.10: Definition of the exclusive fiducial volume. The selections are applied on generator-level observables.

Objects	Requirements
Leptons	$e^+e^-, \mu^+\mu^-, e^+\mu^-, e^-\mu^+$ $p_T^\ell = p_T^{bare\ell} + \sum_i p_T^{\gamma_i}$ if $\Delta R(\ell, \gamma_i) < 0.1$ $p_T^{\ell_1} > 25 \text{ GeV}, p_T^{\ell_2} > 13 \text{ GeV}, p_T^{\ell_3} < 10 \text{ GeV}$ $ \eta < 2.5$ $p_T^{\ell\ell} > 30 \text{ GeV}, m_{\ell\ell} > 50 \text{ GeV}$
Jets	$p_T^j > 30 \text{ GeV}, \eta < 4.7$ $\Delta R(j, \ell) > 0.4$ At least 2 jets, no b jets $m_{jj} > 300 \text{ GeV}, \Delta\eta_{jj} > 2.5$
p_T^{miss}	$p_T^{\text{miss}} > 20 \text{ GeV}$

however, their precision is still strongly limited by the statistical uncertainties.

The LHC is going to start a new data-taking in 2022 (Run III). At the end of this Run III, the integrated luminosity accumulated by the CMS detector will be about 300 fb^{-1} . Our analysis is expected to benefit from the larger data set collected as the contribution from the statistical uncertainty will be reduced. Indeed, in the current status, the majority of VBS studies are limited by the size of the data sample analyzed. Moreover, LHC is preparing for its Phase 2, which is planned to start in 2026 (cf. Figure 2.4 in Sec. 2.1). This phase, known as High Lumi LHC (HL-LHC), will provide proton-proton collisions at $\sqrt{s} = 14 \text{ TeV}$ with an instantaneous luminosity about three times higher than the one delivered by the LHC during Run II. The total integrated luminosity of the events collected during this phase will be of an order of magnitude greater than the one collected at the end of Run III (3000 fb^{-1}). The CMS and the ATLAS detectors are going through major updates to be ready for these new working conditions.

The knowledge of VBS processes has grown in the recent year, bringing from the first discovery (made with the 2016 Run II data sample) to the first precise measurements (achieved with the 2016-2018 data samples). The HL-LHC would provide a sufficiently large data sample to develop VBS analyses even more. Indeed, the study of polarized cross sections and the EFT searches have the HL-LHC as a natural target. At the moment of writing this thesis, prospects and strategies to study EW W^+W^- scattering between polarized bosons are set in place. This study would provide a further check on the standard model consistency. Indeed, the longitudinally polarized scattering is directly related to the Higgs boson and the electroweak symmetry breaking mechanism. Moreover, studies on dimension-6 and dimension-8 EFT operators in the same channel are about to start. A first study

at the LHE level has been published recently [88], combining the W^+W^- channel with other VBS ones, for a set of 15 dimension-6 EFT interesting operators in the Warsaw basis [89]. This preliminary study underlines the ability of the VBS channels to be competitive with diboson productions. A plan to extend these studies at the detector level has been established for the near future.

VBS analyses are a way to constraint SM and BSM physics. The era of discovery is passed; thus, an even more exciting one, the precise measurement era, is about to begin at the LHC.

5 Conclusions

In this thesis, the first observation of the electroweak production of a W^+W^- bosons pair in association with two jets in the fully leptonic final state has been reported. Events used in the analysis refer to the 2016-2018 data sample from proton-proton collisions at center-of-mass energy $\sqrt{s} = 13$ TeV recorded by the CMS detector at the Large Hadron Collider (LHC). The claim for the observation of the W^+W^- electroweak production has been presented with a statistical significance of 5.6 standard deviations, whereas 5.2 standard deviations were expected.

The electroweak W^+W^- production belongs to vector boson scattering processes. These rare processes have cross sections of the order of fb, because at tree level they are mediated completely by electroweak interaction ($O(\alpha_{EW}^6 \alpha_S^0)$). Their investigation is thus fundamental to better understand the electroweak sector of the standard model, as they complement the information deriving from Higgs boson analyses. Moreover, they are tools to search for anomalies in quartic and triple gauge couplings, which may be evidence of new physics. The characteristic signature of VBS processes is the presence of two high-energy jets on the opposite side of the detector at high pseudorapidity values.

The analysis selects events with two jets with the typical VBS signature, two leptons (electrons or muons) with a charge of opposite sign, and missing transverse momentum. The fully leptonic final state was chosen due to its high signal purity. Events are then categorized according to the flavor of the final leptons in three different categories: ee , $\mu\mu$, and $e\mu$. The $ee/\mu\mu$ categories have a worse signal-to-background ratio as they are contaminated from DY production. However, they contribute significantly to the final result; thus, they have been included in the final fit. The other main backgrounds arise from the $t\bar{t}$ -tW processes and the irreducible QCD-induced W^+W^- production. Selections on discriminating observables have been applied to define signal regions with an optimal signal-to-background ratio. Stricter selections have been implemented for $ee/\mu\mu$ categories to reduce the contribution from events from the DY process. A deep neural network (DNN) has been built in the $e\mu$ category to deal with the large $t\bar{t}$ production and the irreducible QCD-induced W^+W^- . The DNN output has been used as a discriminating variable in the final fit. Control regions have been used to normalize the yield of main backgrounds in the data fit. A maximum likelihood fit including all the signal and control regions has been performed to extract the cross section measurements.

Two cross sections have been reported into two different fiducial phase spaces: an inclusive phase space and an exclusive one. The inclusive phase space is defined

with selection on parton level observables; the two outgoing partons are required to have a $p_T > 10$ GeV and an invariant mass $m_{qq'} > 100$ GeV. The measured cross section is 99 ± 20 fb, to be compared with the theoretical expectation at the lowest order of 89 ± 5 fb. In the expected cross section, the errors are due to theoretical uncertainties related to the QCD factorization scale of the signal. The exclusive fiducial volume is defined with requirements on observables at the generator level similar to the ones of the signal region. The cross section observed is 10.2 ± 2.0 fb, whereas the expected one is 9.1 ± 0.6 fb.

The results are in good agreement with standard model expectations; the precision is still limited by the statistical uncertainty, which has the main impact on the cross section's uncertainty. Thus, an improvement is expected to be achieved with the data of Run III (starting in 2022), providing a more accurate measure of inclusive (and differential) cross sections for the electroweak W^+W^- process. Moreover, the HL-LHC era will be the place to develop the full potential of the VBS analysis, thanks to the great amount of data provided. VBS analyses are currently moving from the discovery phase to the era of precision measurements.

The thesis has also presented the work needed to calibrate the electromagnetic calorimeter (ECAL). A new calibration method (EFlow) for the ECAL was developed and tested during this work. Indeed, a good calibration is essential to achieve the best detector performance and thus the optimal precision in an analysis measurement. After laser corrections are applied, additional corrections in time are needed to achieve the desired energy resolution of the ECAL. The EFlow method produces per-crystal intercalibrations with a time granularity of about 1-2 days to correct the time drift in light response related to PN aging. The method relies on the use of low energy minimum bias events, as the ϕ -symmetry, which are expected to have a uniform distribution in ϕ . The EFlow extends the idea of the ϕ -symmetry, normalizing the energy of each crystal to the mean of the barrel. In this way, the response in time of each crystal is adjusted to the average drift of the barrel. Then, events with electrons from W and Z decays are used to correct the residual global drift, providing an overall correction averaged on all the barrel crystals.

The new EFlow method is competitive with the one employed in Run II, which used the E/p distribution of electrons from W and Z decays. Thanks to the fine space-time granularity of these corrections and the short time scale for deriving them, the method may be implemented in Run III to provide the so-called “prompt” calibrations for the ECAL, with a time scale of about one/two day(s).

Bibliography

- [1] Francis Halzen and Alan D. Martin. *Quarks and Leptons: An Introductory Course in Modern Particle Physics*. Ed. by John Wiley & Sons Inc. 1984.
- [2] Daniel Schroeder and Michael Peskin. *An Introduction To Quantum Field Theory*. Ed. by Westview Press. 1995.
- [3] P.A. Zyla et al. “Review of Particle Physics”. In: *PTEP* 2020.8 (2020). DOI: [10.1093/ptep/ptaa104](https://doi.org/10.1093/ptep/ptaa104).
- [4] Sheldon L. Glashow. “Partial-symmetries of weak interactions”. In: *Nuclear Physics* 22.4 (1961). DOI: [10.1016/0029-5582\(61\)90469-2](https://doi.org/10.1016/0029-5582(61)90469-2).
- [5] Steven Weinberg. “A Model of Leptons”. In: *Phys. Rev. Lett.* 19 (21 1967). DOI: [10.1103/PhysRevLett.19.1264](https://doi.org/10.1103/PhysRevLett.19.1264).
- [6] S. L. Glashow, J. Iliopoulos, and L. Maiani. “Weak Interactions with Lepton-Hadron Symmetry”. In: *Phys. Rev. D* 2 (7 1970). DOI: [10.1103/PhysRevD.2.1285](https://doi.org/10.1103/PhysRevD.2.1285).
- [7] F. Englert and R. Brout. “Broken Symmetry and the Mass of Gauge Vector Mesons”. In: *Phys. Rev. Lett.* 13 (9 1964). DOI: [10.1103/PhysRevLett.13.321](https://doi.org/10.1103/PhysRevLett.13.321).
- [8] Peter W. Higgs. “Spontaneous Symmetry Breakdown without Massless Bosons”. In: *Phys. Rev.* 145 (4 1966). DOI: [10.1103/PhysRev.145.1156](https://doi.org/10.1103/PhysRev.145.1156).
- [9] Céline Degrande et al. “Effective field theory: A modern approach to anomalous couplings”. In: *Annals of Physics* 335 (2013). DOI: <https://doi.org/10.1016/j.aop.2013.04.016>.
- [10] CMS Collaboration. “Observation of a new boson at a mass of 125 GeV with the CMS experiment at the LHC”. In: *Physics Letters B* 716.1 (2012). DOI: <https://doi.org/10.1016/j.physletb.2012.08.021>.
- [11] ATLAS Collaboration. “Observation of a new particle in the search for the Standard Model Higgs boson with the ATLAS detector at the LHC”. In: *Physics Letters B* 716.1 (2012). DOI: <https://doi.org/10.1016/j.physletb.2012.08.020>.
- [12] Michael Rauch. *Vector-Boson Fusion and Vector-Boson Scattering*. 2016. arXiv: [1610.08420 \[hep-ph\]](https://arxiv.org/abs/1610.08420).

- [13] ATLAS Collaboration. *Standard Model Summary Plots June 2021*. Tech. rep. Geneva: CERN, July 2021. URL: <http://cds.cern.ch/record/2777014>.
- [14] Alessandro Ballestrero et al. “Precise predictions for same-sign W-boson scattering at the LHC”. In: *Eur. Phys. J. C* 78 (2018). DOI: [10.1140/epjc/s10052-018-6136-y](https://doi.org/10.1140/epjc/s10052-018-6136-y).
- [15] Benjamin W. Lee, C. Quigg, and H. B. Thacker. “Strength of Weak Interactions at Very High Energies and the Higgs Boson Mass”. In: *Phys. Rev. Lett.* 38 (16 1977). DOI: [10.1103/PhysRevLett.38.883](https://doi.org/10.1103/PhysRevLett.38.883).
- [16] Ana Alboteanu, Wolfgang Kilian, and Jürgen Reuter. “Resonances and unitarity in weak boson scattering at the LHC”. In: *Journal of High Energy Physics* 2008.11 (2008). DOI: [10.1088/1126-6708/2008/11/010](https://doi.org/10.1088/1126-6708/2008/11/010).
- [17] CMS Collaboration. “Observation of electroweak production of same-sign W boson pairs in the two jet and two same-sign lepton final state in proton-proton collisions at $\sqrt{s} = 13$ TeV”. In: *Phys. Rev. Lett.* 120.8 (2018). DOI: [10.1103/PhysRevLett.120.081801](https://doi.org/10.1103/PhysRevLett.120.081801). arXiv: [1709.05822 \[hep-ex\]](https://arxiv.org/abs/1709.05822).
- [18] CMS Collaboration. “Measurements of production cross sections of WZ and same-sign WW boson pairs in association with two jets in proton-proton collisions at $\sqrt{s} = 13$ TeV”. In: *Phys. Lett. B* 809 (2020). DOI: [10.1016/j.physletb.2020.135710](https://doi.org/10.1016/j.physletb.2020.135710). arXiv: [2005.01173 \[hep-ex\]](https://arxiv.org/abs/2005.01173).
- [19] CMS Collaboration. “Measurements of production cross sections of polarized same-sign W boson pairs in association with two jets in proton-proton collisions at $\sqrt{s} = 13$ TeV”. In: *Phys. Lett. B* 812 (2020). DOI: [10.1016/j.physletb.2020.136018](https://doi.org/10.1016/j.physletb.2020.136018). arXiv: [2009.09429](https://arxiv.org/abs/2009.09429).
- [20] CMS Collaboration. “Evidence for electroweak production of four charged leptons and two jets in proton-proton collisions at $\sqrt{s} = 13$ TeV”. In: *Phys. Lett. B* 812 (2021). DOI: [10.1016/j.physletb.2020.135992](https://doi.org/10.1016/j.physletb.2020.135992). arXiv: [2008.07013 \[hep-ex\]](https://arxiv.org/abs/2008.07013).
- [21] CMS Collaboration. “Measurement of the electroweak production of $Z\gamma$ and two jets in proton-proton collisions at $\sqrt{s} = 13$ TeV and constraints on anomalous quartic gauge couplings”. In: *Phys. Rev. D* 104 (2021). DOI: [10.1103/PhysRevD.104.072001](https://doi.org/10.1103/PhysRevD.104.072001). arXiv: [2106.11082](https://arxiv.org/abs/2106.11082).
- [22] CMS Collaboration. *Search for vector boson scattering at the LHC Run 2 with CMS data in the semi-leptonic $l\nu qq$ final state*. Tech. rep. Geneva: CERN, 2021. URL: <https://cds.cern.ch/record/2776799>.
- [23] Thomas Sven Pettersson and P Lefèvre. *The Large Hadron Collider: conceptual design*. Tech. rep. 1995. URL: <https://cds.cern.ch/record/291782>.
- [24] Esma Mobs. “The CERN accelerator complex. Complexe des accélérateurs du CERN”. In: (2016). General Photo. URL: <https://cds.cern.ch/record/2197559>.
- [25] CMS collaboration. *Public CMS Luminosity Information*. <https://twiki.cern.ch/twiki/bin/view/CMSPublic/LumiPublicResults>.

- [26] I. Bejar Alonso et al. *High-Luminosity Large Hadron Collider (HL-LHC): Technical design report*. Tech. rep. 2020. DOI: 10.23731/CYRM-2020-0010.
- [27] CMS Collaboration. “The CMS experiment at the CERN LHC”. In: *Journal of Instrumentation* 3 (2008). DOI: 10.1088/1748-0221/3/08/s08004.
- [28] CMS collaboration. *CMS detector design*. <https://cms.cern/news/cms-detector-design>.
- [29] A Dominguez et al. *CMS Technical Design Report for the Pixel Detector Upgrade*. Tech. rep. 2012. URL: <https://cds.cern.ch/record/1481838>.
- [30] Q. Ingram et al. “Energy resolution of the barrel of the CMS Electromagnetic Calorimeter”. In: 2.04 (2007). DOI: 10.1088/1748-0221/2/04/p04004.
- [31] J Mans et al. *CMS Technical Design Report for the Phase 1 Upgrade of the Hadron Calorimeter*. Tech. rep. 2012. URL: <https://cds.cern.ch/record/1481837>.
- [32] CMS Collaboration. *CMS Physics: Technical Design Report Volume 1: Detector Performance and Software*. Technical design report. CMS. Geneva: CERN, 2006. URL: <http://cds.cern.ch/record/922757>.
- [33] CMS collaboration. “Performance of CMS muon reconstruction in pp collision events at $\sqrt{s} = 7$ TeV”. In: 7.10 (2012). DOI: 10.1088/1748-0221/7/10/p10002.
- [34] CMS Collaboration. “The CMS trigger system”. In: *JINST* 12 (2017). DOI: 10.1088/1748-0221/12/01/P01020. arXiv: 1609.02366 [physics.ins-det].
- [35] CMS Collaboration. “Performance of the CMS Level-1 trigger in proton-proton collisions at $\sqrt{s} = 13$ TeV”. In: *JINST* 15 (2020). DOI: 10.1088/1748-0221/15/10/P10017. arXiv: 2006.10165 [hep-ex].
- [36] CMS Collaboration. “Particle-flow reconstruction and global event description with the CMS detector”. In: *Journal of Instrumentation* 12.10 (2017). ISSN: 1748-0221. DOI: 10.1088/1748-0221/12/10/p10003.
- [37] CMS Collaboration. “Performance of the CMS muon detector and muon reconstruction with proton-proton collisions at $\sqrt{s} = 13$ TeV”. In: *JINST* 13 (2018). DOI: 10.1088/1748-0221/13/06/P06015. arXiv: 1804.04528 [physics.ins-det].
- [38] Wolfgang Adam et al. *Track Reconstruction in the CMS tracker*. Tech. rep. Geneva: CERN, 2006. URL: <https://cds.cern.ch/record/934067>.
- [39] CMS Collaboration. “Performance of electron reconstruction and selection with the CMS Detector in proton-proton collisions at $\sqrt{s} = 8$ TeV”. In: *JINST* 10 (2015). DOI: 10.1088/1748-0221/10/06/P06005. arXiv: 1502.02701 [physics.ins-det].
- [40] K. Ito and K. Xiong. “Gaussian filters for nonlinear filtering problems”. In: *IEEE Transactions on Automatic Control* 45.5 (2000). DOI: 10.1109/9.855552.

- [41] Matteo Cacciari, Gavin P. Salam, and Gregory Soyez. “The anti-kt jet clustering algorithm”. In: *JHEP* 04 (2008), p. 063. DOI: 10.1088/1126-6708/2008/04/063. arXiv: 0802.1189 [hep-ex].
- [42] Matteo Cacciari, Gavin P. Salam, and Gregory Soyez. “FastJet user manual”. In: *Eur. Phys. J. C* 72 (2012). DOI: 10.1140/epjc/s10052-012-1896-2. arXiv: 1111.6097 [hep-ph].
- [43] CMS Collaboration. “Jet energy scale and resolution in the CMS experiment in pp collisions at 8 TeV”. In: *Journal of Instrumentation* 12.02 (2017). DOI: 10.1088/1748-0221/12/02/p02014.
- [44] CMS Collaboration. “Performance of missing transverse momentum reconstruction in proton-proton collisions at $\sqrt{s} = 13$ TeV using the CMS detector”. In: *JINST* 14 (2019). DOI: 10.1088/1748-0221/14/07/P07004. arXiv: 1903.06078 [hep-ex].
- [45] CMS Collaboration. “Reconstruction of signal amplitudes in the CMS electromagnetic calorimeter in the presence of overlapping proton-proton interactions”. In: *JINST* 15 (2020). DOI: 10.1088/1748-0221/15/10/P10002. arXiv: 2006.14359.
- [46] T. Adams et al. “Beam test evaluation of electromagnetic calorimeter modules made from proton-damaged PbWO₄ crystals”. In: *Journal of Instrumentation* 11.04 (2016). DOI: 10.1088/1748-0221/11/04/p04012.
- [47] M. Anfreville et al. “Laser monitoring system for the CMS lead tungstate crystal calorimeter”. In: *Nucl. Instrum. Meth. A* 594 (2008). DOI: 10.1016/j.nima.2008.01.104.
- [48] CMS Collaboration. *CMS ECAL Response to Laser Light*. Mar. 2019. URL: <https://cds.cern.ch/record/2668200>.
- [49] CMS Collaboration. *CMS ECAL Laser Monitoring System*. Sept. 2019. URL: <https://cds.cern.ch/record/2690932>.
- [50] CMS Collaboration. “Precision luminosity measurement in proton-proton collisions at $\sqrt{s} = 13$ TeV in 2015 and 2016 at CMS”. In: *Eur. Phys. J. C* 81 (2021). DOI: 10.1140/epjc/s10052-021-09538-2. arXiv: 2104.01927 [hep-ex].
- [51] CMS Collaboration. *CMS luminosity measurement for the 2017 data-taking period at $\sqrt{s} = 13$ TeV*. CMS Physics Analysis Summary CMS-PAS-LUM-17-004. 2017. URL: <https://cds.cern.ch/record/2621960>.
- [52] CMS Collaboration. *CMS luminosity measurement for the 2018 data-taking period at $\sqrt{s} = 13$ TeV*. Tech. rep. Geneva: CERN, 2019. URL: <https://cds.cern.ch/record/2676164>.
- [53] Simone Alioli et al. “A general framework for implementing NLO calculations in shower Monte Carlo programs: the POWHEG BOX”. In: *JHEP* 06 (2010). DOI: 10.1007/JHEP06(2010)043. arXiv: 1002.2581 [hep-ph].

- [54] J. Alwall et al. “The automated computation of tree-level and next-to-leading order differential cross sections, and their matching to parton shower simulations”. In: *JHEP* 07 (2014). doi: 10.1007/JHEP07(2014)079. arXiv: 1405.0301 [hep-ph].
- [55] John M. Campbell and R. Keith Ellis. “An update on vector boson pair production at hadron colliders”. In: *Phys. Rev. D* 60 (1999). doi: 10.1103/PhysRevD.60.113006. arXiv: hep-ph/9905386.
- [56] John M. Campbell, R. Keith Ellis, and Ciaran Williams. “Vector boson pair production at the LHC”. In: *Journal of High Energy Physics* 2011.7 (2011). ISSN: 1029-8479. doi: 10.1007/jhep07(2011)018.
- [57] John M. Campbell, R. Keith Ellis, and Walter T. Giele. “A multi-threaded version of MCFM”. In: *Eur. Phys. J. C* 75 (2015), p. 246. doi: 10.1140/epjc/s10052-015-3461-2. arXiv: 1503.06182 [physics.comp-ph].
- [58] Vardan Khachatryan et al. “Event generator tunes obtained from underlying event and multiparton scattering measurements”. In: *Eur. Phys. J. C* 76 (2016). doi: 10.1140/epjc/s10052-016-3988-x. arXiv: 1512.00815 [hep-ex].
- [59] CMS Collaboration. “Extraction and validation of a new set of CMS PYTHIA8 tunes from underlying-event measurements”. In: *Eur. Phys. J. C* 80 (2020), p. 4. doi: 10.1140/epjc/s10052-019-7499-4. arXiv: 1903.12179 [hep-ex].
- [60] NNPDF Collaboration. “Parton distributions with QED corrections”. In: *Nucl. Phys. B* 877 (2013). doi: 10.1016/j.nuclphysb.2013.10.010. arXiv: 1308.0598 [hep-ph].
- [61] NNPDF Collaboration. “Unbiased global determination of parton distributions and their uncertainties at NNLO and at LO”. In: *Nucl. Phys. B* 855 (2012). doi: 10.1016/j.nuclphysb.2011.09.024. arXiv: 1107.2652 [hep-ph].
- [62] NNPDF Collaboration. “Parton distributions from high-precision collider data”. In: *Eur. Phys. J. C* 77 (2017). doi: 10.1140/epjc/s10052-017-5199-5. arXiv: 1706.00428 [hep-ph].
- [63] S. Agostinelli et al. “GEANT4: a simulation toolkit”. In: *Nucl. Instrum. Meth. A* 506 (2003). doi: 10.1016/S0168-9002(03)01368-8.
- [64] CMS Collaboration. “Measurements of properties of the Higgs boson decaying to a W boson pair in pp collisions at $\sqrt{s} = 13$ TeV”. In: *Phys. Lett. B* 791 (2019). doi: 10.1016/j.physletb.2018.12.073. arXiv: 1806.05246 [hep-ex].
- [65] Torbjörn Sjöstrand et al. “An Introduction to PYTHIA 8.2”. In: *Comput. Phys. Commun.* 191 (2015). doi: 10.1016/j.cpc.2015.01.024. arXiv: 1410.3012 [hep-ph].

- [66] Keith Hamilton, Paolo Nason, and Giulia Zanderighi. “Finite quark-mass effects in the NNLOPS POWHEG+MiNLO Higgs generator”. In: *JHEP* 05 (2015). doi: 10.1007/JHEP05(2015)140. arXiv: 1501.04637 [hep-ph].
- [67] Emanuele Re, Marius Wiesemann, and Giulia Zanderighi. “NNLOPS accurate predictions for W^+W^- production”. In: *Journal of High Energy Physics* 2018.12 (2018). issn: 1029-8479. doi: 10.1007/jhep12(2018)121.
- [68] Barbara Jäger et al. “Parton-shower effects in Higgs production via vector-boson fusion”. In: *The European Physical Journal C* 80.8 (2020). issn: 1434-6052. doi: 10.1140/epjc/s10052-020-8326-7.
- [69] D. Rainwater, R. Szalapski, and D. Zeppenfeld. “Probing color-singlet exchange in Z+2-jet events at the CERN LHC”. In: *Physical Review D* 54.11 (1996). doi: 10.1103/physrevd.54.6680. arXiv: 9605444 [hep-ph].
- [70] CMS Collaboration. “Measurement of the Higgs boson production rate in association with top quarks in final states with electrons, muons, and hadronically decaying tau leptons at $\sqrt{s} = 13$ TeV”. In: *Eur. Phys. J. C* 81 (2021). doi: 10.1140/epjc/s10052-021-09014-x. arXiv: 2011.03652v2.
- [71] CMS Collaboration. “Jet algorithms performance in 13 TeV data”. In: (2017).
- [72] E. Bols et al. “Jet flavour classification using DeepJet”. In: *Journal of Instrumentation* 15.12 (2020). issn: 1748-0221. doi: 10.1088/1748-0221/15/12/p12012.
- [73] CMS Collaboration. *Performance of the DeepJet b tagging algorithm using 41.9/fb of data from proton-proton collisions at 13 TeV with Phase 1 CMS detector*. CMS Detector Performance Note CMS-DP-2018-058. 2018. url: <http://cds.cern.ch/record/2646773>.
- [74] Daniele Bertolini et al. “Pileup per particle identification”. In: *JHEP* 10 (2014). doi: 10.1007/JHEP10(2014)059. arXiv: 1407.6013 [hep-ph].
- [75] Sergey Ioffe and Christian Szegedy. “Batch Normalization: Accelerating Deep Network Training by Reducing Internal Covariate Shift”. In: *CoRR* abs/1502.03167 (2015). arXiv: 1502.03167.
- [76] Lutz Prechelt. “Early Stopping — But When?” In: *Neural Networks: Tricks of the Trade: Second Edition*. Ed. by Grégoire Montavon, Geneviève B. Orr, and Klaus-Robert Müller. Berlin, Heidelberg: Springer Berlin Heidelberg, 2012. doi: 10.1007/978-3-642-35289-8_5.
- [77] Diederik P. Kingma and Jimmy Ba. “Adam: A Method for Stochastic Optimization”. In: (2017). arXiv: 1412.6980 [cs.LG].
- [78] Tom Fawcett. “An introduction to ROC analysis”. In: *Pattern Recognition Letters* 27.8 (2006). ROC Analysis in Pattern Recognition. doi: <https://doi.org/10.1016/j.patrec.2005.10.010>.
- [79] CMS Collaboration. “An embedding technique to determine $\tau\tau$ backgrounds in proton-proton collision data”. In: *Journal of Instrumentation* 14.06 (2019). doi: 10.1088/1748-0221/14/06/p06032.

- [80] Vardan Khachatryan et al. “Performance of electron reconstruction and selection with the CMS detector in proton-proton collisions at $\sqrt{s} = 8$ ”. In: *JINST* 10 (2015), P06005. DOI: 10.1088/1748-0221/10/06/P06005. arXiv: 1502.02701 [physics.ins-det].
- [81] A. M. Sirunyan et al. “Performance of the CMS muon detector and muon reconstruction with proton-proton collisions at $\sqrt{s} = 13$ TeV”. In: *JINST* 13 (2018), P06015. DOI: 10.1088/1748-0221/13/06/P06015. arXiv: 1804.04528 [physics.ins-det].
- [82] Vardan Khachatryan et al. “Jet energy scale and resolution in the CMS experiment in pp collisions at 8 TeV”. In: *JINST* 12 (2017), P02014. DOI: 10.1088/1748-0221/12/02/P02014. arXiv: 1607.03663 [hep-ex].
- [83] Albert M Sirunyan et al. “Performance of missing transverse momentum reconstruction in proton-proton collisions at $\sqrt{s} = 13$ TeV using the CMS detector”. In: *JINST* 14 (2019), P07004. DOI: 10.1088/1748-0221/14/07/P07004. arXiv: 1903.06078 [hep-ex].
- [84] Stefano Catani et al. “Soft gluon resummation for Higgs boson production at hadron colliders”. In: *JHEP* 07 (2003), p. 028. DOI: 10.1088/1126-6708/2003/07/028. arXiv: hep-ph/0306211.
- [85] M. Cacciari et al. “The $t\bar{t}$ cross-section at 1.8 and 1.96: a study of the systematics due to parton densities and scale dependence”. In: *JHEP* 04 (2004), p. 068. DOI: 10.1088/1126-6708/2004/04/068. arXiv: hep-ph/0303085.
- [86] Glen Cowan et al. “Asymptotic formulae for likelihood-based tests of new physics”. In: *The European Physical Journal C* 71.2 (2011). DOI: 10.1140/epjc/s10052-011-1554-0.
- [87] Luv Demortier. “P Values and Nuisance Parameters”. In: *PHYSTAT-LHC Workshop on Statistical Issues for LHC Physics: CERN, Geneva, Switzerland 27 - 29 Jun 2007. PHYSTAT-LHC Workshop on Statistical Issues for LHC Physics* (2008). DOI: 10.5170/CERN-2008-001.23. URL: <http://cds.cern.ch/record/1099967>.
- [88] Riccardo Bellan et al. “A sensitivity study of VBS and diboson WW to dimension-6 EFT operators at the LHC”. In: (Aug. 2021). arXiv: 2108.03199 [hep-ph].
- [89] B. Grzadkowski et al. “Dimension-six terms in the Standard Model Lagrangian”. In: *Journal of High Energy Physics* 2010.10 (2010). DOI: 10.1007/jhep10(2010)085.